Title
ELECTRONIC STRUCTURE OP DIAMOND, ZINCBLENDE AND CHALCOPYRITE SEMICONDUCTORS

Permalink
https://escholarship.org/uc/item/8r042690

Author
Alvarez, Carmen Varea de

Publication Date
1973-09-01

LBL-1863

ELECTRONIC STRUCTURE OF DIAMOND, ZINCBLENDE AND CHALCOPYRITE SEMICONDUCTORS

Carmen Varea de Alvarez

(Ph. D. Thesis)

September 1973

Prepared for the U. S. Atomic Energy Commission
under Contract W-7405-ENG-48

LAWRENCE BERKELEY LABORATORY • UNIVERSITY OF CALIFORNIA • BERKELEY

ELECTRONIC STRUCTURE OF DIAMOND, ZINCBLENDE AND CHALCOPYRITE SEMICONDUCTORS

Contents

ELECTRONIC STRUCTURE OF DIAMOND, ZINCBLENDE AND CHALCOPYRITE SEMICONDUCTORS

Carmen Varea De Alvarez

Inorganic Materials Research Division, Lawrence Berkeley Laboratory
and Department of Physics; University of California
Berkeley, California 94720

ABSTRACT

The dependence of energy band structure and electronic charge density on pseudopotential parameters is investigated for diamond type semiconductors.

The Empirical Pseudopotential Method (EPM)[3] is applied to InSb, InAs, InP and GaP. Spin-orbit interactions are included in the first two crystals. The imaginary part of the frequency dependent dielectric function, $\varepsilon_2(\omega)$ is calculated and the reflectivity spectrum $R(\omega)$ and modulated reflectivity $R'(\omega)/R(\omega)$ is calculated and compared directly with experiment. The agreement for $R(\omega)$ and $R'(\omega)/R(\omega)$ between experiment and theory is better than 0.2 eV, for all four crystals, on the average. In addition electron charge densities for InAs and InSb are calculated.

The pressure coefficients of the most important gaps for Si and InP are calculated and correlated to the properties of the electronic Bloch states.

The chalcopyrite crystal structure and the relation between the zincblende Brillouin Zone and the chalcopyrite Brillouin Zone are discussed in detail. The energy band structure of $ZnGeP_2$ and $ZnGeAs_2$ is calculated along symmetry directions assuming "transferability of the pseudopotentials" and compared with those of their "analogs"

(GaP and GaAs respectively). A full zone calculation of the energy bands of $ZnGeP_2$ is presented along with the density of states curve $D(\omega)$, the $\varepsilon_2(\omega)$ and $R(\omega)$. A complete critical point analysis enables us to identify the prominent structure in the $D(\omega)$, $\varepsilon_2(\omega)$ and $R(\omega)$.

I. INTRODUCTION

Since the concept of the pseudopotential was first introduced, the application of the pseudopotential method to calculate physical quantities that depend only on the valence electrons of a crystal, has been highly successful. In a pseudopotential calculation, the crystalline potential is assumed to be the combination of spherically symmetric pseudopotentials located at the ion sites. Since these pseudopotentials are constructed to describe only the valence electrons including orthogonalization to the core states in the crystal, the pseudopotential is much weaker than the actual potential.

Pseudopotentials for the elements can be constructed theoretically, as those of Heine and Animalu[5], and they can also be obtained by fitting to all the relevant experimental information of a given crystal. This latter procedure has been called the Empirical Pseudopotential Method (EPM). Another, but related way of proceeding is to use of the concept of transferability of the pseudopotentials; that is, by assuming that the atomic pseudopotentials are independent of crystal structure and composition, one can predict the energy band structure or any property of the valence electrons of a given crystal provided one knows the atomic pseudopotentials of its constituents either by using theoretically determined pseudopotentials or by extracting them from an EPM calculation on other crystal.

In Chapter II of this work, we briefly review the pseudopotential method and the properties of the pseudopotentials for the elements in the IV-column of the periodic table, we also study the relationship between the pseudopotential form factors, the energy band structure and the electronic charge density in the valence bands of diamond type semiconductors via a two parameter model pseudopotential.

In Chapter III, we apply the EPM to obtain the form factors, energy band structure, $\varepsilon_2(\omega)$, $R(\omega)$ and $R'(\omega)/R(\omega)$ of the zincblende semiconductors InSb, InAs, InP and GaP; our results are compared with experiment. This comparison, and an analysis of the Van Hove[14] singularities of our calculated $\varepsilon_2(\omega)$ allows us to perform a positive identification of the electronic transitions responsible for the main structure of the experimental reflectivity spectra.

In Chapter IV, the pressure coefficients of the main gaps in Si and InP are calculated, the object of this calculation is three fold: 1) we want to understand why these crystals transform as they do under high hydrostatic stress, 2) we investigate the "Empirical Rule",[28] and the correlation between a wave function $\psi_{\underline{k}}^{n}$ and the pressure coefficient of the energy level $E_{\underline{k}}^{n}$ for a given wave vector $\underline{k}$ and a given band n, and 3) by fitting our form factors to the experimental pressure coefficient, we gain information on the "scaling" of the form factors.

In Chapter V, we discuss the optical and electronic properties of the chalcopyrite compounds of the form $A^2B^4C_2^5$. The energy band structure, $D(\omega)$, $\varepsilon_2(\omega)$ and $R(\omega)$ are calculated for $ZnGeP_2$ using the form factors of its analog GaP and those of Ge; critical point analysis on $\varepsilon_2(\omega)$ is performed and comparison of our calculated $R(\omega)$ with experiment yields information on the energy gap region of the energy band structure.

Energy band structures for $ZnGeP_2$ and $ZnGeAs_2$ are calculated along symmetry lines, using transferability of the pseudopotentials. The results compared with those of their analogs GaP and GaAs. Using the identifications of the main structure of our calculated $R(\omega)$, the results for $ZnGeP_2$ and $ZnGeAs_2$ compare well with experiment; of course, only a full zone calculation can ascertain this.

II. DIAMOND STRUCTURE SEMICONDUCTORS

A. Pseudopotential Method

For the Empirical Pseudopotential Method (EPM), the crystal is considered as a collection of N spherically symmetric "ions" located at the lattice sites. The ZN valence electrons do not interact with each other except in a Hartree sense, and they interact with the ions through a weak local pseudopotential v(r). This pseudopotential includes the Coulomb attraction with the ions, $-Ze^2/r$ and a repulsive term near the core arising from the requirement that the valence-electron wavefunctions be orthogonal to the core wavefunctions (the highly localized core states are not solutions of the pseudopotential Schrödinger's equation, so the pseudopotential is much weaker near the core region than the actual potential). The final contribution to the pseudopotential comes from the interaction arising from the valence electrons which can be included by using a screening function.

Once the pseudopotential is fixed, the energy bands and electronic charge density can be obtained by solving for the eigenvalues and eigenvectors of the one electron Schrödinger equation

$$\left[\frac{p^2}{2m} + V(\vec{r})\right] \phi_{n,\vec{k}}(\vec{r}) = E_n(\vec{k})\ \phi_{n,\vec{k}}(\vec{r}) \qquad (1)$$

where $\vec{k}$ is the wavevector, n the band index and the pseudopotential is given by

$$V(r) = \sum_{\alpha}\sum_{\text{cells}} v_{\alpha}(\vec{r} - \vec{r}_{\alpha j}). \qquad (2)$$

In Eq. (2), α denotes the different kinds of atoms in the unit cell. Crystal symmetry is easily taken into account when this pseudopotential is expanded in the reciprocal lattice. In the diamond structure, with two atoms per cell at positions $\pm \vec{\tau}$ where $\vec{\tau} = \frac{a}{8}(1,1,1)$, a is the lattice constant, Eq. (2) becomes

$$V(\vec{r}) = \sum_{G} v(\vec{G}) \cos(\vec{G}\cdot\vec{\tau})\, e^{i\vec{G}\cdot\vec{r}} \qquad (3)$$

with

$$v(\vec{G}) = \left(\frac{2}{\Omega}\right) \int v(r) e^{i\vec{G}\cdot\vec{r}}\, d^3r \qquad (4)$$

where Ω is the volume of the primitive cell and G is in units of $2\pi/a$. Usually, in EPM calculations only the form factors $v(\sqrt{3})$, $v(\sqrt{4})$, $v(\sqrt{8})$ and $v(\sqrt{11})$ are allowed to be nonzero but the structure factor $\cos \vec{G}.\vec{\tau} = 0$ for $|\vec{G}| = 2$ in diamond structure materials; therefore, this method uses three adjustable parameters to fit the known energy band features.

The pseudopotential curves v(q) can usually be divided into two regions separated by a point where $V(q_0) = 0$. q_0 is related to the radius of the atomic core r_0. For $q < q_0$, $v(q) < 0$ and this region represents the screened attractive coulomb potential outside the ion cores; for the region $q > q_0$, v(q) is positive and approximately represents the repulsive part of the potential arising from the orthogonalization conditions inside an effective core radius. With this in mind, one would expect to obtain all the main properties of the band structure and electronic charge density from only two form factors each representing one of the two regions. We have calculated the band structure and electronic charge densities as function of position in the unit cell for several values of these two form factors. This was done in an attempt to understand the relationship between charge density and band structure in crystalline diamond structure semiconductors. We have found that by changing only one parameter in the pseudopotential, we can simulate the properties of the column IV semiconductors.

For other crystal structures (e.g. zincblende), the pseudopotential method can be used by taking into account the correct structure factors. The details will be given in the appropriate sections.

B. Diamond Structure Semiconductors and Model Pseudopotential Calculations

The group IV elements, carbon, silicon, germanium, gray tin and lead form a very interesting series. The four atomic valence electrons for these elements are in the s^2p^2 electronic configuration. For the crystalline state, in the cases of Si, Ge and Sn (but not Pb), the formation of sp^3 hybrid orbitals gives the strongest bonding overlap and this is the most stable configuration. The sp^3 orbitals give rise to four equivalent tetrahedrally coordinated bonds, and this bonding results in the diamond structure for these crystals. In this group, the bond energy is a decreasing function of the atomic number; carbon has very strong bond while gray tin is only stable at low temperatures and undergoes a phase transformation at 292°K to metallic white tin. Lead crystallizes in the fcc structure and is metallic.

Phillips[1] has been able to correlate the bonding properties with the average gap between valence and conduction bands in semiconductors and insulators; the bonding strength being proportional to the size of the gap. Another approach which showed similar trends was taken by Walter and Cohen[2] who used the Empirical Pseudopotential Method (EPM).[3]

Two important features come in when doing an EPM calculation: (1) the nearest neighbor distance, which increases in going from C to Pb, and (2) the pseudopotential, which depends on the element of interest. These features raise an interesting question: is it the change in nearest neighbor distance, d, that is responsible for the marked differences between these materials, or is it the different effective potential that the electrons feel outside the core which produces such differences? A partial answer comes from pressure experiments. The application of hydrostatic pressure is expected primarily to change d. What one observes in this case is an increase in the average direct gap and a trend toward metallization. Because these are contradictory, then based on pressure data only, changes in d from element to element cannot explain the observed trends in the group IV materials.

To investigate the dependence of the properties on the potentials used, we have calculated the band structures and electronic charge densities in the diamond structure for three model pseudopotentials using only two parameters to specify the pseudopotentials. One of these parameters was kept constant while the other was chosen to give the band structure of a one eV gap semiconductor like Ge; a zero gap semiconductor such as Sn; and a band structure with overlapping bands having metallic properties. We have also calculated the band structure and charge density in the Fermi-Thomas approximation for a pseudopotential appropriate to Ge. All through this work the lattice constant used was that of Ge.

The EPM uses three adjustable pseudopotential form factors to fit the known energy band features of diamond type materials. Since in general, the wave vector q_o which separates the attractive and repulsive parts of the pseudopotential curves is such that $q_o \leq \sqrt{8}\,\frac{2\pi}{a}$, the parameters we choose are $v(\sqrt{3}) < 0$ and $v(\sqrt{8}) \geq 0$. In Fig. 1 we show the three form factors obtained by Cohen and Bergstresser[4] for Ge together with the theoretical pseudopotential of Heine and Animalu[5] and the parameters used in this work; their actual values are in Ry given below:

For model potential I:

$$v(\sqrt{3}) = -0.25,\ v(\sqrt{8}) = 0.071;$$

for model potential II:

$$v(\sqrt{3}) = -0.25,\ v(\sqrt{8}) = 0.053;$$

for model potential III:

$$v(\sqrt{3}) = -0.25,\ v(\sqrt{8}) = 0.0.$$

We have also investigated a Fermi-Thomas model with a cutoff of the potential at $q = 4\frac{2\pi}{a}$. The resulting form factors are (Ry)

$$v(\sqrt{3}) = -0.3004,\ v(\sqrt{8}) = -0.1688,\ v(\sqrt{11}) = -0.1338.$$

For a given set of form factors, the Hamiltonian can be solved for the energy eigenvalues and wavefunctions $\psi_{n,k}(r)$ at many k points in the Brillouin zone. The charge density for each valence band is then given by

$$\rho_n(r) = \sum_k e|\psi_{n,k}(r)|^2 . \qquad (5)$$

In the diamond structure there are a total of eight valence electrons per primitive cell and two valence electrons per energy band. The charge density results given in the next section are plotted in the form of contour plots in the (1,-1,0) plane, which contains an atom and two of its nearest neighbors. The density is plotted in units of (e/Ω) where Ω is the volume of the primitive cell.

Model potential I. In Figs. 2 and 3 we show the calculated energy band structure and electronic charge density, in the valence band, for model potential I.

Table I shows a comparison between the main energy splittings obtained by Cohen and Bergstresser[4] (CB) using three form factors, the present model using two form factors, and the experimental values for Ge. The main difference between our results and those of CB occurs in the first indirect gap. There are smaller differences in the higher conduction bands and even smaller differences in the valence bands. This model would predict optical properties close to those obtained by a CB potential.

From the total charge density for the four valence bands (Fig. 3) the covalent bonding is apparent. The concentration of charge in the bond is a little weaker than that calculated by Walter and Cohen[2] using a CB potential. This is not inconsistent with our model since the valence to conduction band average energy gap for this model is smaller than the one calculated by CB. Thus a simple model pseudopotential that uses only two parameters, one representing the screened Coulomb attraction to the atoms (V_3), and another that represents the repulsive orthogonalization requirements (V_8), describes quite well the energy band structure and bonding properties of Ge.

Model potential II. As the pseudopotential form factor V_8 is reduced, the repulsive part of the atomic potential decreases and the s-like levels which are more sensitive to the potential near the atoms become more tightly bound. For a value of 0.053 Ry for V_8 the energy of the $\Gamma_{25'}$ and $\Gamma_{2'}$ levels becomes equal giving a band structure similar to that of gray tin.

In Fig. 4 the calculated energy band structure is given and in Fig. 5 the total charge density for the four valence bands for our second model potential is shown. The energy band structure is actually that of a semimetal with a small overlap of 0.07 eV from $\Gamma_{25'}$ to L_1; the first direct gap is zero as in the case of α-tin. Table 1 shows the main energy splittings obtained in model II--all the 4-5 splittings are smaller than those of model I. In the next paragraph we show how the changes of the energy splittings with V_8 are easily understood from the form of the wave functions at the bottom of the conduction band.

In part IV of this work, we calculate the charge density for the $\Gamma_{2'}$, L_1 and X_1 states in the conduction band of Si. Our results are as follows:

(1) The charge density for states near Γ_2' is highly peaked near the atoms and it is very sensitive to changes of the pseudopotential in that region in real space. It is therefore very sensitive to changes

in V_8.

(2) The charge density for states near L_1 is more "free like" but peaked between the atoms and the antibonding site so they are less sensitive to changes in V_8 than Γ_2'.

(3) The charge density for states near X_1 is almost constant so that the energy splitting $\Gamma_{25'} - X_1$ is very little affected by changes in V_8.

Figures 6 and 7 show the charge density contour plots in the first valence band for model potential I and II respectively; the reduction of V_8 from the first to the second model has caused a decrease in the repulsive part of the potential near the atoms, and the electronic charge tends to pile up closer to the atomic sites; the same effect is observed in band 2. Bands 3 and 4 are almost identical for models I and II; p-like bands are quite insensitive to the potential near the atoms. The only trend we observe in comparing Figs. 5 and 3 is a small trend to pile up charge closer to the atoms in model II; this tendency is also present in the charge densities of Walter and Cohen[2] going from Si to Ge to α-tin. This is mainly caused by the charge density of the first two s-like valence bands as already discussed.

Model potential III. Figures 8 and 9 show the energy band structure and total charge density in the valence band for model potential III. V_8 is zero in this model; the energy band structure is that of a semimetal and Table I includes the values of the main energy splittings.

Since V_8 is now zero, the piling of the charge density closer to the atoms is more accentuated as shown in Fig. 9. The charge density for valence bands 1 and 2 is completely s-like with no overlap at all, while valence band 3 is affected slightly since it includes antibonding states near L_1 which is now in the valence band. The inclusion of these states affects the bonding charge for this band by about 6% compared with the third valence band of model I. The charge for valence band 4 is again almost unaffected by the change in V_8.

The charge density given in Fig. 9 is not precisely the charge density that our model potential would have at 0°K. The Fermi level is somewhere between the $L_{3'}$ and $\Gamma_{25'}$ levels so that a region around $\Gamma_{25'}$ in the third and fourth bands is unoccupied. Since the wave functions near $L_{3'}$ are very similar to those near $\Gamma_{25'}$, we do not expect that Fermi-level corrections will be very important.

It is interesting to compare the band structure of lead, assuming it could crystallize in the diamond structure, with the results of model III. To do this, we have calculated the band structure using the Heine-Animalu pseudopotential for lead. The lattice constant is chosen so that the nearest neighbor distance, d, in our hypothetical phase for Pb is the same as the nearest neighbor distance in its fcc phase. The justification for this choice is that when Si and Ge undergo a metallic phase transformation under pressure, the nearest neighbor distance is almost unchanged. The band structure obtained in this manner is similar to that of model III.

Fermi-Thomas model. In the Fermi-Thomas approximation, the pseudopotential is given by

$$v(q) = -\frac{8\pi e^2 Z}{\Omega(q^2 + k_s{}^2)} = -\frac{2}{3} E_F \frac{k_s{}^2}{(q^2 + k_s{}^2)} \quad .$$

Here Ω is the volume of the primitive cell, Z the number of outer electrons per atom and for Ge $\frac{2}{3}E_F = 0.57$ Ryd. Since the Fermi-Thomas potential is attractive for regions even close to the cores, (no orthogonalization conditions have been imposed on the valence electrons), the electrons tend to pile up in the core region. This is reflected in the energy band structure obtained for this model shown in Fig. 10. The states in the first two s-like bands are separated by a gap of 20.5 eV from the rest of the states in the valence band. These states behave essentially like core states and are not available for the formation of sp^3 orbitals. The band structure is that of a semimetal (or metal) with a large overlap. As in model III we have not computed the effects of overlap on the charge density, hence the charge density shown in Fig. 11 is approximate. Nevertheless, since the charge distribution in the first two bands is highly peaked around the atoms, and bands 4 and 5 add an almost constant background to the total charge density when compared to the first two, we expect that Fermi level corrections would not affect appreciably the total charge density. The main point is that the repulsive potential is too weak to keep the electrons outside the atoms and the formation of sp^3 orbitals is not energetically favored.

C. Summary and Conclusions for Model Potential

With a simple two parameter model pseudopotential with one variable parameter, it has been possible to simulate the variations observed in the group IV elements. A comparison between our results for model I and model II shows how a decrease in the repulsive part of the potential can take into account the main differences in band structure and bonding properties between Ge and gray Sn. Of course this model is too crude to include all the band structure features of these elements, but we believe that the main trends going from Ge to gray tin are explained by a reduction in the contributions from the repulsive orthogonalization requirements (V_8) to the pseudopotential.

Assuming that we could construct two diamond type crystals, one of Ge and the other of Pb with the same interatomic distances, the major difference in their pseudopotentials apart from screening effects would come from the orthogonalization conditions imposed on the pseudowavefunctions from the two different cores of Ge and Pb. That is, the main difference in the pseudopotentials would be inside an effective core radius r_0. This repulsive contribution to the pseudopotential would be mostly affected by the form factors V(q) for large q which we have included in only one variable parameter V_8. As the positive V(q) for large q decreases, the pseudopotential in real space becomes less repulsive allowing the electrons to concentrate in a region between the real core and our "effective core". If the electrons are too close to the cores, there are fewer electrons to form the bond, hence the bonds formed when the crystal is constructed are weak and the energy gain in the formation of the bonds might be smaller than the energy required to promote the electrons from the s^2p^2 ground state to the sp^3 configuration. The crystal would most likely change to a more stable configuration.

With respect to the band structure and electrical properties, since states near $\Gamma_{2'}$ and L_1 are concentrated close to the atoms, a decrease in the repulsive part of the pseudopotential affects them most. Therefore, decreasing the repulsive potential would decrease the potential energy of these states. Consequently, the first direct as well as the first indirect gap in the band structure would be decreased.

Because of this study using a two parameter model, which simulates the repulsive and attractive parts of the pseudopotential, we can understand and roughly predict the dependence of the total electronic charge density on the pseudopotential without going through a calculation of the energy band structure.

III. ZINCBLENDE STRUCTURE SEMICONDUCTORS

A. Empirical Pseudopotential Method for Zincblende Structure Semiconductors

In applying the pseudopotential method to obtain the electronic band structure for zincblende crystals, we have used the pseudopotential Hamiltonian of Section II but we have changed the structure factors to account for the two different atoms in the cell. The potential $V(\vec{r})$ is expanded in reciprocal lattice vectors and for convenience expressed in terms of a symmetric and antisymmetric part of the potential representing the sums and differences of the potentials of the two atoms in the unit cell,

$$V(\vec{r}) = \sum_{G} [V^S(|G|) \cos \vec{G}\cdot\vec{\zeta} + iV^A(|G|) \sin \vec{G}\cdot\vec{\zeta}] e^{-i\vec{G}\cdot\vec{r}} \qquad (6)$$

where $\vec{\zeta} = \frac{1}{8} a(1,1,1)$, a is the lattice constant. We still make the approximation $V(|G|) = 0$ for $G^2 \geqslant 12$ and the only form factors which enter in the calculation are $V^S(\sqrt{3})$, $V^S(\sqrt{8})$, $V^S(\sqrt{11})$, $V^A(\sqrt{3})$, $V^A(2)$ and $V^A(\sqrt{11})$. These six form factors are determined empirically using the reflectivity $R(\omega)$ and modulated reflectivity $R'(\omega)/R(\omega)$ experimental spectra.[6,7]

Using as our starting point the six form factors given by Cohen and Bergstresser,[4] we have calculated the band structure at many points in the Brillouin zone. With these values of $E(\vec{k})$ and the calculated dipole matrix elements, we have calculated the imaginary part of the dielectric function. This calculation is described by Walter and Cohen,[6,7] in which $\varepsilon_2(\omega)$ is obtained at low energies assuming transitions between the three highest valence bands and the six lowest conduction bands. A tail function of the form $\beta\omega/(\omega^2 + \gamma^2)^2$ is used at high energies to take into account high energy transitions. This tail function starts at 8.3 eV, β is determined from continuity and $\gamma = 4.5$. From $\varepsilon_2(\omega)$ the real part of the dielectric function is obtained by a Kramers-Kronig transformation and from these two functions we obtain the reflectivity $R(\omega)$ and the modulated reflectivity $R'(\omega)/R(\omega)$. The theoretical $R'(\omega)/R(\omega)$ curve obtained from Cohen and Bergstresser pseudopotential form factors show the same main structure as the experimental curves for zincblende semiconductors; thus the most important identifications are easily made.

In order to get better agreement with experiment, the main structure observed in the reflectivity curve is shifted. The method of adjusting the values of the form factors has been described by Walter and Cohen.[6,7]

To determine the transitions responsible for structure in the $\varepsilon_2(\omega)$ curve, we first find the energy of a particular peak. From our tabulated interband contributions to $\varepsilon_2(\omega)$ we are then able to determine which interband transition gives rise to the main contribution to this peak or shoulder. Once the interband transition has been identified, we determine where in the Brillouin zone a critical point appears with the required energy difference and large oscillator strength. The final proof that our identification is correct is made by varying the form factors by a small amount and observing the change in the energy gap, because the energy change for the chosen transition should be the same as the change in position of the peak. Since the procedure involves fitting direct gaps in the band structure to the experimental values, we think that this procedure gives direct transitions which are accurate at the important points in the Brillouin zone.

The crystals under consideration are InP, GaP, InSb and InAs. In InSb and InAs, spin orbit interactions are large and easily observable in the $R(\omega)$ experimental curves while in InP and GaP the effect is much smaller though observable in modulated reflectivity experiments. For this reason, the spin orbit interaction is included for InSb and InAs calculations; the method is that of Weisz[8] as modified by Bloom and Bergstresser.[9]

Two spin-orbit parameters are used to characterize the spin-orbit interaction.[10] The metallic form factor is allowed to vary from its free atomic value, while the non-metallic parameter is constrained so as to maintain a constant ratio between the two parameters. This constant ratio is set equal to the ratio of the spin-orbit interactions for the two atoms as determined by Herman and Skillman.[11] Using this one arbitrary parameter, we are able to obtain the experimentally known splittings at Γ and L to within 0.05 eV.

Table II compares the Cohen and Bergstresser (CB) form factors[4] with those used in the present calculation. The pseudopotential form factors are changed by less than 0.055 Ry. In the CB calculations, the symmetric form factors of InSb were constrained to be the same as the form factors for Sn; the symmetric form factors for InAs were constrained to be the average of the form factors for Ge and Sn; for GaP, CB used a symmetric potential that is the average of Si and Ge; while for InP, the Ge symmetric potential was used. We did not impose this constraint in the present calculation.

B. Results

The calculated energy bands for InAs, InSb, InP and GaP are given in Figs. 12, 13, and 14. These are similar to other energy band calculations[9,12,13] for these materials. Using the calculated energy bands throughout the Brillouin zone, the imaginary part of the frequency-dependent dielectric function, $\varepsilon_2(\omega)$, can be computed.[3] This function can then be used to compute the reflectivity, $R(\omega)$, and the modulated reflectivity, $R'(\omega)/R(\omega)$ as shown in reference 3. The sharp structure in $\varepsilon_2(\omega)$, $R(\omega)$ and R'/R arises from Van Hove[14,3] singularities in the joint density of states between the valence and conduction bands. These singularities arise when the gradient with respect to $\vec{k}$ of the energy bands $E(k)$ are equal for the conduction and valence bands of interests. There are four types of singularities in three dimensions[3,14] a minimum M_0, a maximum M_3 and two saddle points M_1 and M_2.

Figures 15, 16 and 17 contain the theoretical imaginary part of the frequency dependent dielectric function for InAs, InSb, InP and GaP. The calculated and measured[15-18] reflectivities appear in Figs. 18, 19 and 20 for these crystals. The calculated and measured[22,18] modulated spectra for InAs, InSb, InP and GaP appear in Figs. 21, 22, 23 and 24. Tables III, IV, V and VI compare the energies of the prominent structure in the calculated and measured curves for InAs, InSb, InP and GaP. These tables also give the origin in the Brillouin zone for the interband transitions which give rise to the optical structure, the critical point (cp) energy, i.e. the interband energy at which a Van Hove singularity is found, and the symmetry of the associated Van Hove singularity. In some cases a cp is not discernible, and the structure arises from transitions in a volume of the zone; these are labelled in the tables.

The four crystals will be discussed separately.

InAs

The first direct gap (Fig. 1) is $\Gamma_8 - \Gamma_6$.[19] The measured gap is 0.42 eV;[20] the Γ spin-orbit splitting ($\Gamma_7 - \Gamma_6$) is also 0.42 eV.[21,22] The spin-orbit splitting near $L(L_6 - L_4, L_5)$ is 0.27 eV.[22] In the calculated curves the spin-orbit parameter for In was adjusted to give a L splitting of 0.27 eV. The calculated splitting at Γ is 0.40 eV.

The calculated $\Gamma_8 - \Gamma_6$ transitions give rise to the M_0 threshold in $\varepsilon_2(\omega)$, (Fig. 15), at 0.46 eV. The $\Gamma_7 - \Gamma_6$ threshold at 0.86 eV is hidden in the background. These transitions give rise to a slight bump in $R(\omega)$, (Fig. 18); however, both transitions show up in the calculated $R'(\omega)/R(\omega)$ spectrum (Fig. 21).

The first peak in $\varepsilon_2(\omega)$ occurs at 2.60 eV and is caused by L(4-5) and Λ(4-5) transitions.[19] The spin-orbit split peak at 2.90 eV is caused by L(3-5) and Λ(3-5) transitions. This structure gives rise to peaks in the reflectivity spectrum at 2.58 eV and 2.85 eV which agree favorably with the experimental values of 2.61 and 2.88 eV.

The small shoulder at 4.45 eV on the lower side of the main peak in $\varepsilon_2(\omega)$ is caused by (4-5) transitions at X and along Δ(3-5). The corresponding structure in the calculated reflectivity is at 4.47 eV, whereas the measured value is 4.58 eV. Δ(4-5) and Γ(4-6) transitions just below this energy show up in the experimental R'/R spectra at 4.39 eV and correspond to the small structure at 4.37 eV of the theoretical R'/R curve at 4.63 eV. Excitonic effects at Γ may enhance the experimental spectrum.

The main peak in $\varepsilon_2(\omega)$ occurs at 4.63 eV and this peak comes from Σ(4-5) transitions at 4.65 eV. Transitions near X(4-5) also add to the height of the main peak. The main peak in the calculated reflectivity occurs at 4.7 eV; the experimental value is 4.74 eV. On the high energy side of the main peak in $\varepsilon_2(\omega)$, there are two changes in slope at about 5.32 eV, and at 5.35 eV. The first structure comes from Δ(4-6) transitions at 5.25 eV; this structure is found in the calculated reflectivity at 5.3 eV, close to the experimental value of 5.31 eV. The second structure arises mainly from Δ(3-6) transitions at 5.39 eV. The peak in the calculated reflectivity occurs at 5.57 eV, while the measured value is 5.5 eV.

Critical points at Λ(4-7) and L(4-7) with energies of 5.91 eV and 5.96 eV cause the next peak in $\varepsilon_2(\omega)$. The peak in the calculated reflectivity occurs at 6.05 eV. The experimental value for this peak is 6.5 eV, and is obtained by correcting the original value of 6.4 eV at 300°K to the low temperature limit, the agreement here is only fair.

The next small peak in $\varepsilon_2(\omega)$ at 6.4 eV is caused by Λ(3-7) transitions of 6.23 eV. Its counterpart in the measured reflectivity is a broad peak at 6.44 eV, the experimental value for this peak is 6.8 eV. The last structure which can be accurately identified is the shoulder at 7.1 eV, coming from (4-7) transitions in the energy range near 7.1 eV. The peak in the calculated reflectivity occurs at 7.3 eV, the corresponding temperature adjusted experimental value is 7.1 eV.

InSb

The measured splitting of the first direct gap for InSb, $\Gamma_8 - \Gamma_6$ is 0.24 eV;[23] the spin-orbit splitting at the top of the valence band at Γ is 0.82 eV[24,22] and 0.50 eV[24,22] at L. The calculated band structure is plotted in Fig. 13; the $\Gamma_8 - \Gamma_6$ splitting is 0.23 eV. The spin-orbit parameter for In is adjusted to give a splitting of 0.82 eV at Γ and the calculated value at L is 0.55 eV.

The imaginary part of the dielectric function, the calculated reflectivity and the calculated modulated reflectivity are given in Figs. 16, 19, and 22 respectively. The $\Gamma_8 - \Gamma_6$ transitions give rise to the threshold in $\varepsilon_2(\omega)$ at 0.26 eV. The spin-orbit split transition $\Gamma_7 - \Gamma_6$ gives a small peak in $\varepsilon_2(\omega)$, but this is largely masked by fluctuations inherent in the calculation. Both contributions appear clearly in the calculated R'/R curve at 0.26 eV and 0.66 eV respectively.

The first peak in $\varepsilon_2(\omega)$ at 1.98 eV is caused by $\Lambda(4-5)$ transitions at 1.94 eV. The next peak at 2.6 eV is caused by $\Lambda(3-5)$ transitions at 2.5 eV. Associated with these structures are the spin-orbit split Λ peaks in the reflectivity at 2.03 eV and 2.6 eV. The positions of these peaks agree well with the experimental values of 1.98 eV and 2.48 eV.

The rise at 3.55 eV on the low side of the main peak in $\varepsilon_2(\omega)$ arises from (4-5) transitions in a volume located near Δ. At slightly higher energies near the main peak, there is a shoulder at 3.8 eV. This shoulder is caused by $\Delta(3-5)$ transitions at 3.83 eV. In the reflectivity spectrum, these features give rise to a shoulder at 3.65 eV and a shoulder at 3.83 eV. The experimental values are 3.39 eV and 3.78 eV.

The main peak in $\varepsilon_2(\omega)$ is caused primarily by $\Sigma(4-5)$ transitions at 4.1 eV. This structure gives rise to the peak at 4.01 eV in the reflectivity. This peak occurs lower in energy than at the experimental value of 4.23 eV.

The small structure and peak on the high side of the main peak in $\varepsilon_2(\omega)$ at 4.4 and 4.75 eV are caused by (4-6) transitions in a volume of k-space at about 4.4 eV and by $\Delta(4-6)$ transitions 4.75 eV. These are related to the two bumps in the reflectivity at 4.48 and 4.73 eV. These energies are in good agreement with the experiment.

The peak at 4.8 eV and the small shoulder at 5.09 eV in the $\varepsilon_2(\omega)$ curve are caused by $\Lambda(4-6)$, $\Delta(3-6)$ and $\Lambda(3-6)$ transitions at 4.87 eV, 4.94 eV and 5.43 eV. The related reflectivity structures are the broad peak at 5.3 eV with a highly blurred shoulder at 4.73 eV; the corresponding experimental values are at 5.33 and 4.92 eV.

The peak in $\varepsilon_2(\omega)$ at 5.73 eV arises mainly from $\Lambda(3-7)$ transitions at 5.69 eV. The peak in $R(\omega)$ is at 6.01 eV, in good agreement with the experimental value of 5.96 eV.

As for the $\Gamma_6^c - \Gamma_7^c$, $\Gamma_6^c - \Gamma_8^c$ doublet, electroreflectance measurements in n-type InSb[25] show two peaks at 3.16 and 3.54 eV with a red shift response to an increase of the surface potential; this structure disappears as the conduction band is depopulated. These two facts indicate that these two peaks come from transitions from the top of the conduction band (Γ_6^c) to higher conduction bands (Γ_7^c and Γ_8^c). Since these are s-like to p-like transitions, we expect that the oscillator strengths for these transitions are strong enough to be observable. Our calculated energy differences are

$$\Gamma_6^c - \Gamma_7^c = 2.43 \text{ eV}; \ \Gamma_6^c - \Gamma_8^c = 3.41 \text{ eV}$$

in fair agreement with the experimental values.

InP

The threshold in $\varepsilon_2(\omega)$ (calculated energies referred to in this section correspond to structure in $\varepsilon_2(\omega)$ unless otherwise noted) is caused by Γ_{15}- Γ_1 transitions at 1.50 eV. If spin-orbit corrections were included in our calculation, (Δ_0 = 0.21 eV), we would obtain the following energy difference:

$$(\Gamma_8 - \Gamma_6) = (\Gamma_{15} - \Gamma_1) - \frac{1}{3}\Delta_0 = 1.43 \text{ eV}$$

in good agreement with the measured value[26] of 1.42 eV. The rise and peak in the region near 3.35 eV is caused by $L_3 - L_1$ transitions at 3.2 eV (M_1 singularity) and $\Lambda_3 - \Lambda_1$ transitions near the point (0.3, 0.3, 0.3) at 3.22 eV (M_1 singularity). The main peak in the region of 4.9 eV is caused primarily by $\Sigma_2 - \Sigma_1$ transitions at (0.7, 0.7, 0.7) in the Brillouin zone (BZ) with an energy splitting of 5.02 eV (M_2 singularity). Some contribution comes from the 4.82 eV shoulder and these are attributed to Δ_5- Δ_1 transitions at 4.7 eV (M_0 singularity) and $X_5 - X_1$ transitions at 4.71 eV (M_1 singularity). The small shoulder in the calculated $\varepsilon_2(\omega)$ at 5.35 eV is caused by $X_5 - X_3$ 4-6 transitions having an energy difference of 5.29 eV (M_0 singularity); this structure does not appear in the $R(\omega)$ curve. The discontinuous structure in $\varepsilon_2(\omega)$ at 5.6 eV arises from a volume effect for transitions between the 3rd and 6th bands near the point (0.3, 0.1, 0); the reflectivity structure is at 5.48 eV. The peak at 5.82 eV comes from $\Delta_5 - \Delta_1$ transitions near the point (0.7, 0, 0) (M_1 singularity). Finally, the third prominent peak was caused by (4-6) transitions near L at 6.2 eV. Comparison of these last three structures with experiment is only fair.

The experimental reflectivity at 300°K is compared in Fig. 20 with our theoretical results for 5°K. The first peak after the small threshold structure in the experimental curve is at 3 eV while we predict a peak at 3.30 eV; the experimental shoulder near 4.8 eV corresponds to the 4.75 eV theoretical shoulder. The main experimental peak at 5.05 eV has its counterpart in the 5.06 eV calculated peak. Experiment 2 shows a small shoulder at 5.6 eV which corresponds to the calculated shoulder at 5.48 eV; the larger shoulder at 5.6 eV has its theoretical counterpart in the small peak at 5.86 eV. The last structure recognized in our theoretical calculation is a broad peak at 6.47 eV and this corresponds to the 6.57 eV experimental value. Each of the experimental structures up to 6.7 eV has its theoretical counterpart. The agreement in magnitude is reasonably good when compared with Cardona's[17] data except for the first peak which can be interpreted as excitonic enhancement of the experimental curve in this energy region. The difference in position of the peaks is due to the temperature difference between the data used for our calculation and the temperature of the experimental reflectivity curves; the 300°K curves shift to lower energy as expected.

In Fig. 23 we show a comparison between the $R'(\omega)/R(\omega)$ theoretical curve and the modulated reflectivity of Ref. 18 at 5°K. In this curve the agreement in the positioning of the peaks is very good as shown in Table V. Referring to these curves, we make two remarks: (1) if spin-orbit effects were included, the 3.30 eV peak coming from the $\Lambda_3 - \Lambda_1$ band would split into two peaks at 3.23 eV and 3.37 eV ($\Delta_1 = 0.14$ eV) corresponding to the peak and shoulder at 3.24 eV and 3.38 eV in the experimental curve; (2) the small shoulder at 5.48 eV of the theoretical curve may be associated with the small structure at 5.5 eV of the experimental curve; the structure would be almost unnoticeable in the corresponding reflectivity curve.

GaP

In Fig. 24 we show a comparison between the calculated modulated reflectivity curve GaP with experiment.[18] The calculations were done at an assumed temperature of 300°K. The calculated band structure, $\varepsilon_2(\omega)$, and $R(\omega)$ for GaP also appear in Ref. 4. Identifications of the important reflectivity structure is tabulated in Table II. The positions of the important reflectivity peaks are given by those zeroes of $R'(\omega)/R(\omega)$ at which the slope is negative. The other structure appearing in the derivative spectrum is much finer; some of the details are practically imperceptible when seen in the normal reflectivity spectrum.

The fundamental gap in GaP is the indirect $\Gamma_{15} - X_1$ gap. The calculated value is 2.19 eV and the experimental value is 2.22 eV, as determined by absorption and recombination radiation experiments.[27] The smallest direct gap occurs at Γ at 2.79 eV for theory and at 2.78 eV for experiment. The major structure in the 3.4 - 3.9 eV region is a reflectivity peak centered at 3.68 eV caused by $\Lambda(4\text{-}5)$ and $\Lambda(3\text{-}5)$ transitions. The theoretical peak in the reflectivity occurs at 3.70 eV, giving excellent agreement with experiment. The next major reflectivity peak occurs at 5.31 eV in the experimental measurements and at 5.3 eV in the theoretical calculations. This peak is caused by a combination of $\Sigma(4\text{-}5)$, $\Delta(3\text{-}5)$, and $\Delta(4\text{-}5)$ transitions, all with large oscillator strengths. The fine structure in this region consists of a reflectivity shoulder at 4.74 eV caused by Δ(4-5) and X(4-5) transitions. This shoulder occurs in the calculated reflectivity at about 4.7 eV.

Most of the above assignments for the four semiconductors studied in this work are consistent with those of refs. 3, 22 and 31.

Indirect Gaps (InP and GaP)

For GaP as well as InP we have obtained a very good agreement between measured and calculated reflectivity and modulated reflectivity. The fitting is good enough to indicate that our identifications of the important direct transitions in the reflectivity experiments are correct and that our band structure is accurate with respect to direct transitions.

In GaP the minimum gap is the indirect $\Gamma_{15} - X_1$ gap. This transition has been determined experimentally by absorption and recombination radiation experiments[27] and it is found to be 2.22 eV while our calculated value is 2.19 eV; in these experiments Zallen and Paul also determine the pressure dependence of this gap and of the $\Gamma_{15} - \Gamma_1$ direct gap (the experimental value of the $\Gamma_{15} - \Gamma_1$ being 2.78 eV in agreement with the calculated value of 2.75 eV). The measured pressure coefficients are $dE(\Gamma_{15} - \Gamma_1)/dP = 10.7 \pm 10\% \times 10^{-6}$ eV/bar and $dE(\Gamma_{15} - X_1)/dP = -1.1 \pm 10\% \times 10^{-6}$ eV/bar. We have calculated the pressure coefficients for these gaps; our results are as follows: $dE(\Gamma_{15} - \Gamma_1)/dP = 12.6 \times 10^{-6}$ eV/bar; $dE(\Gamma_{15} - X_1)/dP = -1.0 \times 10^{-6}$ eV/bar in good agreement with the experimental values. The calculation involves the evaluation of the change in energy levels with small changes in lattice constant (see part III). The measured compressibility was also used in the calculation.

For InP a direct measurement of the $\Gamma - X$ indirect transition has not been performed. One possibility for obtaining this value arises from what Paul[28] calls "the empirical rule" which says that all the gaps in III-V and II-VI semiconductors have roughly the same pressure dependence. The pressure coefficient of the direct gap between the Γ_{15} valence band and the Γ_1 conduction band is of the order of 10×10^{-6} eV/bar and the pressure coefficient of the $\Gamma_{15} - X_1$ indirect gap is roughly -1×10^{-6} eV/bar. Our calculated values for this crystal are: $dE(\Gamma_{15} - \Gamma_1)/dP = 9.24\text{x}10^{-6}$ eV/bar; $dE(\Gamma_{15} - X_1)/dP = -1.26\text{x}10^{-6}$ eV/bar. At sufficiently high pressure (> 50 k bar) the indirect $\Gamma_{15} - X_1$ gap will become the smallest gap and therefore directly observable.

Another possibility is explored by Hakki et al.;[29] in these experiments they combine pressure and composition dependence on In-GaP alloys. Using Paul's "empirical rule" they are able to identify the smallest gap for a given composition as a function of pressure; then from extrapolation, they determine the variation with composition of the $\Gamma_{15} - X_1$ gap at zero pressure. A linear extrapolation of the $\Gamma_{15} - X_1$ gap to the InP side gives a value of 2 eV. The extrapolated pressure coefficient for this gap is -1.1×10^{-6} eV/bar. We think that the conclusions of Hakki et al. are correct;[30] our calculated value for this gap at 5°K is 2.84 eV. To compare the band structure calculation with experiment for the indirect gaps, we have introduced a k^2 dependent term in our band structure as shown by the dotted line in Fig. 14. The expression used is $E(\vec{k}) = E_{EPM}(\vec{k}) - \gamma k^2$; γ is adjusted to give the experimentally determined $\Gamma_{15} - X_1$ gap, and its value is $\gamma = 0.743$ ev Å. Writing

$-\gamma = \hbar^2/2m'$ and $1/m^* = 1/m' + 1/m_e$, we find that our correction may be thought of as a mass renormalization with $m^* = 1.22\ m_e$.

C. Electronic Charge Densities for InAs and InSb

We have solved the secular equation for the pseudopotential Hamiltonian for the wavefunctions $\psi_{n,k}(r)$ on a grid of 3360 points in the Brillouin zone (n is the band index)[21] for InAs and InSb. From these wavefunctions we obtain the charge density in each valence band as

$$\rho_n(\vec{r}) = \sum_{\vec{k}} e|\psi_{n,\vec{k}}(\vec{r})|^2 \ . \qquad (7)$$

Figures 26 and 27 show the contour maps of the sum over the first four valence bands for InAs and InSb respectively, for the plane (1, -1, 0) as shown in Fig. 25. The density is plotted in units of (e/Ω) where Ω is the volume of the primitive cell, $\Omega = a^3/4$.

Our results are consistent with the fact that InAs is a more ionic cyrstal than InSb,[1] the charge being more piled up towards the As atom in InAs than towards the Sb atom in InSb.

The form factors used here for InSb are different from those used in ref. 21 and give a much better agreement with the optical data. We have calculated the covalent bonding charge Z_b as described in Ref. 21. Our result is $Z_b = 0.083e$. When this result is plotted using Phillips and Van Vechten[1] ionicity scale with earlier results for Sn and CdTe, the curve of bonding charge versus ionicity is more linear, but the extrapolated value of the critical ionicity f_c does not change when compared with the results of Walter and Cohen.[2]

The value for Z_b we obtain for InAs is 0.069e. When this is plotted vs. the ionicity scale of Phillips and Van Vechten, this point lies very near the curve of the Ge family of Walter and Cohen.

IV. PRESSURE DEPENDENCE OF ELECTRONIC STATES

A. Hydrostatic Pressure Dependence of Electronic Properties of zb and Diamond Type Crystals (Transferability of the Pseudopotentials)

A large number of hydrostatic pressure experiments[28] have been carried out on the germanium family; from them, the following rough empirical rule is found: the pressure coefficient of the energy difference between two states of given symmetry is roughly independent of the material in which the pressure coefficient is measured. As mentioned in Chapter III of this work, this empirical fact tells us, for example, that the first absorption edge of GaP at atmospheric pressure is a $\Gamma_{15} - X_1$ transition. Moreover, pressure experiments can give us information about transitions that are otherwise rather inaccessible at normal pressure conditions.

Here, we present our theoretical results for the pressure coefficients for some important gaps in the electronic band structures of Si and InP. The method used is again the EPM. The application of an external pressure modifies the pseudopotential form factors (and through them the electronic band structure $E_n(\vec{k})$) in the following ways:

(1) A change in the lattice parameter a varies the atomic volume so that v(G) has to be scaled with inverse volume.

(2) A change in a varies the value of the reciprocal lattice vectors $\vec{G}$ at which v(G) has to be evaluated.

(3) A change in atomic volume is also expected to affect the screening of the valence electrons which in turn affects the functional dependence of v(G). This effect is only big for small values of the wave vector q and of little importance for $\vec{G} \neq 0$.

From 1, 2 and 3, we see that in order to study the change in band structure with lattice parameters, it is necessary to know the complete pseudopotential function v(q). In this paper we used the empirical approach to determine the slopes of v(q) at the reciprocal lattice vectors $\vec{G}$ at atmospheric pressure. The procedure is as follows: the pseudopotential curves were freehand extrapolated from their known values at atmospheric pressure. From the extrapolated curves the values of important gaps were obtained at 10 k bars (here we use the known compressibility of the semiconductor in question) and small adjustments to the extrapolation were made in order to have better agreement with experiment (at 10 k bars we are dealing with very small energy changes $\lesssim$0.1 eV, thus the results are very sensitive to the scaling). It is known that under very high pressures Si undergoes a phase transformation to a metallic phase similar to that of white tin while InP undergoes a phase transformation to an insulating phase with rock salt structure. Thus we are interested to explore whether our simple method predicts a trend towards metallization for Si under high pressure and if the charge density for InP becomes more ionic as pressure is applied. To do this, we adjusted a polynomial curve to the v(q)'s from the known values at the reciprocal lattice vectors at atmospheric pressure and at 10 k bars. Our results are given separately in the next section for the two crystals.

In EPM calculations, the importance of pressure experiments rests not only in the positive identification of important optical transitions in the electronic energy band structure of semiconductors, it also provides information on the scalling of the pseudopotential form factors. It is expected that the scaling that reproduces the pressure data for

Si will give very good results when used to predict the band structure of Si in its wurtzite crystalline phase.[3] If in addition we know how to scale P form factors from GaP pressure experiments and Zn form factors from ZnS pressure experiments, we are in a position of predicting the electronic properties of the chalcopyrite compound $ZnSiP_2$.

B. Results

Si

Silicon is one of the solids for which the electronic band structure is best known; in addition, experimental data on Si under pressure[28] is readily available. Our calculated results are summarized in Fig. 28. The form factors for Si at 0 and 20 k bar pressure are (in Ry)

$$v(3) = -.21 \qquad v(8) = .04 \qquad v(11) = .0800$$

and

$$v(3) = -.2092 \qquad v(8) = .044 \qquad v(11) = .0816$$

respectively. In zincblende and diamond crystals, special attention has been paid to the study of the pressure coefficients of the first three valleys in the conduction band with respect to the top of the valence band at Γ. In Si these three valleys have symmetry, L_1, Δ_1 and Γ_{15}. Our calculated values for these pressure coefficients are in 10^{-6} ev/bar

$$\frac{dE_{\Gamma-L}}{dP} = 4.4 \qquad \frac{dE_{\Gamma-\Gamma}}{dP} = -0.7 \qquad \frac{dE_{\Gamma-X}}{dP} = -1.6$$

while the experimental value for $\frac{dE_{\Gamma-X}}{dP} = -1.5 \times 10^{-6}$ ev/bar. The pressure dependence of the Γ-L transition is $\sim 5 \times 10^{-6}$ ev/bar for all zb and diamond crystals measured. According to the empirical rule, the pressure coefficient for the $\Gamma_{25}' - \Gamma_2'$ transition in zb and diamond crystals is $\frac{dE(\Gamma_{25}' - \Gamma_2')}{dP} \sim 10 \times 10^{-6}$ eV/bar (for Ge is 14×10^{-6} eV/bar) our calculated value is 13.4×10^{-6} eV/bar.

From the above theoretical and experimental results, it is clear that the pressure coefficients are quite sensitive to the symmetry of the wave functions. In Fig. 29 we show the absolute value of these wave functions as a function of position in the unit cell along the (1, 1, 1) direction. From this figure, we notice that the Γ_2' wave function is highly peaked near the atoms, the L_1 wave function is broader and peaked between the atoms and the antibonding site, the Γ_{15} wave function is concentrated at the antibonding site and the X_1 wave function is almost constant with a slight build up farther away from the antibonding site. As for the pressure coefficients, the $\Gamma_{25}' - \Gamma_2'$ transition increases in energy at a high rate, the $\Gamma_{25}' - L_1$ transition increases at a slower rate while the $\Gamma_{25}' - \Gamma_{15}$ and $\Gamma_{25}' - X_1$ transitions decrease at a small rate. So there is a correlation between pressure coefficients and the quantity

$$\sigma_k^2 = \int_{\substack{\text{primitive}\\\text{cell}}} r^2 \, \rho_k(r) \, d^3r \qquad (8)$$

which measures the dispersion of the charge density of the k-state from the bonding site. The pressure coefficient of the transition $\Gamma_{25}'^{\,v} - k^c$ is a decreasing function of σ_k^2, k^c is a state in the conduction band with wave vector $\vec{k}$.

As for the important direct transitions (the ones that give the biggest contribution to the reflectivity spectra), L_1-L_3 and X_4-X_1, our calculated value for the pressure coefficients are:

$$\frac{dE\ (L_1-L_3)}{dP} = 5.7 \times 10^{-6}\ \text{eV/bar}$$

$$\frac{dE(X_4-X_1)}{dP} = 2.1 \times 10^{-6}\ \text{eV/bar}$$

this last coefficient in fair agreement with the experimental value of $2.9 \pm 0.6 \times 10^{-6}$ eV/bar for the pressure coefficient of the main E_2 peak in reflectivity spectra.

The fact that negative pressure coefficients (with respect to the top of the valence band) are found for antibonding s-like states (Γ_{15}) and quasi-metallic states (X_1) in the conduction band, indicates that the total charge density $\rho(r)$ in the valence band becomes more metallic as hydrostatic pressure is applied. To show this, we calculated the charge density in our model for 120 k bars of pressure. The charge density is calculated using the representative k-point used by Baldareschi.[51] This method is discussed in Appendix A. The charge densities as functions of position in the (011) plane for 0 and 120 k bars of pressure are shown in Fig. 30. The results at 0 pressure are those of Walter and Cohen.[2] The bonding charge in Si 120 k bar is about 20% smaller than that at 0 pressure indicating a definite trend toward metallization. No attempt was made to compare them exactly, because Walter and Cohen's results were obtained in a band by band analysis which is not possible using a representative k-point in calculating the charge density, mainly because the accuracy of the method for individual bands is not as good as that for the sum over the valence bands (∿3%).

Results InP

InP is the only zb semiconductor of the III-V group that transforms to a rock-salt structure under hydrostatic pressure. In the Phillips[1] ionicity scale, the value of the ionicity for InP draws a limit between tetrahedrally coordinated compounds that transform into a metallic phase and those that transform into a NaCl structure, under pressure. The Γ_{15}-Γ_1 and Γ_{15}-X_1 coefficinets of InP are relatively well established, the experimental values are:[28,29]

$$\frac{dE}{dP}(\Gamma_{15}-\Gamma_1) = 8.7 \times 10^{-6}\ \mathrm{eV/bar},\quad \frac{dE}{dP}(\Gamma_{15}-X_1) = -\ 1 \times 10^{-6}\ \mathrm{eV/bar}$$

our theoretical results give

$$\frac{dE}{dP}(\Gamma_{15}-\Gamma_1) = 9.24 \times 10^{-6}\ \mathrm{eV/bar},\quad \frac{dE}{dP}(\Gamma_{15}-X_1) = -\ 1.26 \times 10^{-6}\ \mathrm{eV/bar}$$

Our calculated pressure coefficient for the main reflectivity peak X_5^{v}-X_1^{c} is 2.21 x 10^{-6} eV/bar. The form factors used at 10 k bar are

$V_s(3) = -.271 \qquad V_s(8) = .0364 \qquad V_s(11) = .044$

$V_A(3) = .0887 \qquad V_A(4) = .0887 \qquad V_A(11) = .0306$

The 0 pressure form factors are those of part II of this work.

In Figs. 31 and 32 we plot our calculated charge density for InP at 0 and 100 k bar pressure; the only observed trend as pressure is applied is that of metallization, contrary to what one would expect from the transformation properties of InP under hydrostatic compression. At this point, we can only speculate on the various possible explanations for this result.

(a) The scaling of the pseudopotential form factors is not correct; in this case more experimental information about the pressure dependence of the band structure is needed.

(b) The local approximation for the pseudopotential of InP breaks down. As we pointed out in Section II, a local pseudopotential fails to predict the energy of indirect gaps if the empirical rule is correct.

(c) Assuming that the empirical rule is correct, the fact that the pressure dependence of the energy gaps between the fourth valence band and the first conduction band is essentially the same for all zb semiconductors whether they transform to a metallic or a rock salt crystalline structure under pressure, seems to indicate that the bonding properties of these semiconductors under pressure are not only associated with the pressure properties of $\varepsilon_2(\omega)$

V. CHALCOPYRITE CRYSTALS

Recently much attention has been given to studies of electronic and optical properties of ternary compounds with chemical formula $A^{N-1} B^{N+1} C_2^{8-N}$ (N = 3,2). Theoretically, the study of the electronic and optical properties of these compounds is a logical extension of the study of their closest analogs, the $B^N C^{8-N}$ (N = 3,2) zincblende semiconductors. The $A^{N-1}B^{N+1}C_2^{8-N}$ have many interesting physical properties which promise to be useful for studies of the electronic properties of semiconductors in general and for applications in semiconductor technology.

In the case N = 3 most of these ternary compounds crystalize in the chalcopyrite structure which is a simple generalization of the zincblende crystal structure. We know from the work of Cohen and Bergstresser[4] and Phillips and Van Vechten that most of the electronic and optical properties of the B^3C^5 zincblende semiconductors are analogous to those of the diamond structure semiconductors (group B^4). Some modifications exist when the effects of the anion and cation difference are introduced into the band structure and bonding properties. In the same way, most of the properties of $A^2B^4C_2^5$ chalcopyrite semiconductors can be understood by introducing the effects of the two cation differences into the band structure of their zincblende analog. In Section A of this chapter, we study the chalcopyrite crystal structure in detail with emphasis on how systematic trends in the lattice parameters give us information about the bonding properties of these crystals. In Section B we describe in detail the Brillouin zone of the chalcopyrites and its relation to the zincblende Brillouin Zone. In Section C we present our results for the imaginary part of the dielectric function, $\varepsilon_2(\omega)$, the reflectivity $R(\omega)$ and the density of states $D(\omega)$ for the chalcopyrite compound $ZnGeP_2$. In concurrence with the analysis of our results for this particular semiconductor, we have discussed the common features in $\varepsilon_2(\omega)$, $R(\omega)$, and $D(\omega)$ which are characteristic of many of the $A^2B^4C^5_2$ semiconductors.

In Section D we present the details of the band structure calculation of $ZnGeP_2$ and $ZnGeAs_2$.

A. Chalcopyrite Crystal Structure

The chalcopyrite crystal structure of a compound with formula $A^{N-1}B^{N+1}C^{8-N}_2$ has a body centered tetragonal unit cell with 8 atoms per primitive cell at positions given by:

A^2 at $(0,0,0)$, $(0,a/2,c/4)$

B^4 at $(0,0,c/2)$, $(0,a/2, 3\,c/4)$

C^5 at $(au,a/4,c/8)$, $(a\bar{u},3a/4,c/8)$, $(3a/4,au,7c/8)$, $(a/4, a\bar{u},7c/8)$

The space group is the nonsymmorfic group D_{2d}^{12} and the unit cell can be thought of as composed of two zincblende unit cells stacked and compressed along the z-axis. The cation of the zincblende is substituted by the two cations of the chalcopyrite is such a way that two kinds of chains are formed. A-C-B-C-A chains run along the (1,±1,0) directions while A-C-A-C-B-C-B-C-A chains run along the (0,±1,1) and (±1,0,1) directions; the presence of A-C-A and B-C-B linkages running along the z-axis is responsible for the doubling of the unit cell with respect to the zincblende case.

The tetragonal compression given by $2 - c/a = \varepsilon$ is always positive or zero for the chalcopyrite compounds with $N = 3$ and runs from a value of 0.242 for $MgSiP_2$ to 0 in $ZnSnP_2$ (see Table VII).

The anion of a chalcopyrite compound is tetrahedrally coordinated to two cations of type A and two cations of type B and slightly displaced from its original zincblende position towards the smallest pair of cations; this displacement can be measured by the parameter $\sigma = 4u - 1$. The parameter σ can be positive or negative depending on which of the two cations is the smallest; the largest measured distortion is for $CdGeAs_2$ for which $\sigma = 0.144$; the value of this parameter for the ZnSn compounds ($ZnSnP_2$ and $ZnSnAs_2$) is negative ($\sigma = -0.044$).

In Table VII[33] we give the crystal parameters for these compounds; from it, several trends can be observed: both the tetragonal distortion ε and the displacement of the anion σ seem to depend mostly on the two cations of these ternary compounds; both ε and σ are slightly larger for the phosphides than for the arsenides. In the Zn compounds for which the table is more complete, the parameter $|\varepsilon - 4\sigma|$ is an increasing function of the row number of the second cation.

To study this trend more closely, let's take the difference between the AC and BC bond lengths to first order in ε and σ:

$$D = |\overline{AC}| - |\overline{BC}| = a\left\{\left[\left(\frac{\sigma+1}{4}\right)^2 + \left(\frac{1}{4}\right)^2 + \left(\frac{2-\varepsilon}{8}\right)^2\right]^{1/2} - \left[\left(\frac{\sigma-1}{4}\right)^2 + \frac{1}{4} + \left(\frac{2-\varepsilon}{8}\right)^2\right]^{1/2}\right\} \tag{9}$$

$$\simeq \frac{2}{\sqrt{3}}\,\sigma a \quad . \; . \; .$$

i.e., $\frac{D}{a}$ is a direct measure of the crystal parameter σ. This explains one of the observed trends, if D is very weakly dependent on the anion, σ should be a decreasing function of lattice constant. It is thus smaller for the arsenides than for the phosphides given the same pair of cations. In Table VIII we compare the experimental values of σ with those obtained from the additive radii of atoms (when in tetrahedral covalent bonds) of Pauling[34] and Phillips and Van Vechten.[35] The agreement between the experimental values of σ with those predicted using Pauling's radii is better than 25% while those predicted using Phillips and Van Vechten are much worse. The difference between the experimental values of σ and those predicted using Pauling's radii seems to indicate that, for example, the Zn - P bond is more ionic in $ZnSiP_2$ than in $ZnGeP_2$ and that the Sn - As bond is more ionic in $ZnSnAs_2$ than in $CdSnAs_2$. S. C. Abrahams and J. L. Bernstein[36] have pointed out that in the $A^2B^4C^5_2$ compounds, the B cations are tetrahedrally coordinated to within 0.3°, while the tetrahedral coordination of the A cations may be deformed by more than 10° from their studies on $ZnSiP_2$ and $CdSiP_2$. Again, to first order in σ and ε, these angles are given by

$$\left.\begin{aligned} \cos(\sphericalangle CAC) &\sim \frac{1}{3}(-1 + \quad \alpha(\varepsilon + 4\sigma)) \\ \cos(\sphericalangle CBC) &\sim \frac{1}{3}(-1 + \quad \alpha(\varepsilon - 4\sigma)) \end{aligned}\right. \quad \alpha = 2/3,\ -4/3 \qquad (10)$$

So the B cation is perfectly tetrahedrally coordinated if $\varepsilon \sim 4\sigma$ the trend observed in the Zn compounds in the quantity $|\varepsilon - 4\sigma|$ only reflects what we already know i.e., that Si is more covalent than Ge and the latter is more covalent than Sn. The crystal is constructed in such a way that increasing the distortion of the tetrahedral arrangement around the A cation tends to decrease the distortion around the B cation; the fact that $\varepsilon = 0$ for the ZnSn compounds probably indicates that both linkages CAC and CBC are equally covalent.

B. The Relation Between the Zincblende Brillouin Zone and the Chalcopyrite Brillouin Zone

Since the primitive cell of a chalcopyrite crystal is four times larger than the primitive cell of a zincblende crystal compressed along the z axis, the zincblende Brillouin zone is four times larger than that of the chalcopyrite analog. The two crystal structures are so similar, that it is possible to completely fold in the zincblende zone four times into the chalcopyrite zone.

Some of the ternary crystals with composition $A^2B^4C^5_2$ (e.g., $MgGeP_2$), lack the segregation of its two cations. The cations are considered randomly distributed among the cation position in the Zb analog. Then the compound has the zincblende structure, one of the two sites in the primitive cell is occupied by the anion and the other by an average of the two cations $\left(\frac{A^2+B^4}{2}\right)$. It is only the ordering of the two cations and their different potentials what reduces the Brillouin Zone. In view of this, it is expected that the electronic and optical properties of a chalcopyrite crystal should be very similar to those of their zincblende analog. This is even more convincing if one takes into account the fact that the average cation pseudopotential in a chalcopyrite crystal is very close to the pseudopotential of the cation in its zincblende analog. In the folding in process of the band structure of a zincblende crystal into the chalcopyrite Brillouin Zone, singly degenerate states may now be double, triple or quadruple. If the differences in the two cation pseudopotential, represented by an antisymmetric cation potential $V_A^c = \frac{V(A^2) - V(B^4)}{2}$, lifts the degeneracy, simple perturbation theory predicts that these states are going to be the most affected by the ordering of the two cations and by the antisymmetric cation potential.

In Fig. 38, we show the irreducible part of the chalcopyrite Brillouin zone; the labeling of symmetry points and symmetry directions is that of Zak.[50] In Figs. 34 and 35 we show the folding in process of the zincblende BZ into two different planes of the chalcopyrite BZ. The smallest G vectors in the chalcopyrite structure are of the form $2\pi(0,0,2/c)$, $2\pi(0,1/a,1/c)$ and $2\pi(1/a,0,1/c)$; for $c = 2c'$ where c' is the z lattice vector of the compressed zincblende analog, these G vectors correspond to the points X, W_x, W_y of the zincblende Brillouin zone. In Fig. 34, the planes $k_z = 0$ (Fig. 34a), $k_z = +1$ (Fig. 34b) and $k_z = +1$ (Fig. 34c) of the zincblende BZ map into the plane $k_z = 0$ of the chalcopyrite BZ, the translation vectors are $2\pi(0,0,0)$, $2\pi(0,0,1/c')$, $2\pi(1/a,0,1/2c')$ and $2\pi(0,1/a,1/2c')$ respectively. The last two translations are completely equivalent in this case so that while the points X and Γ that map into Γ have the same degeneracy as in the zb case, the point W now is double degenerate and also maps into Γ. In what follows k_x and k_y are in units of $2\pi/a$ and k_z in units of $2\pi/c'$: $(c = 2c')$. Figure 34d shows the $k_z = 0$ plane of the chalcopyrite BZ. In Fig. 34e we show the planes (Figs. 34a, 34b and 34c) appropriately displaced to show the folding in process. The points marked by X in Figs. 34a, 34b and 34c are those that map into Γ of Fig. 39d. σ represents the points of the form (1/2,1/2,0) and δ points of the form (1/2,0,0) of the zb BZ.

From Fig. 34d we see that the Σ direction in the chalcopyrite BZ, now contains the Σ_{xy} and S directions of the zb analog (Γ - σ and X→U, K → σ) and the double degenerate Q direction (W→L). The Δ and S chalcopyrite directions now contain the original Δ direction plus the Z direction (X_z - W_z - X_z) and the doubly degenerate W - δ direction (along (x,0,1/2)). Finally, in this plane, the Y and U directions contain the doubly degenerate σ to X line (along (1 - x,x,0)) and the double line L - δ along (x,x,1/2). In Fig. 35, we show the folding in process for the N plane ($k_x = k_y$) of the chalcoyprite BZ; Figs. 35a and 35b, show the $k_x = k_y$ and $1 - k_x = k_y$ planes of the zb BZ again the points marked by X map into Γ of the chalcopyrite BZ, Fig. 35c shows the N plane of the chalcopyrite BZ. In Fig. 35d, the direction Γ - X (along $k_x = k_y = k_z$) contains the original Λ direction of the zb BZ together with the lines X - L (along $(k_x,k_x,1 - k_x)$) and W - Σ (along $(k_x,1 - k_x,1/2 - k_x)$). Besides the important high symmetry point X (with degeneracy 2n, where n is the degeneracy in the zb case), there are two interesting points in this plane, the point A (1/2,1/2,1/4) whose degeneracy is 4 when the antisymmetric cation potential is zero and splits into two doubly degenerate levels when this potential is turned on, and the point (1/4,1/4,1/4) that contains singlets and triplets (corresponding to (1/4,1/4,1/4) (3/4,1/4,1/4) (1/4,3/4,1/4) and (1/4,1/4,3/4) in the zb case) and is the representative k-point for charge density for body centered tetragonal structures (see Appendix A and references therein).

C. Electronic and Optical Structure for the Chalcopyrites

In Fig. 36a, we show our calculated band structure for the chalcopyrite compound $ZnGeP_2$ and in Fig. 36b that of its stressed analog. This last band structure corresponds to that of GaP uniaxially stressed along the z direction in such a way that the c'/a ratio is that of $ZnGeP_2$ and the band structure is folded into the chalcopyrite BZ. Here we are interested in showing the similarities and differences between the electronic properties of a chalcopyrite compound and its analog and the main effects of the ordering of the two cations. The method of calculation and choosing of parameters is discussed in a following section. In Figs. 37 and 38 we show the theoretical imaginary part of the dielectric function and density of states curve obtained from a full zone calculation of the band structure of $ZnGeP_2$[37] (Fig. 38b). The difference between the band structures shown in Figs. 38b and 36a is only a slight change in the pseudopotential parameters used.

Now let us compare the two band structures in Figs. 36a and 36b. First we point out that as shown in Fig. 36b the effects of tetragonal compression on the band structure are very small when compared with the effects of the antisymmetric cation potential so we will ignore them for now.

1. Structure of the Valence Band and Density of States

In the first four valence bands, the main splittings occur at the point X and the point A of the chalcopyrite Brillouin zone. In the analog, the levels L_1 and Σ_1 are almost degenerate forming a level that is almost four fold degenerate and is split into two degenerate levels by about 0.4 eV with symmetry X. The point A which was four fold degenerate in the analog is again split by 0.5 eV into two 2-fold degenerate states with symmetry A_1 and A_2.

The effect of these splittings on the first peak of the density of states curve is shown on Fig. 38a. This peak extends from $\Gamma_1(\Gamma_1)$ to $\Gamma_3(X_1)$ and shows considerably more structure than that of the analog. The first structure comes from states near the N point of the BZ and along the B direction, this direction contains doubly degenerate bands in the analog (1/2,x,1/4) and (1/2,x,3/4) that again are split by the antisymmetric cation potential. The second structure contains states mostly in the W direction (X→A) and the third broader structure comes as in the analog from states along the Λ(W→X) direction and states near $X_1(L_1)$. The width of this peak is slightly larger than that of the analog. Physically, this peak that represents s-like states around the anion is expected to be split and broadened due to the deviations from perfect tetrahedral environment around the anion but these effects are expected to be small as shown in the averaged density of states curve (dotted line in Fig. 38a). These states are deep inside the cation thus very insensitive to environment. The opposite situation occurs for the usual second s-like peak in a zincblende crystal. This peak represents s-like states near the cation and the difference between the two cations in the chalcopyrite analog is expected to deeply affect it. In Fig. 38a, we see how this peak is now split into three structures, the first two separated from the third by a small gap. The first two peaks come from bands 5 and 6 while the third comes mostly from band 7 (each peak holds approximately 2 electrons). The first two structures probably represent s-like states around the B^4 cation while the third one corresponds mainly to s-like states around the A^2 cation.

In zincblende studies of density of states, the gap between the first two s-like states has been correlated to the ionicity of the bond.[38] Since we now have two kinds of bonds, one much less ionic than that of the analog, the gap between these two structures gets reduced by as much as 1.9 eV in our calculated band structure. The first structure in this second peak starts at the point $\Gamma_2(X_3,W_1)$ and the rise and peak is caused from states in the B direction with symmetry B_2; the second structure comes from states in the Σ and Λ directions (symmetry Σ_1 and Δ_1) close to $\Gamma_1(W_1)$; for most of the band structure a gap develops between bands 6 and 7, the rise of the third peak comes from states near the point A_2 (in bands 7-8) and the peak is caused by the singular point $\Gamma_2(X_1,W_1)$. The mixing of states caused by the antisymmetric cation potential is very big for states at the Γ point in bands 5, 6 and 7, the originally doubly degenerate state $\Gamma_2(W_1) + \Gamma_1(W_1)$ splits and $\Gamma_2(W_1)$ then mixes with $\Gamma_2(X_3)$. Here we can speculate that most probably the energy separations between $\Gamma_3(X_1)$ and the two energy levels $\Gamma_2(X_3,W_1)$ can be correlated to the ionicities of the two kinds of bonds of a chalcopyrite semiconductor.

The big dip in the density of states plot after the third structure in the second s-like region is associated to a point Σ_{min} along the Σ_2 direction (band 8) near (0.3,0.3,0), corresponding to the same kind of structure and origin in the analog; this point marks the high rise of bonding orbitals in the density of states curve. The states associated with this rise are as in the analog $\Gamma_5(W_2)$ states. The broad bonding peak has much more structure than that of the analog. One new interesting feature is that it splits into two broad peaks (this effect is more noticible in the broaden out density of states curve). The dip between these peaks is associated with splittings at the point A of the chalcopyrite BZ with symmetry A_2 (bands 9-10), a gap develops along the Σ and N (x,x,2x) directions due to interactions between two Σ_1 lines and two N_1 lines.

At this point of our investigation, we can speculate that this splitting is mainly due to the two kinds of bonds $A^2 - C^5$ and $B^4 - C^5$ in the crystals under consideration. The first peak corresponding mainly to electrons concentrated in the $B^4 - C^5$ bonds while the second corresponds to electrons in the $A^2 - C^5$ bonds. A charge density plot as a function of position for the different bonds and for a few points in the BZ is expected to give the answer to these questions (work is in progress along these lines). The top of the valence band is formed by the triplet $\Gamma_5 + \Gamma_4$ originating from the Γ_{15} level of the analog. For most chalcopyrite compounds of the $A^2B^4C^5$ family, the top of the valence band has Γ_4 symmetry. The doubly degenerate level Γ_5 is separated from Γ_4 by crystal field splitting Δ_{cr} increasing with larger tetragonal compression. Shay and co-workers[39] and Shileika[40] have studied extensively the crystal field splittings for most of the $A^2B^4C_2^4$ type semiconductors. They find that a model that assumes that the value of Δ_{cr} of the ternary compound is equal to the strain induced splitting of its analog (assuming the same c'/a ratios) fits reasonably well their experimental data. There seems to be an exception to this rule, in the chalcopyrite crystal $ZnSiP_2$, the top of the valence band has symmetry Γ_5, i.e., the crystal field splitting is opposite to that of most of the other chalcopyrite crystals.[41]

Cardona, et al.[42] have been able to correlate the deformation potential $b = \Delta_{cr}/3(1 - c'/a)$ of the A^3B^5 compounds to their ionicity (b decreases with increasing ionicity). K. Dreher[43] has calculated the average ionicities of the $A^2B^4C^5$ compounds and finds that it is usually larger than those of their analogs, so a reduction of this quantity is expected due to an ionicity effect. We find that in addition the antisymmetric cation potential tends to reduce further the value of Δ_{cr} by about 0.02 eV in the case of $ZnGeP_2$.

Since the most reliable data on the structure of the conduction band and the structure of the optical gap comes from experimental reflectivity spectra (and all the modulation techniques on this spectra) let us first describe what are the dominant features of the reflectivity spectrum of $A^2B^4C^5_2$ compounds.

Due to the folding in the zb BZ into the chalcopyrite BZ, transitions between the valence and conduction band of a chalcopyrite crystal have been divided by Shay[44] into two categories:

Direct transitions--those originating from direct transitions in a zb crystal.

Pseudodirect transitions--those originating from indirect transitions in a zb crystal.

It is of course expected that the reflectivity spectrum of a chalcopyrite crystal be richer in structure than that of its zb analog; the larger number of structures in the spectrum arises from several sources:

1) Originally degenerate levels in the cubic case are split under the influence of the tetragonal compression and the antisymmetric cation potential.

2) The star of k in chalcopyrite structure does not contain all of the star of k in zb structure e.g., the Δ direction in zb splits into the Δ $(k_x,0,0)$, Λ $(0,0,k_z)$ and S $(k_x,0,2\pi/c)$ directions in chalcopyrite structure. As shown in Fig. 41a, the effects of V_A^c in the original direction are quite different along the Δ and Λ directions of the chalcopyrite BZ. The most important effects coming from the ordering of the two cations are observed near points in the band structure, where two bands coming from different k points in the zb BZ cross in the folding in process and have the same symmetry under the point group of the chalcopyrite. The bands that cross with the original Δ bands and the points of crossing in k-space are quite different in the Δ and Λ directions of the chalcopyrite band structure.

3) At this point of crossing where degenerate perturbation theory should be used in a quasi-cubic model, the mixing of states is expected to be large and as Stokowski[47] points out, the term "pseudo-direct" for transitions that become allowed due to these effects is not appropriate. We find that these mixing effects of V_A^c are the most important in splitting the reflectivity structure.

In the past few years, a fair amount of data on the optical spectra of $A^2B^4C_2^5$ compounds has appeared in the literature.[39,40,44,45] Although the optical spectra of chalcopyrites is much more complicated than those of their binary analogs, they show the same general features i.e., the spectra can be divided into three main regions: the region E_o of the first absorption edge, the region E_1 which in zb materials corresponds to transitions in the Λ direction and L point of the BZ, and the E_2 region that in zb corresponds to transitions in the Σ and Δ directions. In addition to the complexity, these reflectivity spectra will be different for light polarized parallel and perpendicular to the c-axis.

2. Optical Structure in the E_o Region.

By the properties of the first absorption edge, chalcopyrite compounds can be divided into two groups: those with a pseudo-direct gap $\Gamma_5 + \Gamma_4(\Gamma_{15}) \rightarrow \Gamma_3(X_1)$ and those with a direct gap $\Gamma_5 + \Gamma_4(\Gamma_{15}) \rightarrow \Gamma_1(\Gamma_1)$. From a quasi-cubic model, it is expected that chalcopyrite compounds with an indirect gap $\Gamma_{15} - X_1$ analog (GaP-like) be pseudo-direct gap crystals. Experimentally[40] it has been observed that $ZnSiP_2$, $ZnGeP_2$, $ZnSiP_2$ and $CdSiP_2$ have an absorption edge with pressure coefficients $dEg/dP \simeq \pm 1\times10^{-6}$ eV $kg^{-1}cm^2$, indicating that the first gap in these crystals is a pseudo-direct one $\Gamma_5 + \Gamma_4(\Gamma_{15}) \rightarrow \Gamma_3(X_1)$. Electroreflectance studies on these materials show very small structure corresponding to the first absorption edge followed by three strong peaks corresponding to the first direct transitions $\Gamma_5 + \Gamma_4(\Gamma_{15}) \rightarrow \Gamma_1(\Gamma_1)$. The weakness of the pseudo-direct transitions, indicates that the mixing of $\Gamma_3^c(X_1)$ with $\Gamma_1^c(\Gamma_1)$ and the mixing effects of the chalcopyrite potential on these levels is very small, not because this potential is small as Shileika[40] suggests, but because of the symmetry properties of the Γ_1^c and X_1^c wave functions. From charge considerations, the antisymmetric cation potential and the usual antisymmetric potential of a A^3C^5 zb semiconductor should be of the same order of magnitude. It is relatively easy to show that states coming from the Γ and X points in the zb BZ should never mix under the influence of the antisymmetric cation potential. In pseudopotential formalism this potential V_a^c can be written in the form

$$V_a^c(\vec{r}) = \sum_G S_a^c(\vec{G})\ v_a^c(|G|)\ e^{i\vec{G}\cdot\vec{r}}$$

where $v_a(|G|) = 1/2(v_A2\ (|G|) - v_B4(|G|))$. For the particular $\vec{G}$ vectors, $\vec{G} = 2\pi(\frac{n}{a}, \frac{m}{a}, \frac{\ell}{c})$, with n, m, and ℓ integers, the structure factors $S_a^c(\vec{G})$ are zero, but these are the only fourier components that can mix Γ-Γ, Γ-X, and X-X states to second order in perturbation theory. So that the only mixing that can make Γ-X transitions allowed is a Γ-W, X-W mixing but in zb materials the W energy levels are at least 2 eV from the Γ_{15}, X_1^c, Γ_1^c levels. In view of this it is not surprising that a quasi-cubic model explaining the crystal field splitting and spin-orbit splitting of the first direct gap works so well.[39]

In this discussion we have omitted the effects of the small potential introduced by the displacement of the anion from its ideal position, we will show later that structure factors introduced by this displacement are of second order in the small parameter σ for G vectors of the form $G_{zb} + (0,0,1)$ (G_{zb} are the usual G vectors for the zb analog).

3. Optical Structure in the E_1 Region

In the E_1 region, corresponding to the two spin-orbit split peaks E_1 and $E_1 + \Delta$, of the analog, chalcopyrite compounds show a much richer structure. In general, five or more peaks are observed in experimental electroreflectance,[39,40,45] modulated reflectivity[46] and reflectance[47] in the energy interval of the spectrum corresponding to the Λ transitions (E_1, $E_1 + \Delta_1$) of the analog. These peaks have been labeled $E_1(1)$, $E_1(2)$, $E_1(3)$, $E_1(4)$ and E_c by Stokowski[47] and E_1,E_2, E_3, E_4 and E_6 by Shileika.[40] We shall adopt Stokowski's notation here.

The most important features of these structures will be discussed below. The energy separating $E_1(2) - E_1(1)$ and $E_1(3) - E_1(4)$ are close to each other for the most of the $A^2B^4C^5_2$ compounds studied. This seems to indicate that these transitions come from two spin-orbit split doublets in the same region of the Brillouin Zone. The origin of this structure has been subject to extensive investigation in the past few years. Most interpretations agree in that the $E_1(1)$ and $E_1(2)$ structures originate from transitions in the N plane along the (x,x,x) direction and in terms of a quasi-cubic model equivalent to the Λ transitions in the analog. Our full zone calculations on the reflectivity of $ZnGeP_2$, show that indeed this is the case and the critical point is near the point (0.2,0.2,0.2). A comparison of the band structure of GaP and that of $ZnGeP_2$ (Fig. 41) shows that near that point the valence bands are almost unaffected by the antisymmetric cation potential while the Γ-L conduction band mixes with the W-Σ conduction bands. Notice that in the analog, these are almost degenerate near the point (0.25,0.25,0.25).

A downshift of the $E_1(1)$, $E_1(2)$ structure with respect to the E_1, $E_1 + \Delta_1$ structure in the analog has been observed for most of the chalcopyrite crystals studied so far. Since the mixing of the Λ valence bands near the critical point is small, spin-orbit interaction effects should be very close to those of the compressed analog. Under this assumption, Stokowski[47] estimates values of $E_1(2) - E_1(1) = \Delta_1$ in reasonably good agreement with experiment except for $CdSiAs_2$. Inclusion of spin-orbit interactions in $ZnGeP_2$ in our pseudopotential calculations give a value of Δ_1 = 0.08 eV in close agreement with the experimental values of 0.06 eV.

The nature of the $E_1(3)$ and $E_1(4)$ structure is subject to controversy. Kavaliauskas, et al.[45] suggest that all four peaks $E_1(1)$ to $E_1(4)$ come from transitions at the X point of the BZ in the bands 15-16→17-18 and 13-14→17-18. Under the influence of the spin-orbit interactions, the four fold degenerate level X_1, splits into two two-fold degenerate levels, $X_1 \rightarrow X_1^- + X_4^-$, $X_2^- + X_3^-$. From our studies in $ZnGeP_2$, the splitting $X_1^- + X_2^- - X_2^- + X_3^-$ is 0.02 eV; thus, it is too small to be associated to the energy separation between $E_1(1)$, $E_1(3)$ and $E_1(2)$, $E_1(4)$ as Kavaliauskas, et al. suggest. Stokowsky[47] assigns the $E_1(3)$ and $E_1(4)$ peaks to transitions at the X point of the BZ. As shown in Fig. 36, the top of the valence band at the point X contains six states which are almost degenerate, they correspond to the two doubly degenerate levels $X_1(L_3)$ ($L_3(1/2,-1/2,-1/2)$ and $L_3(-1/2,1/2,-1/2)$) and $L(\Sigma_1)$ ($\Sigma_1(1/2,1/2,0)$, $\Sigma_1(-1/2,-1/2,0)$). The fact that the L_3 and Σ_1 levels are almost degenerate is not accidental; Cohen and Bergstresser's band structures show that this is the case for all of the B^3C^5 semiconductors they study. Under these circumstances, the effects of the antisymmetric cation potential mixing the Σ_1 and L_3 levels is expected to be large as shown in Fig. 36a. This large interaction and the shifts of the L_3^v to L_1^c transitions relative to the Λ_3^v to Λ_1^ε leads Stokowski to suggest that the $E_1(3)$, $E_1(4)$ and E_c peaks come from transitions at the X points from bands 15-16, 13-14, 11-12→17-18. Although all of these transitions are allowed due to the strong L-Σ mixing in the valence band, we find that for all our band structure calculations,[48] that 15-16 → 17-18 transitions at the X point lay below the Λ $E_1(1)$, $E_1(2)$ peak. In most cases, the $X_1 \rightarrow X_1$ transitions between bands 13-14 → 17-18 lay too close to the Λ peak to explain the splitting between the $E_1(1)$, $E_1(3)$ and $E_1(2)$, $E_1(4)$ peaks.

Shay et al.[44] associate the origin of the $E_1(3)$ and $E_1(4)$ peaks to pseudo-direct transitions from the Σ line to the L-W line and to a pseudo-direct X to Γ transition. As we have seen, Γ-X mixing is too small to be observed. We find two more pieces of structure above $E_1(1)$ and $E_1(2)$. These structures which can be associated with $E_1(3)$ and $E_1(4)$ arise mainly from the strong mixing at the crossing point of the Σ and Q(W-L) lines in the conduction band along the (x,x,0) line. This mixing extends into a large region of the N plane (x,x,z) and is still very strong near the point (1/4,1/4,1/4) along the (x, x, x) line, where the mixing is between the Γ-L line and the W-Σ line. Unfortunately the peak $E_1(3)$ $N_2 \rightarrow N_1$ originates from a volume effect close to the (x, x, x) direction; because of this, a full zone calculation for the reflectivity spectra is required to compare it with experiment.

Contributions from the broad structure caused by the M_0 critical point at X (bands 13-14 → 17-18) enhance this structure in the ⊥ polarization.

Another piece of structure in the perpendicular polarization spectra, is associated to $\Sigma_2(\Sigma_2) \rightarrow \Sigma_1(\Sigma_1,Q)$ transitions. These transitions, are responsible for the $E_1(4)$ peak in $ZnGeP_2$ which for this semiconductor appears only in the perpendicular polarized spectra.[46]

A work of caution is in order here. Reference 46 is the only measurement that we know of in which the optical quality of the surface is very good and complete perpendicular and parallel polarizations were obtained. In all other electroreflectance and reflectance experiments, the parallel polarized spectra is only nominal. Even with this problem, thermoreflectance data[40] at 120°K and the modulated reflectivity experiment at 5°K agree very closly but electroreflectance data at 300°K does not (see Table IX). With the above identifications, it is clear that at least in the case of $ZnGeP_2$, the structure $E_1(3)$ and $E_1(4)$ do not come from a pair of spin-orbit split transitions. Whether this is true for all chalcopyrite semiconductors, requires more theoretical research.

For some $A^2B^4C^5_2$ semiconductors, it may happen that the strongest mixing of the (x,x,z) and the (x,x-1,z-1/2) lines is along the (x,x,x) direction, in which case a pair of spin-orbit doublets is expected in addition to the $\Sigma(\Sigma) \rightarrow \Sigma(\Sigma+Q)$ peak. From Stokowski's data[47] this seems to be the case for $ZnSiAs_2$.

We have been able to associate the E_c structure with transitions at the X point $X_1(\Sigma_2 1(3) \rightarrow X_1(L_1)$; this peak is stronger in the parallel polarization. Caution has to be taken when identifying this peak, since it is caused by an M_o singular point, the actual peak is shifted by about 0.1 eV to higher energies with respect to the energy of the transition at the singularity.

4. Optical Structure in the E_2 Region

At higher energies in the region corresponding to the E_2 peak of the reflectivity structure of zb semiconductors, at least five pieces of structure are observed in the reflectivity spectra of the $A^2B^4C^5_2$ semiconductors. At present it is premature to assign any particular transition to these peaks for all the chalcopyrite compounds. Our full zone calculations for $ZnGeP_2$ show that as one would expect, most of the contribution to the E_2 structure comes from direct and mixed transitions in the Δ and Σ directions of the analog. The Δ direction folds into the Δ, Λ and (x,0,1) directions of the chalcopyrite BZ while the Σ direction is folded into the Σ, (x,0,x) and (1-x,0,1-2x) directions. Partial summation over k-space in these directions shows that in effect the E_2 peak is mainly a Δ, Σ peak.

The width of the E_2 peak in our full zone calculation is about 0.4 eV while in experiment it is at least 0.8 eV. This probably means that we have underestimated the antisymmetric cation potential for this calculation.

The first peak in the parallel polarization around 4.76 eV comes from transitions along the Δ direction $\Delta(15\text{-}17)$ at (0.34,0,0). The line $\Delta(\Delta)$ mixes with the line $\Delta(1\text{-}k,0,1/2)$ in the valence band and then continues into bands (13,14) so transitions (13,14) → 17 near (0.5,0,0) contribute also to this peak. On the other hand, $\Lambda(0,0,k_2)$ and Σ transitions are responsible for the first peak in the perpendicular polarization at 4.77 eV. The bands involved are 12-13 → 18, and the critical point is near $\Gamma_5(X_5) \rightarrow \Gamma_3(X_1)$. The main peak in the perpendicular polarization is caused by Σ transitions near the point X of the BZ bands 16-20, indicating the strong mixing near that point in the valence bands. The small shoulder at 4.6 eV in the ⊥ polarization is caused by a singular point at (0,0,0.3) along the Λ direction (bands (13 → 17)), in this energy region we also find a critical point at (0.25,0.25,0) (14 → 17 transitions) coming from the original Σ transitions in the analog.

The main peak in parallel polarization is caused by a strong critical point inside the zone near (0.16,0.05,0.0) bands (14-17). Along the (kx,0.5,0) direction one has the δ to σ, W to σ and σ to L directions of the analog. The critical point is caused by strong mixing at the crossing point in the conduction band of the σ to L line with the δ to σ line; transitions near this point are stronger in the parallel polarization, but they also contribute to the perpendicular polarized spectra. The bands involved are 14 → 17. Near this energy region we find two additional pieces of structure caused by a critical point at (0.25,0.25,0.25) in the N plane in bands (13 → 18) and (14 → 20). The first one at 5 eV is polarized in the ∥ direction while the second one at 5.11 eV is polarized in the ⊥ polarization. The shoulder at 4.92 eV in the experiment in Ref. 46 is associated with Δ(0.5,0,0) transitions in bands 15-18; our calculated value for these transitions is 5.21 eV.

Table X shows the results of our critical point analysis and a comparison with the experiment in Ref. 46. The intensity of the E_2 peak is considerably reduced when compared with the intensity of the E_2 peak for zb crystals in our theoretical calculation, but still it is higher than the measured peak. For $ZnGeP_2$ this peak has the same intensity as the E_1 peak in the experiments of Petroff, et al. In other respects, their structure is similar to our theoretical predictions. In fact, if the entire theoretical spectra were shifted to lower energies by around 0.3 eV, the agreement between theory and experiments for almost all optical structure is very good. This is encouraging since no experimental data (except for structure constants) for $ZnGeP_2$ were used in our calculations. Theoretical and experimental reflectivity spectra are shown in Fig. 44.

Before ending this section, we add the following remarks about the identification of the reflectivity peaks. In zincblende semiconductors most of the structure in the E_1 and E_2 regions comes from transitions between the third and fourth valence bands and the fifth and sixth conduction bands, this makes the identifications very easy. On the other hand, in chalcopyrite semiconductors we have transitions from 8 valence bands to at least 4 conduction bands contributing to the reflectivity spectrum. There also exists band crossing and mixing all over the BZ and identifications are extremely difficult. Since identification of critical points that give large contributions to the electronic density of states is much more simple and physically transparent, experiments that measure this quantity are bound to be of great importance in the determination of the band structure of the chalcopyrite type semiconductors.

D. Pseudopotential Hamiltonian for Chalcopyrite Crystals and the Energy Band Structure of $ZnGeP_2$ and $ZnGeAs_2$

In this section we will discuss: 1. the psuedopotential Hamiltonian for semiconductors that crystalize in chalcopyrite structure, 2. the determination of the pseudopotential form factors and 3. the results obtained for $ZnGeP_2$ and $ZnGeAs_2$.

1. Pseudopotential Hamiltonian

The pseudopotential Hamiltonian for an electron in the crystal is:

$$\mathcal{H} = -(\hbar^2/2m)\nabla^2 + V(\vec{r}) \tag{11}$$

where $V(\vec{r})$ is the weak crystalline pseudopotential which has the symmetry of the lattice and can be expanded in the reciprocal lattice vectors $\vec{G}$.

For chalcopyrite compounds $A^2B^4C^5_2$ with 8 atoms per primitive cell, two of kind A, two of kind B and 4 of kind C, the pseudopotential $V(\vec{r})$ in Eq. (11) can be written in the form

$$\begin{aligned} V(\vec{r}) &= \frac{1}{8}\sum_{G}\left\{\sum_{i=1} e^{i\vec{G}\cdot\vec{\tau}_i^A} V_G^A + \sum_{i=1} e^{i\vec{G}\cdot\vec{\tau}_i^B} V_G^B + \sum_{i=1} e^{i\vec{G}\cdot\vec{\tau}_i^C} V_G^C\right\} e^{i\vec{G}\cdot\vec{r}} \\ &= \sum_{G} V(\vec{G})\, e^{i\vec{G}\cdot\vec{r}} \end{aligned} \tag{12}$$

where

$$\left.\begin{aligned} &\vec{\tau}_1^A = (0,0,0)\ ,\ \vec{\tau}_2^A = (0,a/2,c/4) \\ &\vec{\tau}_1^B = (0,0,c/2)\ ,\ \vec{\tau}_2^B = (0,a/2,3c/4) \\ &\vec{\tau}_1^C = (au,a/4,c/8)\ ,\ \vec{\tau}_2^C = (a\bar{u},3a/4,c/8)\ ,\ \vec{\tau}_3^C = (3a/4,au,7c/8)\ , \\ &\vec{\tau}_4^C = (a/4,a\bar{u},7c/8) \end{aligned}\right\} \tag{13}$$

and V_G^A, V_G^B and V_G^C are related to the spherically symmetric atomic pseudopotentials by:

$$V_G^{A,B\text{ or }C} = 8/\Omega \int V^{A,B\text{ or }C}(\vec{r})\, e^{-i\vec{G}\cdot\vec{r}}\, d^3r \tag{14}$$

Ω is the volume of the primitive cell, $\Omega = a^2c/2$.

Let's define the average cation potential $V_1(G)$ by

$$V_1(G) = (V_G^A + V_G^B)/2 \quad , \tag{15}$$

the antisymmetric cation potential by

$$V_A^C(G) = (V_G^A - V_G^B)/2 \tag{16}$$

and let us write

$$V_2(G) = V_G^C \tag{17}$$

Further, let us separate the Hamiltonian into two parts, one assuming that the anion is in its ideal position, the other taking care of the pseudopotential that this displacement produces. With this, $V(\vec{G})$ in Eq. (12) can be written in the form

$$\begin{aligned} V(\vec{G}) = S_s(\vec{G})\ (V_1(G) + V_2(G))/2 + S_A(\vec{G})\ (V_1(G) - V_2(G))/2 \\ + S_A^C(\vec{G})\ V_A^C(G) + S_u(\vec{G})\ V_2(G)\ \ldots \end{aligned} \tag{18}$$

The symmetric structure factor $S_s(\vec{G})$ in Eq. (18) can be written in the form

$$\begin{aligned} S_s(\vec{G}) &= \frac{e^{i\vec{G}\cdot\vec{\eta}}}{4} \cos(\eta\cdot G) \left(e^{i\vec{G}\cdot\vec{\tau}_1^A} + e^{i\vec{G}\cdot\vec{\tau}_2^A} + e^{i\vec{G}\cdot\vec{\tau}_1^B} + e^{i\vec{G}\cdot\vec{\tau}_2^B} \right) \\ &= e^{i\vec{G}\cdot\vec{\eta}} \cos(\vec{\eta}\cdot\vec{G}) \quad \text{for } \vec{G} = \vec{G}_{zb} \\ &= 0 \qquad \text{otherwise} \end{aligned} \tag{19}$$

$\vec{\eta} = (a/8, a/8, c/16)$ and $\vec{G}_{zb}$ are the set of $\vec{G}$'s that contain only $\vec{G}$ vectors of the zincblende crystal structure (compressed along the z-axis).

Similarly the antisymmetric structure factor $S_A(\vec{G})$ is

$$\begin{aligned} S_A(\vec{G}) &= e^{i\vec{G}\cdot\vec{\eta}}\ i \sin \vec{G}\cdot\vec{\eta} \quad \text{for} \quad \vec{G} = \vec{G}_{zb} \\ &= 0 \qquad\qquad\qquad\qquad \text{otherwise} \end{aligned} \tag{20}$$

The antisymmetric cation structure factor $S_A^C(\vec{G})$ can be written in the form

$$S_A^C(\vec{G}) = \frac{i}{2}\, e^{i\vec{G}\cdot\vec{\tau_2^B}/2} \sin(\vec{G}\cdot\vec{\tau_1^B}/2) \cos(\vec{G}\cdot\vec{\tau_2^A}/2) \tag{21}$$

in this form, it is easy to show that $S_A^C(\vec{G}) = 0$ for $\vec{G}$'s of the form $\vec{G} = \vec{G}_{zb}$ or $\vec{G} = \vec{G}_{zb} + (0,0,1)$.

The anion distortion structure factor $S_u(\vec{G})$ is

$$\begin{aligned} S_u(\vec{G}) = e^{i2\vec{\eta}\cdot\vec{G}} \Bigg\{ & \left(e^{i\vec{\varepsilon}_1\cdot\vec{G}} - 1\right) + e^{i\vec{\beta}\cdot\vec{G}} \left(e^{-i\vec{\varepsilon}_1\cdot\vec{G}} - 1\right) + \\ & e^{i\vec{\gamma}\cdot\vec{G}} \left[\left(e^{i\vec{\varepsilon}_2\cdot\vec{G}} - 1\right) + e^{i\underline{\beta}\cdot\underline{G}} \left(e^{-i\vec{\varepsilon}_2\cdot\vec{G}} - 1\right)\right] \Bigg\} \end{aligned} \tag{22}$$

where $\vec{\varepsilon}_1 = (\sigma/4,0,0)$, $\vec{\varepsilon}_2 = (0,\sigma/4,0)$ and $\underline{\beta}$ and $\underline{\gamma}$ are zincblende lattice vectors of the form $\vec{\beta} = (-a/2,a/2,0)$, $\vec{\gamma} = (a/2,0,3c/4)$. Then for $\vec{G} = \vec{G}_{zb}$:

$$S_u(\vec{G}) = \frac{e^{i2\vec{\eta}\cdot\vec{G}}}{4} (\cos\vec{\varepsilon}_1\cdot\vec{G} + \cos\vec{\varepsilon}_2\cdot\vec{G} - 2) \tag{23}$$

For $\vec{G} = \vec{G}_{zb} + (0,0,1)$

$$S_u(\vec{G}) = \frac{e^{i2\vec{\eta}\cdot\vec{G}}}{4}\ i(\cos\vec{\varepsilon}_1\cdot\vec{G} - \cos\vec{\varepsilon}_2\cdot\vec{G}) \tag{24}$$

For $\vec{G} = \vec{G}_{zb} + (1,0,1/2)$

$$S_u(\vec{G}) = \frac{e^{i2\vec{\eta}\cdot\vec{G}}}{4}\ i(\sin\vec{\varepsilon}_1\cdot\vec{G} - \sin\vec{\varepsilon}_2\cdot\vec{G}) \tag{25}$$

Exchanging cations A and B has the effect of changing u → -u. From the above equations $S_u(G) = S_{-u}(G)$ for $G = G_{zb}$ or $G = G_{zb} + (0,0,1)$ but $S_u(G) = -S_{-u}(G)$ for $G = G_{zb} + (1,0,1/2)$. Typically the nonzero structure factors $S_s(G)$ and $S_A(G)$ are of the order of 1, the nonzero antisymmetric cation structure factors that under the quasicubic model only mix k states with k + (1,0,1/2) states are typically of the order of 1/4. $S_u(G) \sim 0.02$ for $G = G_{zb}$ or $G = G_{zb} + (0,0,1)$ (and this is the reason why the Γ-X pseudodirect transitions are so weak in all the $A^2B^4C^5_2$ compounds studied so far) while $S_u(G) \lesssim 0.1$ for $G = G_{zb} + (1,0,1/2)$ in the region where the pseudopotential form factors are appreciable. Usually this happens for $|G| < 4\ (2\pi/a)$. In view of the values of the structure factors in Eq. 18, it is clear that the leading term is the cubic one given by

$$V_{cubic}(\vec{G}) = S_s(\vec{G})\ (V_1(G) + V_2(G))/2 + S_A(\vec{G})\ (V_1(G) - V_2(G))/2 \tag{26}$$

the antisymmetric cation potential

$$V^C_A(\vec{G}) = S^C_A(\vec{G})\ V^C_A(G) \tag{27}$$

perturbs the cubic band structure mostly at points where k and k + (1,0,1/2) states are degenerate or nearly degenerate, and the distortion potential

$$V_u(\vec{G}) = S_u(\vec{G})\ V_2(G) \tag{28}$$

which depends only on the anion potential can be considered as only a small perturbation on the band structure obtained with Eqs. (26) and (27). The fact that Eq. (28) depends only on the anion potential seems to indicate that it is the effect of this small perturbation what causes the flip over of the ordering of the Γ_4 and Γ_5 levels at the top of the valence band in $ZnSiP_2$ with respect to the ordering of those levels in $ZnSiAs_2$.

In the region $|G| < 4(2\pi/a)$ where the pseudopotential form factors. are assumed to be different from zero, there are 30 different G vectors, With 3 different atoms in the primitive cell, one needs 90 form factors to fix the crystalline pseudopotential, Fortunately, this number can be greatly reduced by using the symmetric part of the potential $V_S(G)$ the antisymmetric part of the potential $V_A(G)$, the antisymmetric cation pseudopotential $V_A^C(G)$ as in Eq. (18). With this, a total of 39 parameters are needed for the calculation.

The basis states used to solve the Hamiltonian matrix are plane waves of wave vector $\vec{k} + \vec{G}$, ($\vec{G}$ reciprocal lattice vectors and $\vec{k}$ inside the first Brillouin zone). The number of plane waves is bounded by the relationship $(\vec{G} + \vec{k})^2 \leq E_1$ and Löwdin[3] perturbation scheme is used for plane waves such that $E_1 < (\vec{k} + \vec{G})^2 < E_2$.

For the band structure shown in Fig. 38, for $ZnGeP_2$, E1 = 7.1 and E2 = 18.1 and convergence is better than 0.1 eV. For the band structure shown in Figs. 41 and 45, E1 = 5.1 and E2 = 18.1 and convergence is about 0.1 eV for the top valence bands and bottom conduction bands but about 0.2 eV for the bottom valence bands corresponding to more localized states. Since we do not have any experimental information on these valence bands, we believe that a high accurate but costly calculation is not justified at the present time.

2. Determination of the Form Factors

Basic to the pseudopotential theory, is the concept of transferability[3] of atomic pseudopotentrals, i.e., it is assumed that the atomic pseudopotential in real space for the elements is independent of crystal structure and composition. Of course, this assumption is not an exact one, small screening effects which are included in the empirically determined form factors are expected to change with environment. In determining the form factors for chalcopyrite compounds from the known form factors of zincblende semiconductors, these screening effects can be taken into account by noting for example that the surroundings of a P atom in $ZnGeP_2$ are on the average those of GaP while in $CdSnP_2$ are those of InP. Then in extracting the P atomic pseudopotential for $ZnGeP_2$ from GaP and for $CdSnP_2$ from InP one is accounting correctly for screening effects on the average. In addition, since the volume per atom of a chalcopyrite semiconductor is very close to the volume per atom in its zincblende analog, problems of scaling are minimized for the $\underline{G}$ vectors with largest structure factors i.e., $\vec{G} = \vec{G}_{zb}$. In determining the form factors of $ZnGeP_2$ we followed two different paths; in the first calculation (band structure in Fig. 43) we assumed that on the average $ZnGeP_2$ is GaP, then we used

$$\begin{aligned} (V_1 + V_2)/2 &= V_S^{GaP} \\ (V_1 - V_2)/2 &= V_A^{GaP} \end{aligned} \qquad (29)$$

Assuming these two relations and from the known form factors of Ge[4] we get

$$V_A^C = V_{Ga} - V_{Ge} = V_S^{GaP} + V_A^{GaP} - V_{Ge} \qquad (30)$$

The form factors for GaP used are those of Ref. 7. The pseudopotential curves of GaP and Ge were free hand extrapolated and it is assumed that all pseudopotentials are zero for $G \geqslant (4,0,0)\ 2\pi/a$ and that the antisymmetric GaP pseudopotential is zero for $G \geqslant (2/a, 2/a, 2/c')\ 2\pi$, and that the symmetric GaP and Ge pseudopotentials at $G = 0$ are $-2/3\ E_F$ while the antisymmetric GaP pseudopotential is zero at zero wave vector. The zinc pseudopotential curve extracted in this way follows a rather strange curve which turns upwards from $(G)^2 = 4$ to $(G)^2 = 3$ (in units of $(2\pi/a)^2$). This phenomenon, which is also observed by Cohen and Heine[3] for the Zn pseudopotential curves extracted from the pseudopotential form factors of ZnS and ZnSe was not completely understood, although it probably arises from non-local effects. We therefore smoothed out the Zn pseudopotential curve. This in great part accounts for the discrepancies of the theoretical reflectivity spectra calculated with this potentials and the experiment. Our results with these pseudopotential form factors for the imaginary part of the dielectric function $\epsilon_2(\omega)$, the reflectivity $R(\omega)$ and density of states curve $D(\omega)$ are shown in Figs. 37, 39 and 38 respectively and are discussed above.

For the band structure of Fig. 36, the pseudopotential of Zn was extracted from ZnS, the one for P from GaP. All ZnS, GaP and Ge form factors are those of Cohen and Bergstresser[4]

We take

$$V_{chal}(G) = \frac{8\Omega_{zb}}{\Omega_{chal}} V_{zb}(G) \tag{31}$$

in agreement with the assumption that the real space atomic pseudopotential is independent of crystal structure and composition.

For the scaling of the form factors we assume that the antisymmetric form factors of ZnS and GaP are monotonic decreasing functions of wave vector of the form $V_S(G) = A/G\alpha + B$ for $G^2 \geqslant 3(2\pi/a)^2$. For the symmetric form factors we get the slopes of the pseudopotential curves by assuming that a homopolar diamond crystal with a symmetric pseudopotential equal to that of GaP has the same hydrostatic pressure coefficients as Ge. We expect this since the GaP and ZnS symmetric C-B form factors are the average of the Si and Ge form factors and it is expected that the homopolar contribution to hydrostatic pressure coefficients in GaP and ZnS be close to the pressure coefficients of Si and Ge. With the values of the pseudopotentials and its slopes at $G = G_{zb}$ we fitted a smooth polinomial curve such that $V_S(0) = -2/3\ E_F$ and $V_S(G^2 = 16) = 0$.

Because of the extraneous behavior of the Zn pseudopotential curve for low G's, it is very hard to estimate V_A^C for $\vec{G} = (1/a, 0, 1/c)\ 2\pi$, the only important parameter for $G^2 < 3(2\pi/a)^2$, and this, we estimated by using the known splitting between the Λ peak (E_1 and E_2) and the E_c peak in $ZnGeP_2$.

For the band structure of $ZnGeAs_2$ shown in Fig. 45, the pseudopotential of Zn was extracted from ZnSe, the one for As from GaAs, C-B form factors; the extrapolating proceedure is the same as in the case of

$ZnGeP_2$. $V_A^C(\vec{G} = (1/a,0,1/c)2\pi)$ was again fitted to give the splitting of the E_1, E_2 pair with E_c; the data used was that of Shileika.[40] For the band structures of compressed GaAs and GaP (Figs. 40b and 36b), the same extrapolating proceedure was used. In setting up the Hamiltonian matrix it is assumed that the crystal structure is chalcopyrite with two equal cations and an ideal u (u = 0.25). The compression is given by assuming the c/a ratio equal to that of the chalcopyrite analog. The lattice constant is choosen so that the volume of the compressed crystal is the same as the volume of the uncompressed crystal to avoid hydrostatic pressure components.

The zincblende component of the crystalline potential for $ZnGeP_2$ is equal to the crystalline potential of GaP due to the fact that C-B symmetric form factors of GaP and ZnSe are equal while the C-B antisymmetric form factors of GaP are exactly 1/2 the C-B antisymmetric form factors of ZnS. The same assertion is not true for $ZnGeAs_2$ and its analog GaAs; in this case the C-B antisymmetric form factors of GaAs are not 1/2 the C-B antisymmetric form factors of ZnSe. Then all the differences in band structure between GaP and $ZnGeP_2$ can be attributed to the chalcopyrite component of the potential while the differences between the band structure of GaAs and $ZnGeAs_2$ include also the effects of a different zincblende component of the potential. The band structures (Figs. 36 and 40) were calculated along the $\Lambda(0,0,k_z)$, $\Sigma(k_x,k_x,0)$, $N(k_x,k_x,k_x)$, $\Delta(k_x,0,0)$ and $W(1/2,1/2,k_z)$ directions (the k_x component in units of $2\pi/a$, k_z component in units of $2\pi/c'$ with $c' = c/2$, as through all this work).

The band structures of $ZnGeP_2$ and $ZnGeAs_2$ should be considered only approximate, not only because of the low value of E_1 used for this calculation, but and most important because the form factors that enter into the chalcopyrite potential come only from extrapolated values.

Let us discuss our results for $ZnGeAs_2$ and $ZnGeP_2$ (Figs. 36 and 40) in more detail:

$ZnGeAs_2$

$ZnGeAs_2$ is a direct gap semiconductor. Shileika[40] reports three electroreflectance peaks in the region of the absorption edge at 1.15 eV, 1.19 eV, 1.48 eV (at room temperature). Removing the spin-orbit splitting, with the help of the quasicubic model,[39] these peaks correspond to a Γ_5-Γ_1 transition at 1.29 eV and a Γ_4-Γ_1 transition at 1.23 eV our calculated values are $\Gamma_5-\Gamma_1 = 1.4$ eV and $\Gamma_4-\Gamma_1 = 1.35$ in fair agreement with experiment. Our calculated value for the crystal field splitting Δ_{cr} is $\Delta_{cr} = 0.05$ eV while in experiment is 0.06 eV. The experimental spin-orbit splitting is 0.31 eV and very close to the value of this parameter in the analog.

Using our identifications of the E_1 structure in $ZnGeP_2$ as a guide, we predict an $E_1(1)$, $E_1(2)$ doublet for $ZnGeAs_2$ at 2.37 eV; the mean energy of this peak in experiment is at 2.34 eV. Shileika's experiment shows only one peak in the $E_1(3)$, $E_1(4)$ region at 2.72 eV; the energy of the transitions from the $\Sigma(\Sigma)$ valence band to the point of crossing of the $\Sigma(\Sigma,Q)$ conduction bands is 2.77 eV in our calculated band structure. Our calculated interband energies of the X point of the BZ are $X(15,16\rightarrow17,18) = 1.90$ eV, $X(13,14\rightarrow17,18) = 2.37$ eV, $X(11,12\rightarrow17,18) = 3.19$ eV, this last transition in close agreement with the experimental value of 3.23 eV for the E_3 peak in Shileika's data. Kwan and Woolley's[49] unpolarized data is in close agreement with Shileika's data in the E_1 region, and shows three structures in the E_2 region at 3.8 eV, 4.37 eV and 4.92 eV. The main peak occurs at 4.37 eV and probably corresponds to Σ, Λ and Δ direct transitions near the $\Gamma(X)$ point of the BZ. Our calculated value for this interband energy is 3.7 eV; the lack of agreement between theory and experiment for these transitions can be traced back to Cohen and Bergstresser's results that give values for the X_5-X_1 transitions that are consistently about 0.5 eV smaller than experiment for the Ge, GaAs ZnSe series. Guided from our experience on $ZnGeP_2$ we expect that $X(\sigma,L) \rightarrow X(\sigma)$ transitions (bands (15,16→19,20)) also contribute strongly to the main E_2 peak in the perpendicular polarized spectra; our interband energies for these transitions are 3.85 eV. Based on our identifications in $ZnGeP_2$, we conclude that the small shoulder in Kwan's data at 3.8 eV is caused by Λ and Δ transitions around the points (0,0,0.34) and (0.34,0,0), our interband energies at these points are 3.55 eV and 3.5 eV respectively.

Let us now discuss the structure of the valence bands. The first four valence bands corresponding to s-like states around the As are almost unaffected by the chalcopyrite potential, the main splittings occur along the W direction (X to A), at the point A of the BZ the splitting is 0.88 eV. On the other hand bands 5, 6 and 7 that in the analog give most of the contribution to the s-like (around the cation) peak of the density of states curve, are completely distorted by the chalcopyrite potential. Bands 5 and 6 correspond to s-like states around the Ge atom with some transfer of charge to the Zn atom in band 6. A gap develops between bands 6 and 7 in a large region of the BZ and band 7 corresponds to s-like states around the Zn atom. The most striking feature of the band structure shown in Fig. 40 is that the second $\Gamma_2(X_3,W_1)$ s-like level is almost degenerate with $\Gamma_5(W_2)$ level so that what we conjecture to be s-like states around the Zn will be very hybridized with the p-like bands. The same is not true for our calculated band structure of $ZnGeP_2$. A result in this direction is somewhat expected if one notices that $ZnGeAs_2$ is a more covalent crystal than $ZnGeP_2$. Of course, whether the effect of the chalcopyrite potential is as large as we predict or not will come when X-ray photoemission spectra or ultraviolet photoemission spectra for $ZnGeAs_2$ become available.

$ZnGeP_2$

$ZnGeP_2$ is a pseudodirect gap semiconductor; Shay et al.[41] report two small electroreflectance peaks at 2.05 and 2.11 eV corresponding to the spin-orbit pseudodirect transitions Γ_5-Γ_3 in close agreement with Shileika's wavelength modulation absorption spectrum for this semiconductor at room temperature. Removing the 0.08 eV spin-orbit contributions, the experimental values correspond to a Γ_5-Γ_3 transition at 2.08 eV and a Γ_1-Γ_3 transition at 2 eV; our calculated values for these transitions are Γ_5-Γ_3 = 2.09 eV, Γ_4-Γ_3 = 2.04 eV. The first direct transitions Γ_4-Γ_1 are at 2.47 eV and the Γ_5-Γ_1 transitions are of 2.55 eV (Δ_{S-O} removed from Shileika's data at 120°K), our calculated values for these transitions are Γ_5-Γ_1 = 2.28 and Γ_4-Γ_1 = 2.23 in fair agreement with experiment.

The downshift of the first direct gap when compared with that of the antisymmetric cation potential that produces a small mixing of Γ states with W states at the top of the valence band and bottom of the conduction band. On the other hand, pseudodirect Γ-X dipole matrix elements are about 100 times smaller than Γ-Γ dipole matrix elements indicating the smallness of the Γ-X mixing. N(Λ) transitions near (0.2,0.3,0.2) (bands 15,16→18) calculated at 2.93 and 2.98 eV corresponding to the $E_1(1)$ and $E_1(2)$ peaks of Petroff's [46] data at 3.02 and 3.08 eV. The calculated energy of $\Sigma(\Sigma,Q)$ transitions near the point of crossing in the conduction band is 3.46 eV in good agreement with the experimental[46] value of 3.41 eV for the $E_1(4)$ peak. At the X point interband energies corresponding to X(L,σ) - X(L) transitions are: 2.58 eV (15,16→17,18) 3.03 eV (13,14→17,18) and 3.54 eV (11,12→17,18). These last transitions corresponding to the experimental[46] $E_{c'}$ peak at 3.74 eV. As we pointed out before in this work, we extimate that the actual position of the E_c peak in our calculated band structure is shifted at least 0.1 eV towards higher energies from the M_o singularity at the X point, improving the agreement with experiment.

At higher energies the $\Delta(\Delta)$, $(k_x,0,0)$ transitions are split; for $k_x > 0.5$ bands 14-17 contribute mostly to the $\perp$ polarization while bands 13-17 contribute mostly to the $\parallel$ polarization we find a critical point near (0.5, 0,0) in bands 14-17 with a 4.19 interband energy and a critical point near (0.6,0,0) in bands 13-17 with 4.32 eV interband energy. We associate these transitions with the first two peaks in the experimental E_2 region of the spectrum at 4.17 eV and 4.3 eV; the agreement here is excellent but of course only a full zone calculation with the present form factors can prove that our identification is correct. $\Lambda(\Delta)$ 13-17 transitions near (0,0,0.3) which we associated with the first structure in the E_2 region of the perpendicular polarized spectrum in our earlier calculation are now at about 4.15 eV. Our calculated energy for the $\Gamma_5(X_5) - \Gamma_3(X_1)$ transitions is 4.57 eV in close agreement with the 4.46 eV value for the $E_2^{\perp}(2)$ experimental peak. The main peak in the perpendicular polarization labeled $E_2^{\perp}(3)$ at 4.79 eV in the experimental spectrum is associated with $X(\sigma,L) \rightarrow X(\sigma)$ transitions, our calculated value is 4.69 eV.

Using our earlier full zone calculation as a guide, (see Table 10) we predict that the main peak in the E_2 region $E_2^{\parallel}(3)$ at 4.68 eV the experimental value for this peak is 4.73 eV.

Our new value for the $\Delta(0.5,0,0)$ transitions in bands 15-18 is 4.8 eV in fair agreement with our earlier identification that corresponds to the experimental shoulder at 4.92 eV.

ACKNOWLEDGEMENTS

I am deeply grateful to my thesis adviser, Professor Marvin Cohen. His kindness, patience and encouragement are in great part responsible for the completion of this work.

I express my thanks to the faculty members of the Department of Physics, in particular to Professors Yves Petroff and Ron-Yen Shen for helpful discussions during various phases of my research.

It is a great pleasure to thank all the graduate students and post-doctoral physicists in the Solid State Group, with whom I discussed innumerable questions in the course of this work. Among this I especially thank Dr. John Walter, John Joannopoulos, J. D. Chadi and Jim Chelikowsky.

I appreciate the help of Jean Wolslegel in preparing this manuscript. The financial support of the Consejo Nacional de Ciencia y Tecnologia, the National Science Foundation and the computer support given by the Inorganic Materials Research Division, of the Lawrence Berkeley Laboratory is gratefully acknowledged.

On the non-professional level, the constant encouragement of my parents and husband has made this work possible.

This work was done under the auspices of the U. S. Atomic Energy Commission.

APPENDIX
CALCULATIONS OF CHARGE DENSITIES AND WANNIER FUNCTIONS FROM A REPRESENTATIVE $\vec{k}$ POINT IN THE BRILLOUIN ZONE

In this section we will discuss briefly the method of obtaining a representative $\vec{k}$ point in the BZ that gives an approximate total charge density for crystals with a fcc lattice.[33] We also construct a set of approximate Wannier functions using the same representative $\vec{k}$ point.

The Block functions of the system (which are determined up to a phase factor) are given in terms of the Wannier functions by

$$e^{i\theta(\vec{k})}\,\psi_{\vec{k},n}(\vec{r}) = \frac{1}{\sqrt{N}}\sum_{\vec{\ell}}\sum_{\mu=1}^{\nu} e^{i\vec{k}\cdot\vec{\ell}}\,a_{\mu}(\vec{r}-\vec{\ell})\,U_{n,\mu}(\vec{k}) \qquad (A.1)$$

where $\theta(\vec{k})$ is any real function of $\vec{k}$, n is the band index and $\vec{\ell}$ are the lattice vectors of the crystal. The band index for a given k is usually defined in terms of increasing energy i.e., $E_{\vec{k},n} < E_{\vec{k},n+1}$ and $U_{n,\mu}(\vec{k})$ is a unitary matrix for each $\vec{k}$. If $U_{\mu,n}(\vec{k}) \neq \delta_{\mu n}$ for every $\vec{k}$ it is said that the Wannier functions $a_{\mu}(\vec{r})$ are Composite Wanier functions of the ν valence bands in the band structure of the crystal.

From Eq. (A.1) it is easy to show that

$$a_{\mu}(\vec{r}-\vec{\ell}) = \frac{1}{\sqrt{N}}\sum_{\vec{k}}\sum_{\mu=1}^{\nu} e^{-i\vec{k}\cdot\vec{\ell}}\,e^{i\theta(\vec{k})}\,\psi_{\vec{k},n}(\vec{r})\,U^{\dagger}_{n,\mu}(\vec{k}) \;\ldots \qquad (A.2)$$

and that the total charge density in the ν valence bands is

$$\rho(\vec{r}) = \sum_{\mu=1}^{\nu}\rho_{n}(\vec{r}) = \sum_{\mu=1}^{\nu}\sum_{\vec{k}}|\psi_{\vec{k},n}(\vec{r})|^{2} = \sum_{\mu=1}^{\nu}\sum_{\vec{\ell}}|a_{\mu}(\vec{r}-\vec{\ell})|^{2} = \sum_{\mu=1}^{\nu}\rho_{\mu}(\vec{r}) \;\ldots \qquad (A.3)$$

Let T be all the transformations of the point group of the crystal, the sum over the valence bands charge density for a given $\vec{k}$ is given by:

$$\sum_n \sum_T \rho_{T\vec{k},n}(\vec{r}) = \frac{1}{N} \sum_T \sum_{\vec{\ell}} \sum_\mu |a_\mu(\vec{r}-\vec{\ell})|^2 +$$

$$\frac{1}{N} \sum_{\vec{\ell}'\neq 0} e^{i\vec{k}\cdot\vec{\ell}'} \sum_{\vec{\ell}} \sum_T \sum_\mu a_\mu(\vec{r}-\vec{\ell})\, a^*_\mu(\vec{r}-T\vec{\ell}'-\vec{\ell})$$

$$= \frac{1}{N} \sum_T \sum_\mu \rho_\mu(\vec{r}) + \frac{1}{N} \sum_{\vec{\ell}'}{}' e^{i\vec{k}\cdot\vec{\ell}'} \sum_\mu F_\mu(\vec{r},\vec{\ell}') \quad \ldots. \qquad (A.4)$$

with

$$F_\mu(\vec{r},\vec{\ell}') = \sum_T \sum_{\vec{\ell}} a_\mu(\vec{r}-\vec{\ell})\, a^*_\mu(\vec{r}-T\vec{\ell}'-\vec{\ell}) \quad \ldots. \qquad (A.5)$$

for $U_{n,\mu} = \delta_{n,\mu}$ for every $\vec{k}$, Eq. (A.4) can be decoupled into four equations, one for each band (see Ref. 51).

If one can minimize the last term on the left-hand side of Eq. (A.4) for some $\vec{k}$, the total change density in the valence band can be approximated by the term on the left-hand side of Eq. (A.4) (except for normalization factors). To do this, Chadi and Cohen[51] separate the sum over $\vec{\ell}'$ into two parts: one containing all $T\vec{\ell}'$ for a given $\vec{\ell}'$, the other containing different sets of $\vec{\ell}'$'s not related by a transformation in the point group of the crystal; $F_\mu(\vec{r},\vec{\ell}')$ is independent of the particular $\vec{\ell}'$ in the set $T\vec{\ell}'$. Let $\vec{\ell} = \vec{\ell}_{p,g}$ such that $T(\vec{\ell}_{p,g}) = \vec{\ell}_{p,g'}$, then

$$\sum_{\vec{\ell}\neq 0} e^{i\vec{k}\cdot\vec{\ell}} F_\mu(\vec{r},\vec{\ell}) = \sum_p \left(\sum_g e^{i\vec{k}\cdot\vec{\ell}_{p,g}} \right) F_\mu(\vec{r},p) \qquad (A.6)$$

If the Wannier functions are well localized, $F_\mu(\vec{r},p)$ is small for large $|\vec{\ell}_{p,g}|$; for small $|\vec{\ell}_{p,g}|$, $\sum_g e^{i\vec{k}\cdot\vec{\ell}_{pg}}$ may be minimized choosing an appropriate $\vec{k}$. The $\vec{k}$ point proposed by Baldareschi is such that this sum is zero for the first two nearest neighbors in fcc structure.

Its coordinates are $\vec{k}_o = \frac{2\pi}{a}(0.622,\ 0.295,\ 0)$.

The error involved in this calculation of charge density depends on the localization of $a_n(\vec{r})$ for the sum over the valence bands charge density, while for individual bands it depends on the localization of $a_n(\vec{r})$. Since it is possible to construct composite Wannier functions $a_\mu(\vec{r})$ which are more localized than individual band Wannier functions,[34] it is to be expected that the approximation is better for the sum over the valence band charge density than for individual bands. We estimate an error of ±3% for the total charge density of Si, comparing our results using the Baldareschi scheme and those of Walter and Cohen[2] at a few points in $\vec{r}$ space.

We can construct a set of approximate Wannier functions $a_{n,o}$ (in the sense that give the same charge density as the Baldereschi point) assuming that

$$\psi_{\vec{k},n}(\vec{r}) = \frac{e^{i\vec{k}\cdot\vec{r}}}{\sqrt{N}}\, u_{T\vec{k}_{o},n}(\vec{r})\; e^{i\theta_n(\vec{k})} \quad \ldots \tag{A.7}$$

for $\vec{k}$ and $T\vec{k}_o$ in the same irreducible part of the BZ. $u_{T\vec{k}_o}$ is the periodic part of $\psi_{T\vec{k}_o}$. Let I be the irreducible part of the BZ such that $\vec{k}_o \varepsilon I$, then:

$$a_{\mu,o}(\vec{r}) = \frac{1}{\sqrt{N}}\,\frac{\Omega_{cell}}{(2\pi)^3}\sum_T\sum_n\left[\int_{TI} e^{i\vec{k}\cdot\vec{r}}\, U^+_{n,\mu}(\vec{k})\, e^{i\theta_n(\vec{k})}\, d^3\vec{k}\right] u_{T\vec{k}_{o},n}(\vec{r}) \quad \ldots \tag{A.8}$$

It is easy to show that the set of functions $a_{n,o}(\vec{r} - \vec{\ell})$ are orthogonal, have the proper normalization and that

$$\sum_T\sum_\mu\sum_{\vec{\ell}} |a_{\mu,o}(\vec{r}-\vec{\ell})|^2 = N\sum_T\sum_n |u_{T\vec{k}_{o},n}|^2 \quad \ldots \tag{A.9}$$

In Figs. 41, 42, 43 and 44 we show the approximate Wannier functions for Si along the (1,1,1) direction. These wave functions were constructed with $U_{m,n} = \delta_{m,n}$ for every $\vec{k}$ and for simplicity $e^{i\theta_n(\vec{k})} = \pm 1$ the choice of sign depends on the band index and on T and gives real symmetric Wannier functions around the origin at the bonding site.

In Fig. 45, we show the plot of a composite Wannier function along the (1,1,1) direction. We have assumed that $\theta_n(\vec{k})$ and $U_{n,\mu}(\vec{k})$ are only functions of n and T: again, $e^{i\theta_n(\vec{k})} = \pm 1$ depending on n and T.

Along the (1,1,1) direction, the only transformations on $\vec{k}$ involved in the calculation are of the form R and IR where $R = (S_4)^n$ (n=0,1,2,3) and I is the inversion operator. For real Wannier functions, $e^{i\theta_n(\vec{k})} = e^{i\theta_n(\vec{Ik})}$ and $U_{n,\mu}(\vec{k}) = U_{n,\mu}(\vec{Ik})$. The Wannier function shown in Fig. 37, $a^C_{1,o}(\vec{r})$, is constructed with $U_{n,1}(R^{m+1}) = \pm\delta_{n,m}$. Comparing Fig. 45 with Figs. 41, 42, 43 and 44, we see that even for this simple choice of $U_{n,m}$, the composite Wannier function is more localized than the individual band Wannier functions.

REFERENCES

1. J. C. Phillips, Phys. Rev. Letters 20, 550 (1968).

   J. C. Phillips, Rev. Mod. Physics 42, 317 (1970).
2. J. P. Walter and M. L. Cohen, Phys. Rev. B4, 1877 (1971).
3. M. L. Cohen and V. Heine, Solid State Physics 24, 37 (1970).
4. M. L. Cohen and T. K. Bergstresser, Phys. Rev. 141, 789 (1966).
5. A. E. O. Animalu and V. Heine, Phil. Mag. 12, 1249 (1965).
6. J. P. Walter and M. L. Cohen, Phys. Rev. B1, 2661 (1970).
7. J. P. Walter and M. L. Cohen, Phys. Rev. 183, 763 (1969).
8. G. Weisz, Phys. Rev. 149, 504 (1966).
9. S. Bloom and T. K. Bergstresser, Solid State Comm. 6, 465 (1968).
10. J. P. Walter, M. L. Cohen, Y. Petroff and M. Balkanski, Phys. Rev. B1, 2661 (1970).
11. F. Herman and Skillman, Atomic Structure Calculations (Prentice-Hall, Inc., Englewood Cliffs, N. J., 1963).
12. C. W. Higginbotham, F. H. Pollak and M. Cardona in Proceedings of the Ninth International Conference on the Physics of Semiconductors, Moscow (Nauka, Leningrad, 1968), p. 57.

    F. Herman, R. L. Kortum, C. D. Kuglin and J. P. Van Dyke, Methods in Computational Physics, B. Adler, S. Fernabach and M. Rotenbert, eds. (Academic Press, Inc., N. Y., 1968), p. .
13. F. H. Pollak, C. W. Higginbotham and M. Cardona, J. Phys. Soc. Japan Suppl. 21, (1966).
14. L. Van Hove, Phys. Rev. 89, 1189 (1953).
15. H. Ehrenreich, H. R. Philipp and J. C. Phillips, Phys. Rev. Letters 8, 59 (1962). The values have been adjusted to a temperature of 5K.

16. S. S. Vishnubhatla and J. C. Woolley, Canad. J. Phys. 46, 1769 (1968).

17. M. Cardona in Semiconductors and Semimetals, R. W. Willardson and A. C. Beer, eds. (Acacemic Press, New York, 1967), Vol. 3, p. 138.

18. C. Varea de Alvarez, J. P. Walter, M. L. Cohen, S. Stokes and Y. R. Shen, Phys. Rev. B6, 1412 (1972).

19. In discussing gaps or transitions, the valence band is listed first, then the conduction band, e.g., $\Gamma_8 - \Gamma_6$ means Γ_8(valence) and Γ_6(conduction). Another notation will also be used, e.g., Λ(4-5) means a transition occurring between bands 4 and 5 (small splittings like those found along Γ-K not included) at the Λ point in the Brillouin zone. The first valence band is labelled 1; the first conduction band is 5.

20. J. R. Dixon and J. M. Ellis, Phys. Rev. 123, 1560 (1961).

21. F. Matossi and F. Stern, Phys. Rev. 111, 472 (1958).

22. R. R. L. Zucca and Y. R. Shen, Phys. Rev. B1, 2668 (1970).

23. H. Ehrenreich, J. Appl. Phys. Suppl. 32, 2155 (1961).

24. M. Cardona, K. L. Shalkee and F. H. Pollak, Phys. Rev. 154, 696 (1967).

25. R. Glosser, J. E. Fischer and B. O. Seraphin, Phys. Rev. B1, 1607 (1970).

26. W. J. Turner, W. E. Reese and G. D. Pettit, Phys. Rev. 136, A1467 (1964).

27. R. Zallen and W. Paul, Phys. Rev. 134, A1628 (1964).

28. W. Paul in Les Proprietes Physiques des Solides Sous Pression, Colloques Internationaux de Centre National de la Recherche Scientifique, Grenoble, 1969, p. 199.

29. B. W. Hakki, A. Jayaraman and C. K. Kim, J. Appl. Phys. 41, 5291 (1970).

30. More recently A. Anton, et al. (Phys. Rev. Lett. 28, 966 (1972)) have been able to measure optical transitions from the Γ_1^c conduction band to the subsidiary X_1^c conduction band at 8°K. They report a X_1^c-Γ_1^c interband energy of 960 5 MeV, therefore, a value of 2.39 eV for the indirect Γ_{15}-X_1 gap. Probably the difference between this result and the result of Ref. 29 is due to the linear extrapolation in the latter.
31. R. N. Cahn and M. L. Cohen, Phys. Rev. B1, 2569 (1970).
32. J. C. Phillips and J. A. Van Vechten, Phys. Rev. B2, 2147 (1970).
33. A compendium of the known values of the crystal parameters of chalcopyrite compounds appears in D. S. Chemla, Phys. Rev. Lett. 26, 1441 (1971).
34. L. Pauling, The Nature of the Chemical Bond (Cornell University Press, N. Y., 1960).
35. J. A. Van Vechten and J. C. Phillips, Phys. Rev. B2, 2160 (1970).
36. S. C. Abrahams and J. L. Bernstein, J. Chem. Phys. 55, 796 (1971).
37. C. Varea de Alvarez and M. L. Cohen, Phys. Rev. Lett. 30, 979 (1973).
38. D. E. Eastman, M. L. Cohen and W. D. Grobman, Phys. Lett.
    D. J. Chadi, M. L. Cohen and W. D. Grobman (to be published).
39. J. L. Shay, E. Buehler and J. H. Wernick, Phys. Rev. B4, 2479 (1971) and references therein.
40. R. A. Bendorius, G. Z. Krivaite, A. Yu. Shileika, G. F. Karavaev and V. A. Chaldyshev, International Conference on Semiconductors, Warsaw, 1972.
41. J. L. Shay, B. Tell, E. Baehler and J. H. Wernick, Phys. Rev. Lett. 30, 983 (1973).

43. K. Kreher (to be published). The Ionincities of $A^2B^4C^5_2$ Compounds is published in K. Hubner and K. Unger, Phys. Stat. Sol. (b) 50, K105 (1972).

44. J. E. Rowe and J. L. Shay, Phys. Rev. B3, 451 (1971).

45. J. L. Shay, E. Buehler and J. H. Wernick, Phys. Rev. B2, 4104 (1970). and Phys. Rev. B4, 2479 (1971); J. L. Shay and E. Buehler, Phys. Rev. B3, 2598 (1971); C. C. Y. Kwan and J. C. Woolley, Phys. State. Sol. (b) 44, K93 (1971); Appl. Phys. Letters 18, 520 (1971); R. K. Karymshakov, Y. I. Ukhanov and Y. V. Shmartsev, Fiz. Tekh. Poluprov. 5, 514 (1971) [Sov. Phys. Semiconductors 5, 540 (1971)]; J. Kavaliauskas, G. F. Karavaev, E. I. Leonov, V. M. Orlov, V. A. Chaldyshev and A. Shileika, Phys. Stat. Sol. (b) 45, 443 (1971). R. A. Bendorius, V. D. Prochukhan and A. Shileika, Phys. Stat. Sol. (b) 53, 745 (1972) [see also Ref. 40, 41, 44, 46, 47 and 49].

46. Y. Petroff, S. Kohn and Y. R. Shen, Paper given at the *International Conference on Modulation Spectroscopy, Tucson, 1972*, November 23-26, 1972.

47. S. E. Stokowski, Phys. Rev. B6, 1294 (1972).

48. C. Varea de Alvarez and M. L. Cohen, to be published.

49. C. C. Y. Kwan and J. C. Woolley, Canad. J. Phys. 48, 2085 (1970.

50. J. Zak, *The Irreducible Representations of Space Groups* (Benjamin, New York, 1969).

51. A. Baldareschi, Phys. Rev. B 7, 5212 (1973); D. J. Chadi and M. L. Cohen, Phys. Rev. B 7, 692 (1973).

Table I. Comparison of the main energy gaps between model potentials I, II, III and those calculated by Cohen and Bergstresser.[4]

	$\Gamma_{25'}-\Gamma_{2'}$	$\Gamma_{25'}-\Gamma_{15}$	$\Gamma_{25'}-L_1$	$\Gamma_{25'}-X_1$	$L_{3'}-L_1$	X_4-X_1
Exp	1.0	3.4	0.8	0.1	2.1	4.3
CB	1.2	3.5	0.9	1.0	2.0	3.8
I	1.0	2.1	0.41	0.34	1.74	3.5
II	0	2.20	-0.07	0.25	1.24	3.35
III	-3.08	3.4	-1.46	-0.07	-0.19	2.85

Table II. A comparison of the form factor (Ry) of Cohen and Bergstresser (Ref. 2) with the form factors used in the present calculation. The lattice constants are also given.

	InAs		InSb		InP		GaP	
	C-B*	Present Work	C-B*	Present Work	C-B*	Present Work	C-B*	Present Work
Lattice Constant	6.04 A	6.053**	6.48	6.473**	5.86	5.852	5.44	5.44
$V^S(3)$	-0.22 Ry	-0.2699	-0.20	-0.2547	-0.23	-0.2704	-0.22	-0.225
$V^S(8)$	0.0	0.0196	0.0	0.0188	0.01	0.0345	0.03	0.024
$V^S(11)$	0.05	0.0411	0.04	0.0452	0.06	0.0442	0.07	0.076
$V^A(3)$	0.08	0.0775	0.06	0.0302	0.07	0.0888	0.12	0.128
$V^A(4)$	0.05	0.0384	0.05	0.0012	0.05	0.054	0.07	0.053
Metallic Spin-Orbit Parameter		0.00137		0.00203				
Non-Metallic Spin-Orbit Parameter		0.00109		0.00260				

*M. L. Cohen and T. K. Bergstresser, Phys. Rev. 141, 789 (1966).

**V. G. Giesecke and H. Pfister, Acta. Cryst. 11, 369 (1958). S. I. Novikova, Soviet Physics Solid State 2, 2087 (1961). Lattice constants were scaled to a temperature of 5°K, except in the case of GaP.

Table III. Identification of transitions responsible for the prominent theoretical and experimental reflectivity structure in InAs, including location in the Brillouin zone, energy, and symmetry of calculated critical points.

Reflectivity Structure		Associated Critical Points (InAs)		
Theory	Exper.*	Location in Zone	Symmetry	c_p Energy
0.46 eV	0.42 eV**	Γ(4-5)(0,0,0)	M_0	0.46 eV
2.58 eV	2.61 eV	Λ(4-5)(0.3,0.3,0.3)	M_1	2.47 eV
		L(4-5)(0.5,0.5,0.5)	M_1	2.48 eV
2.85 eV	2.88 eV	Λ(3-5)(0.3,0.3,0.3)	M_1	2.74 eV
		L(3-5)(0.5,0.5,0.5)	M_1	2.75 eV
4.37 eV	4.39 eV	Δ(4-5)(0.7,0,0)	M_1	4.3 eV
		Γ(4-6)(0,0,0)	--	4.37 eV
4.47 eV	4.58 eV	X(4-5)(1.0,0,0)	M_1	4.43 eV
		Vol. near (3-5)(0.7,0,0)	--	4.43 eV
4.7 eV	4.74 eV	Σ(4-5)(0.7,0.7,0)	M_2	4.65 eV
		Δ(3-6)(0.3,0,0)	M_1	4.69 eV
5.3 eV	5.31 eV	Vol. near Δ(4-6)(0.7,0,0)	--	5.25 eV
5.57 eV	5.5 eV	Vol. near Δ(3-6)(0.7,0,0)	--	5.39 eV
6.05 eV	6.5 eV†	L(4-7)(0.5,0.5,0.5)	M_0	5.91 eV
		Λ(4-7)(0.4,0.4,0.4)	M_1	5.96 eV
6.44 eV	6.8 eV†	L(3-7)(0.5,0.5,0.5)	M_0	6.18 eV
		Λ(3-7)(0.4,0.4,0.4)	M_1	6.23 eV
7.37 eV	7.1 eV†	Vol. near (4-7)(0.4,0.3,0.1)	--	7.05 eV

*R. R. L. Zucca and Y. R. Shen, Phys. Rev. B1, 2668 (1970), except as listed below.

**I. R. Dixon and J. M. Ellis, Phys. Rev. 123, 1560 (1961).

†H. Ehrenreich, H. R. Phillip and J. C. Phillips, Phys. Rev. Lett. 8, 59 (1962). These values have been adjusted to a temperature of 5K.

Table IV. Identification of transitions responsible for the prominent theoretical and experimental reflectivity structure in InSb including location in the Brillouin zone, energy and symmetry of the calculated critical points.

Reflectivity Structure		Associated Critical Points (InSb)		
Theory	Exper.*	Location in Zone	Symmetry	c_p Energy
0.26 eV	0.24 eV**	Γ(4-5)(0,0,0)	M_0	0.26 eV
2.03 eV	1.98 eV	Λ(4-5)(0.3,0.3,0.3)	M_1	1.94 eV
		L(4-5)(0.5,0.5,0.5)	M_1	2.0 eV
2.60 eV	2.48 eV	Λ(3-5)(0.3,0.3,0.3)	M_1	2.5 eV
		L(3-5)(0.5,0.5,0.5)	M_1	2.55 eV
3.65 eV	3.39 eV	Δ(4-5)(0.7,0,0)	M_1	3.65 eV
3.83 eV	3.78 eV	Δ(3-5)(0.7,0,0)	M_1	3.83 eV
4.15 eV	4.23 eV	Δ(3-6)(0.2,0,0)	M_1	3.95 eV
		Σ(4-5)(0.7,0.7,0)	M_2	4.1 eV
4.48 eV	4.56 eV	vol. near Δ(4-6)(0.5,0,0)	--	4.75 eV
4.73 eV	4.75 eV	Δ(4-6)(0.7,0,0)	M_3	4.75 eV
4.95 eV	4.92 eV	L(4-6)(0.5,0.5,0.5)	M_0	4.86 eV
		Λ(4-6)(0.4,0.4,0.4)	M_1	4.87 eV
		Δ(3-6)(0.7,0,0)	M_3	4.94 eV
5.3 eV	5.33 eV	L(3-6)(0.5,0.5,0.5)	M_0	5.41 eV
		Λ(3-6)(0.4,0.4,0.4)	M_1	5.43 eV
6.01 eV	5.96 eV	L(3-7)(0.5,0.5,0.5)	M_0	5.64 eV
		Λ(3-7)(0.4,0.4,0.4)	M_1	5.69 eV

[*] R. R. L. Zucca and Y. R. Shen, Phys. Rev. B1, 2668 (1970), except for b.

[**] H. Ehrenreich, J. Appl. Phys. Suppl. 32, 2155 (1961).

Table V. Identification of transitions responsible for the prominent theoretical and experimental reflectivity structure in InP, including location in the Brillouin zone, energy and symmetry of calculated critical points (cp).*

Theory	Experiment	Location in Zone	Symmetry	c_p Energy
1.43 eV**	1.42 eV†	Γ(4-5)(0,0,0)	M_0	1.5 eV
3.23 eV**	3.24 eV	L(4-5)(0.5,0.5,0.5)	M_0	3.2 eV
3.37 eV**	3.38 eV	Λ(4-5)(0.3,0.3,0.3)	M_1	3.22 eV
4.75 eV	4.78 eV	Δ(4-5)(0.8,0,0)	M_0	4.7 eV
		X(4-5)(1.0,0,0)	M_1	4.71 eV
		Volume near (4-5)(0.3,0,0)	--	4.88 eV
5.06 eV	5.10 eV (5.05 eV)	Σ(4-5)(0.7,0,7,0)	M_2	5.02 eV
5.48 eV	(5.25 eV)	Vol. (3-6)(0.3,0.1,0)	--	5.5 eV
5.86 eV	5.77(5.6)	Δ(4-6)(0.7,0,0)	M_1	5.77 eV
6.47 eV	(6.57 eV)	L(4-6)(0.5,0.5,0.5)	M_0	6.2 eV
		Λ(4-6)(0.4,0.4,0.4)	M_1	6.28 eV

*Data in parentheses from Woolley-Vishnubhatla, Canad. J. Phys. 46, 1769 (1968). Other data from this paper's 5°K experiment.

**Corrected to include spin-orbit corrections.

†W. J. Turner, W. E. Reese and G. D. Pettit, Phys. Rev. 136, A1467 (1964).

Table VI. Identification of transitions responsible for the prominent theoretical and experimental reflectivity structure in GaP, including location in the Brillouin zone, energy and symmetry of calculated critical points (cp).

Theory	Experiment	Location in Zone	Symmetry	c_p Energy
2.79 eV	2.78 eV	Γ(4-5)(0,0,0)	M_0	2.79 eV
	2.86 eV			
3.70 eV	3.69 eV	L(4-5)(0.5,0.5,0.5)	M_0	3.40 eV
		Λ(4-5)(0.15,0.15,0.15)	M_1	3.76 eV
4.7	4.74	Δ(4-5)(0.71,0,0)	M_0	4.50 eV
		X(4-5)(1,0,0)	M_1	4.57 eV
5.3	5.31	Δ(4-5)(0.30,0,0)	M_3	4.72 eV
		Σ(4-5)(0.50,0.50,0)	M_2	5.20 eV

Table VII: Crystal parameters of $A^2B^4C^5_2$
chalcopyrite semiconductors.

Compound	a	c	ε $2-c/a$	u	σ $4u-1$	$\lvert\varepsilon-4\sigma\rvert$
$MgSiP_2$	5.718	10.109	0.232			
$ZnSiP_2$	5.398	10.434	0.067	0.2691	0.076	0.009
$ZnGeP_2$	5.465	10.71	0.040	0.2582	0.033	0.007
$ZnSnP_2$	5.65	11.30	0.000	0.239	-0.044	0.004
$CdSiP_2$	5.678	10.43	0.163			
$CdGeP_2$	5.741	10.776	0.123	0.283	0.132	0.009
$CdSnP_2$	5.900	10.93	0.148			
$ZnSiAs_2$	5.606	10.89	0.057			
$ZnGeAs_2$	5.672	11.15	0.034	0.264	0.056	0.022
$ZnSnAs_2$	5.852	11.704	0.000	0.239	-0.044	0.044
$CdSiAs_2$	5.884	10.879	0.151			
$CdGeAs_2$	5.943	11.22	0.112	0.285	0.144	0.032
$CdSnAs_2$	6.092	11.922	0.043	0.261	0.044	0.001

Table VIII. Experimental values of σ, and comparison with those predicted using Pauling's* additive radii of atoms (when in tetrahedral covalent bonds and Phillips and VanVechten's** covalent radii for the elements.

Compound	σ Experimental	σ Pauling	σ Phillips and VanVechten
$ZnSiP_2$	0.076	0.089	0.066
$ZnSiAs_2$		0.086	0.061
$ZnGeP_2$	0.033	0.057	0.0
$ZnGeAs_2$	0.056	0.055	0.0
$ZnSnP_2$	-0.044	-0.055	-0.110
$ZnSnAs_2$	-0.044	-0.053	-0.107

---

[*] L. Pauling, The Nature of the Chemical Bond (Cornell University Press, N. Y., 1960).

[**] J. A. VanVechten and J. C. Phillips, Phys. Rev. B2, 2160 (1970).

Table IX. Energies and Pronounced polerizations of the reflectivity spectra of $ZnGeP_2$.

	Experiment 1	Experiment 2		Experiment 3
	5°K	120°K	320°K	300°K
A		2.46	2.39 ∥	2.39 ∥
B		2.53	2.46 ⊥	2.40 ⊥
C		2.59	2.52 ⊥ (∥)	2.48 ∥ (⊥)
E_1(1)	3.02 ∥ ,⊥	3.02	2.97 ∥ (⊥)	2.87 ∥
				2.92 ⊥
E_1(2)	3.08 ⊥ ,∥	3.15	3.09 ⊥	3.05 ∥
E_1(3)	3.2 ⊥ (∥)	3.22	3.13 ∥	3.32 ∥⊥
E_1(4)	3.41 ⊥	3.48	3.41 ⊥ (∥)	3.64 ∥⊥
E_c	3.74(3.72) ∥ ,⊥	3.75	3.71 ∥ ,⊥	3.83 ⊥
E_2(1)	4.17 ⊥		4.14	4.05 ⊥

Experiment 1. Modulated Reflectivity, Y. Petroff, S. Kohn and Y. R. Shen, Paper given at the International Conference on Modulation Spectroscopy, Tucson, 1972, November 23-26, 1972.

Experiment 2. Thermoreflectance, A. Raudonis, V. S. Grigoreva, V. D. Prochukhan and A. Shileika Phys. Stat. Solidi (b) 57, 1973.

Experiment 3. J. L. Shay, B. Tell, E. Baehler and J. H. Wernick, Phys. Rev. Lett. 30, 983 (1973).

Table X. Reflectivity structure of $ZnGeP_2$.

Theory	Experiment†	Polarization	Peak	Location in Zone	Energy (eV)
	2.34**	∥⊥	A	$\Gamma_2^- - \Gamma_1^-$	2.31*
	2.40**	⊥	B	$\Gamma_1^- - \Gamma_1^-$	2.27*
	2.40**	∥⊥	C	$\Gamma_2^- - \Gamma_1^-$	2.40*
3.04		∥	$E_1(1)$	$X_1-X_1(15,16-17,18)$	$3.04\left\{\begin{matrix}3.05^*\\3.03^*\end{matrix}\right.$
3.41	3.02	∥,⊥		$N_1-N_1(16-17)(0.2,0.2,0.2)$	3.42*
3.37		⊥	$E_1(2)$	$X_1-X_1(13,14-17,18)$	$3.36\left\{\begin{matrix}3.35^*\\3.37^*\end{matrix}\right.$
3.41	3.08	⊥,∥		$N_2-N_1(15-17)(0.2,0.2,0.2)$	3.50
3.6	3.2	⊥(∥)	$E_1(3)$	$N_2-N_1(16-17)(0.3,0.3,0.19)$	3.6
3.9	3.41	⊥	$E_1(4)$	$\Sigma_2-\Sigma_1(16-18)(0.25,0.25,0)$	3.95
4.0	3.74(3.72)	∥(⊥)	E_c	$X_1-X_1(11,12-17,18)$ $\Lambda(13-17)(0,0,0.6)$	3.9
4.77	4.17	⊥	$E_2^{\perp}(1)$	$\Sigma(14-17)(0.25,0.25,0)$	4.6
4.76	4.3	∥	$E_2^{\parallel}(1)$	$\Delta(15-17)(0.34,0,0)$	4.76
4.6	4.46	⊥	$E_2^{\perp}(2)$	$\Gamma_5-\Gamma_2(13-18)$	4.77
5.05	4.73	∥	$E_2^{\parallel}(3)$	$(0.16,0.5,0)(14-17)$	5.05
4.96	4.79	⊥	$E_2^{\perp}(3)$	$X(16-20)$ and along	4.96
5.21	4.92(4.93)	∥(⊥)	$E_2^{\parallel}(4)$	$\Delta(15-18)(0.5,0,0)$	

[*] Spin-orbit included.

[**] J. L. Shay, B. Tell, E. Baehler and J. H. Wernick, Phys. Rev. Lett. 30, 983 (1973).

[†] Y. Petroff, S. Kohn and Y. R. Shen, paper given at the International Conference on Modulation Spectroscopy, Tucson, 1972, November 23-26, 1972. Except for **.

FIGURE CAPTIONS

Fig. 1. Pseudopotential parameters used in this work together with the Ge pseudopotential parameters of Heine and Animalu[5] and Cohen and Bergstresser.[4]

Fig. 2. Band structure for model pseudopotential I.

Fig. 3. Electronic charge density in the (1,-1,0) plane for model I (summed over the valence bands).

Fig. 4. Band structure for model II.

Fig. 5. Electronic charge density in the (1,-1,0) plane for model II (summed over the valence bands).

Fig. 6. Electronic charge density in the (1,-1,0) plane for the first valence band for model I.

Fig. 7. Electronic charge density in the (1,-1,0) plane for the first valence band for model II.

Fig. 8. Band structure for model III.

Fig. 9. Electronic charge density in the (1,-1,0) plane (summed over the valence bands) for model III.

Fig. 10. Band structure for the Fermi-Thomas model.

Fig. 11. Electronic charge density in the (1,-1,0) plane (summed over the valence bands) for the Fermi-Thomas model.

Fig. 12. Electronic band structure of InAs along the principal symmetry directions in the Brillouin zone. Some bands slightly split by spin-orbit interaction are drawn as degenerate because of the smallness of the splitting.

Fig. 13. Electronic band structure of InSb along the principal symmetry directions in the Brillouin zone. Some bands slightly split by spin-orbit interaction are drawn as degenerate because of the smallness of the splitting.

Fig. 14. Electronic band structure of InP along the principal symmetry directions in the Brillouin zone. The dotted line represents the corrected band structure $E(k) = E_{EPM}(k) - \alpha k^2$.

Fig. 15. Calculation of the imaginary part of the frequency dependent dielectric function for InAs.

Fig. 16. Calculation of the imaginary part of the frequency dependent dielectric function for InSb.

Fig. 17. Calculation of the imaginary part of the frequency dependent dielectric function for InP.

Fig. 18. Calculation and measured reflectivity for InAs. Experiment 1 is H. Ehrenreich, H. R. Philipp, and J. C. Phillips, Phys. Rev. Letters 8, 59 (1962). Experiment 2 is S. S. Vishnubhatla and J. C. Woolley, Canad. J. Phys. 46, 1769 (1968).

Fig. 19. Calculated and measured reflectivity for InSb. Experiment 1 is H. Ehrenreich, H. R. Philipp, J. C. Phillips, Phys. Rev. Letters 8, 59 (1962). Experiment 2 is S. S. Vishnubhatla and J. C. Woolley, Canad. J. Phys. 46, 1769 (1968).

Fig. 20. Calculated and measured reflectivity for InP. Experiment 1 is M. Cardona in Semiconductors and Semimetals, R. W. Willardson and A. C. Beer, eds. (Academic Press, N. Y., 1967), p. 138. Experiment 2 is S. S. Vishnubhatla and J. C. Wooley, Canad. J. Phys. 46, 1769 (1968); experiment 3, Ref. 18.

Fig. 21. Comparison of the theoretical and experimental modulated reflectivity spectrum for InAs. The experimental spectrum is from R. R. L. Zucca and Y. R. Shen. Phys. Rev. B1, 2668 (1970). Prominent structure is identified.

Fig. 22. Comparison of the theoretical and experimental modulated reflectivity spectrum for InSb. The experimental spectrum is from R. R. L. Zucca and Y. R. Shen. Phys. Rev. B1, 2668 (1970). Prominent structure is identified.

Fig. 23. Comparison of the theoretical and experimental modulated reflectivity spectrum for InP. Experimental curve is at 5°K.

Fig. 24. Comparison of the theoretical (J. P. Walter and M. L. Cohen, Phys. Rev. 183, 763 (1970)) and experimental modulated reflectivity spectrum for GaP. Experimental curve is at 300°K.

Fig. 25. Location of atoms in the primitive cells. A section of the (1,-1,0) plane is shown bounded by dashed lines.

Fig. 26. InAs charge density--sum of valence bands 1-4.

Fig. 27. InSb charge density--sum of valence bands 1-4.

Fig. 28. Pressure dependences of a few important gaps in Si.

Fig. 29. Electronic charge densities corresponding to the $\Gamma^{v}_{25'}$, $\Gamma^{c}_{2'}$, L^{c}_{1}, and X^{c}_{1} as function of position along the (1,1,1) direction.

Fig. 30. Valence band charge densities as function of position in the (1,-1,0) plane for Si at 0 k-bar (a) and 120 k-bar (b) of pressure.

Fig. 31. Valence band charge density in the (1,-1,0) plane for InP at 0 k-bar of pressure.

Fig. 32. Valence band charge density in the (1,-1,0) plane for InP at 100 k-bar of pressure.

Fig. 33. Irreducible part of the chalcopyrite Brillouin zone. Dashed lines represent the "practical irreducible part of the Brillouin zone".

Fig. 34. Planes $k_z = 0$ (a), $k_z = 1$ (b), $k_z = 1/2$ (c) of the zincblende Brillouin zone and how they map into the plane $k_z = 0$ of the chalcopyrite Brillouin zone (d). Points marked by (x) of (a), (b) and (c) map into the point Γ of (e).

Fig. 35. Planes $k_x = k_y$ (a), $(1 - k_x) = k_y$ (b) of the zincblende Brillouin Zone. Figure (c) shows the N plane of the chalcopyrite BZ and (d) the folding in process. Points marked by (x) of (a) and (b) map into the point Γ of (c).

Fig. 36. (a) Band structure of $ZnGeP_2$, form factors of Zn extracted from ZnS, of P from GaP, for Ge the form factors are extrapolated from the Ge C·B form factors. (b) Band structure of GaP stressed along the (0,0,1) axis; the c/a ratio is that of $ZnGeP_2$.

Fig. 37. Calculation of the imaginary part of the frequency dependent dielectric function for $ZnGeP_2$. The form factors used are such that the zincblende component is the same as GaP. The chalcopyrite component was extracted from this assumption and the known form factors of Ge.

Fig. 38. Density of states curve for $ZnGeP_2$ and corresponding band structure. The parameters used in this calculation are the same ones as those in Fig. 42.

Fig. 39. Theoretical and experimental reflectivity spectra for $ZnGeP_2$. The parameters used in this calculation are the same ones as those in Fig. 42.

Fig. 40. (a) Band Structure of $ZnGeAs_2$, form factors of Zn extracted from ZnSe, of As from GaAs, for Ge, the form factors are extrapolated from the Ge C-B form factors. (b) Band structure of GaAs stressed along the (0,0,1) axis; the c/a ratio is that of $ZnGeAs_2$.

Fig. 41. Wannier function along the (1,1,1) direction corresponding to the first valence band of Si.

Fig. 42. Wannier function along the (1,1,1) direction corresponding to the second valence band of Si.

Fig. 43. Wannier function along the (1,1,1) direction corresponding to the third valence band of Si.

Fig. 44. Wannier function along the (1,1,1) direction corresponding to the fourth valence band of Si.

Fig. 45. Composite Wannier function along the (1,1,1) direction corresponding to the four valence bands of Si.

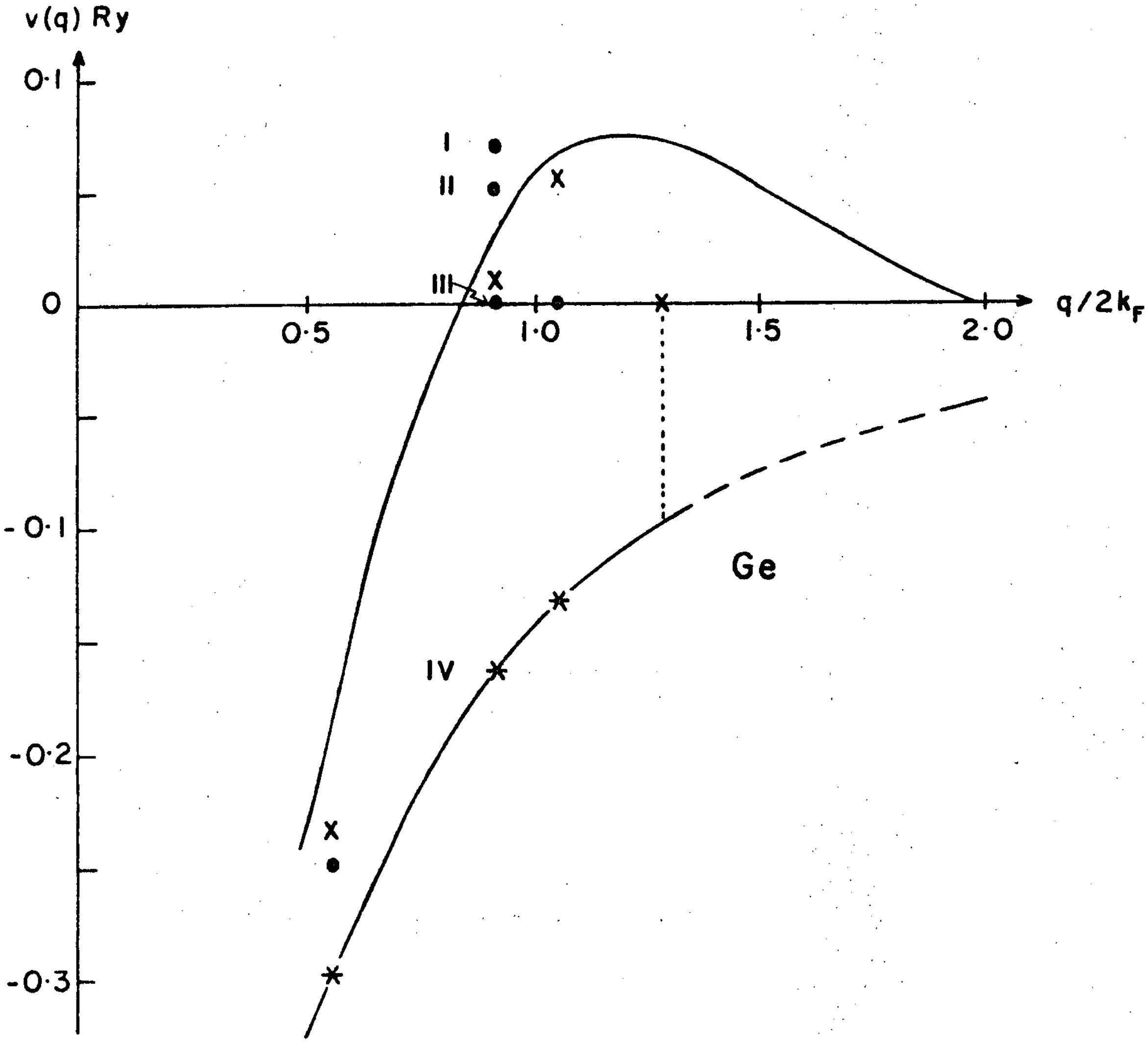

XBL 737-6524

Fig. 1

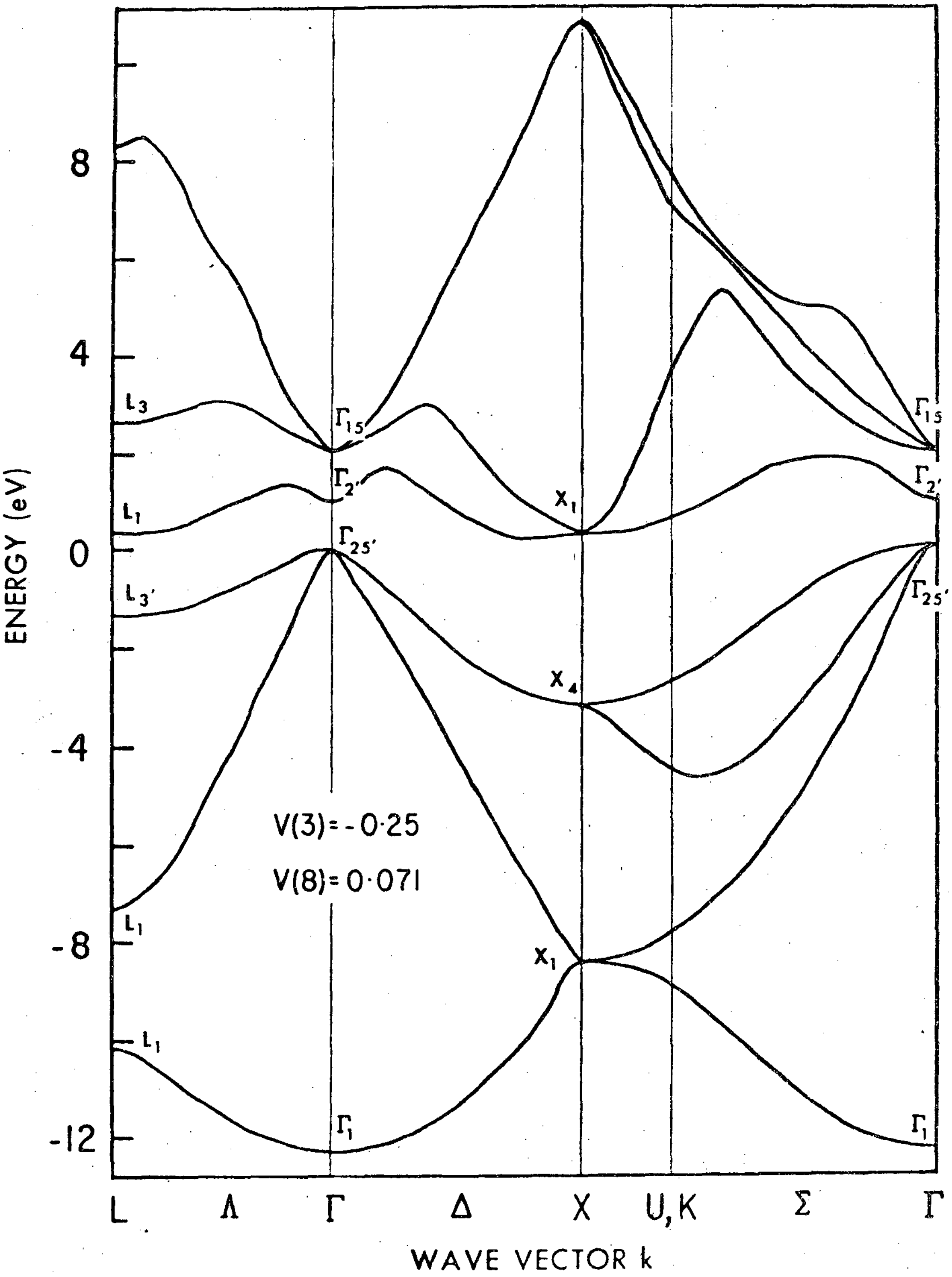

XBL 737-6525

Fig. 2

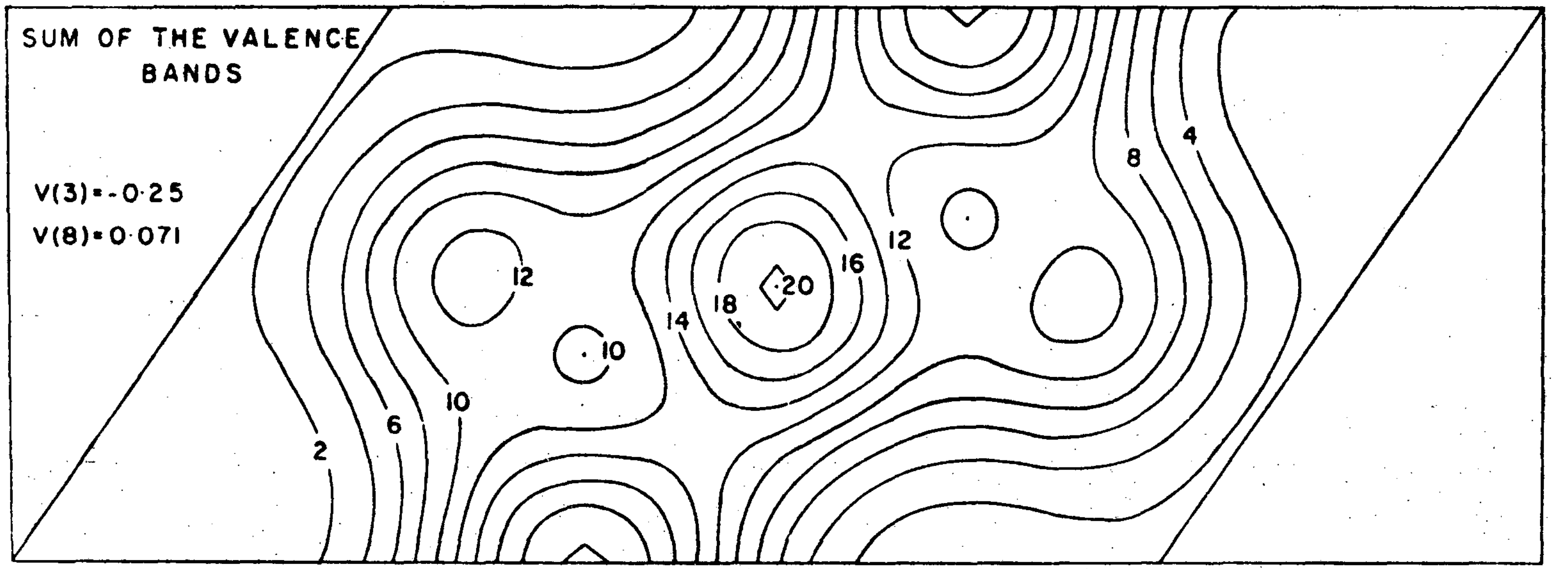

XBL 737-6526

Fig. 3

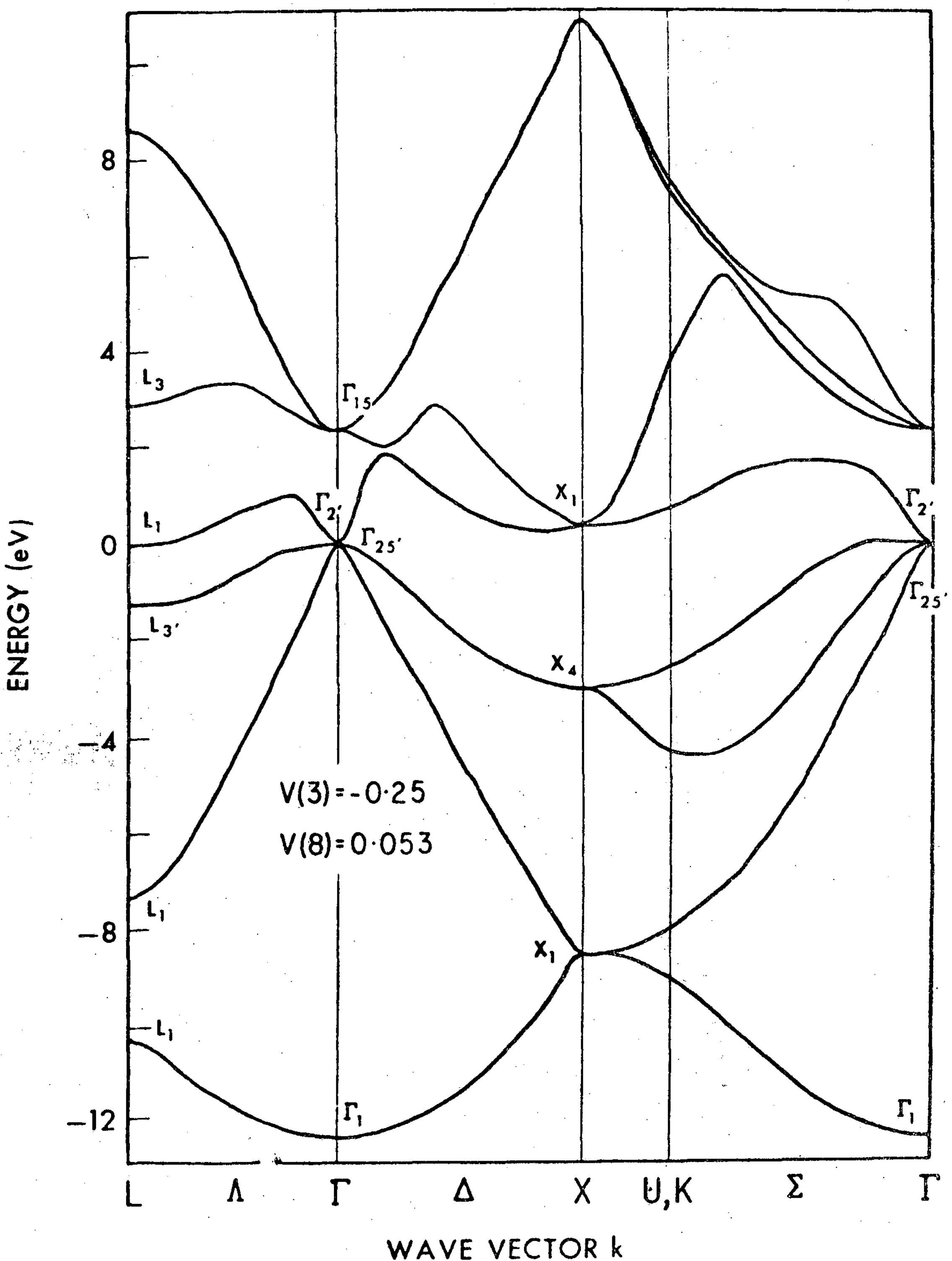

XBL 737-6527

Fig. 4

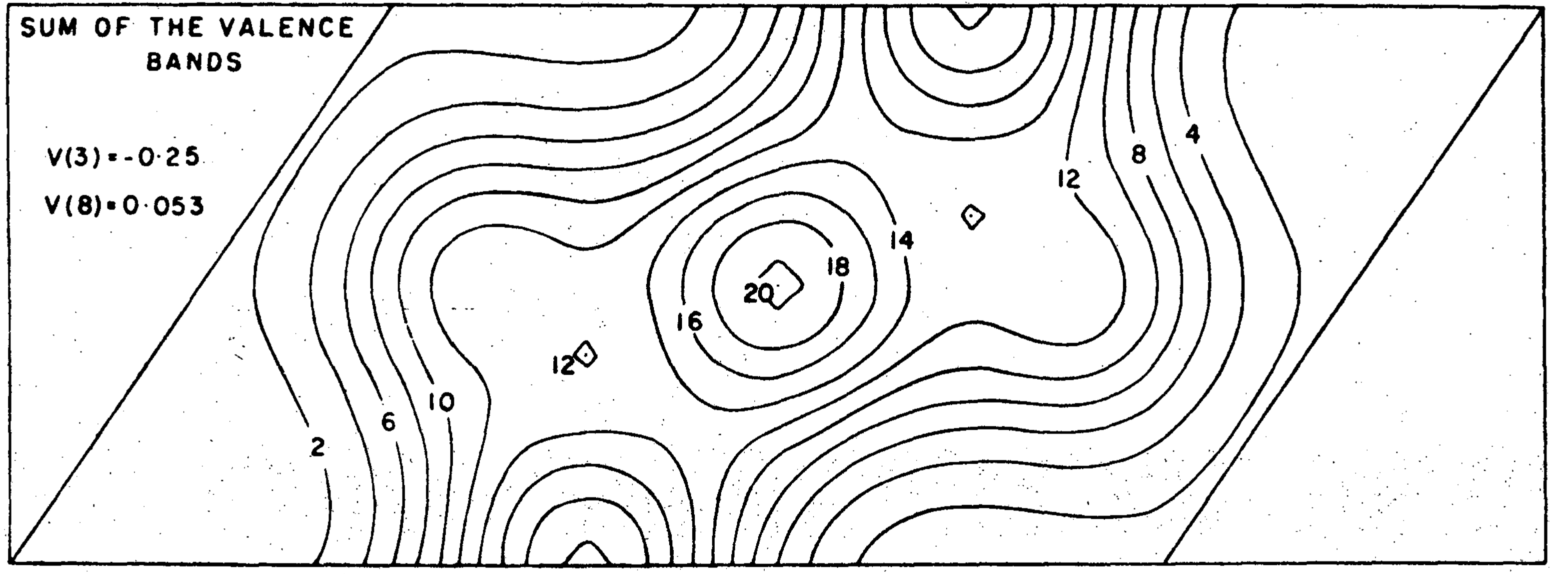

XBL 737-6528

Fig. 5

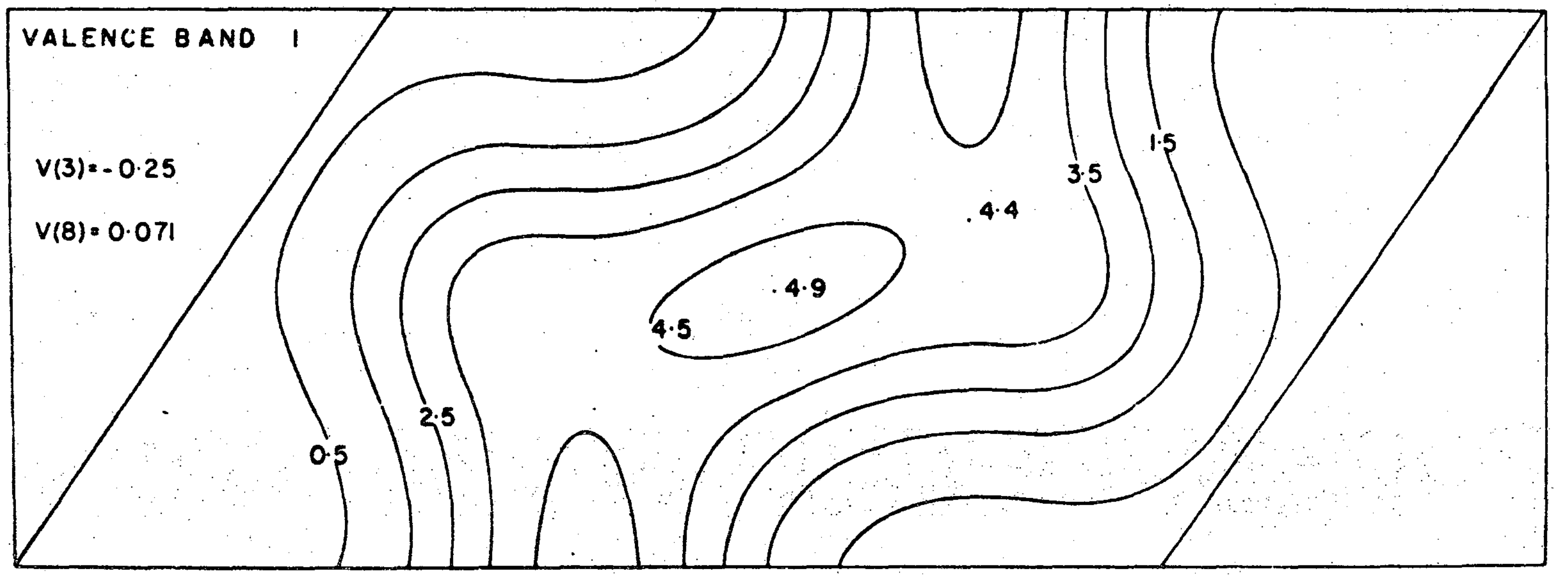

XBL 737-6529

Fig. 6

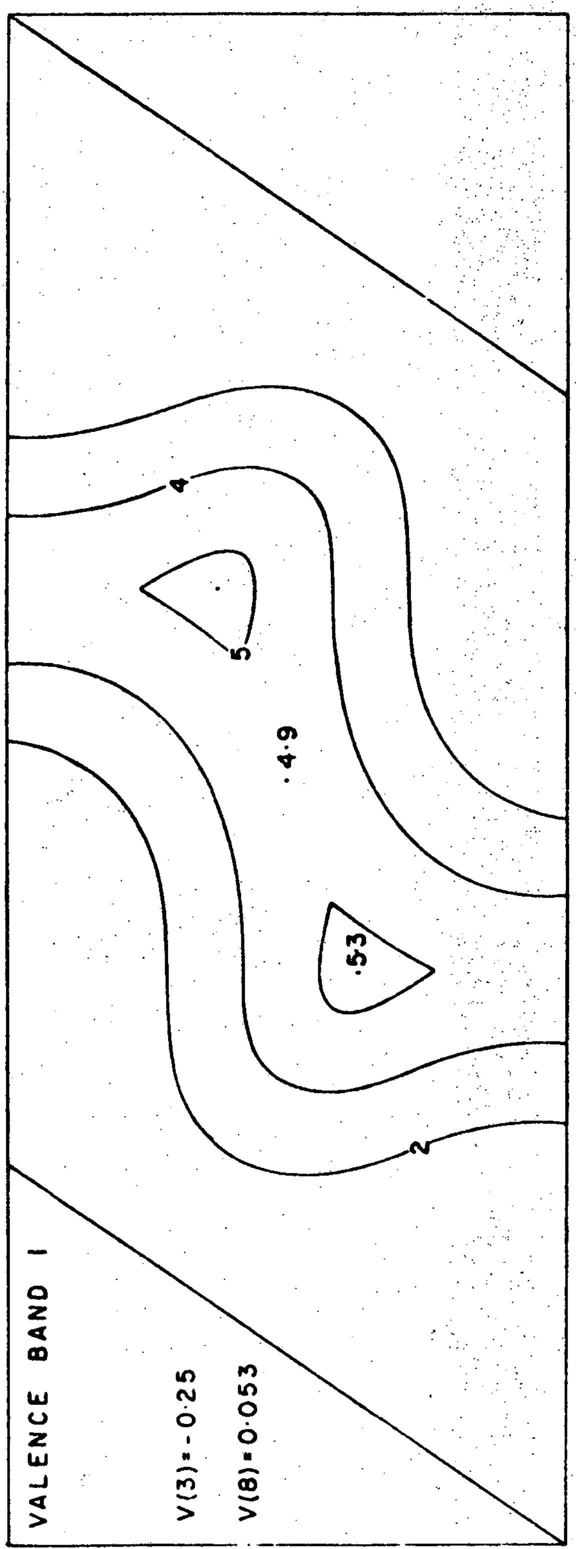

XBL 737-6530

Fig. 7

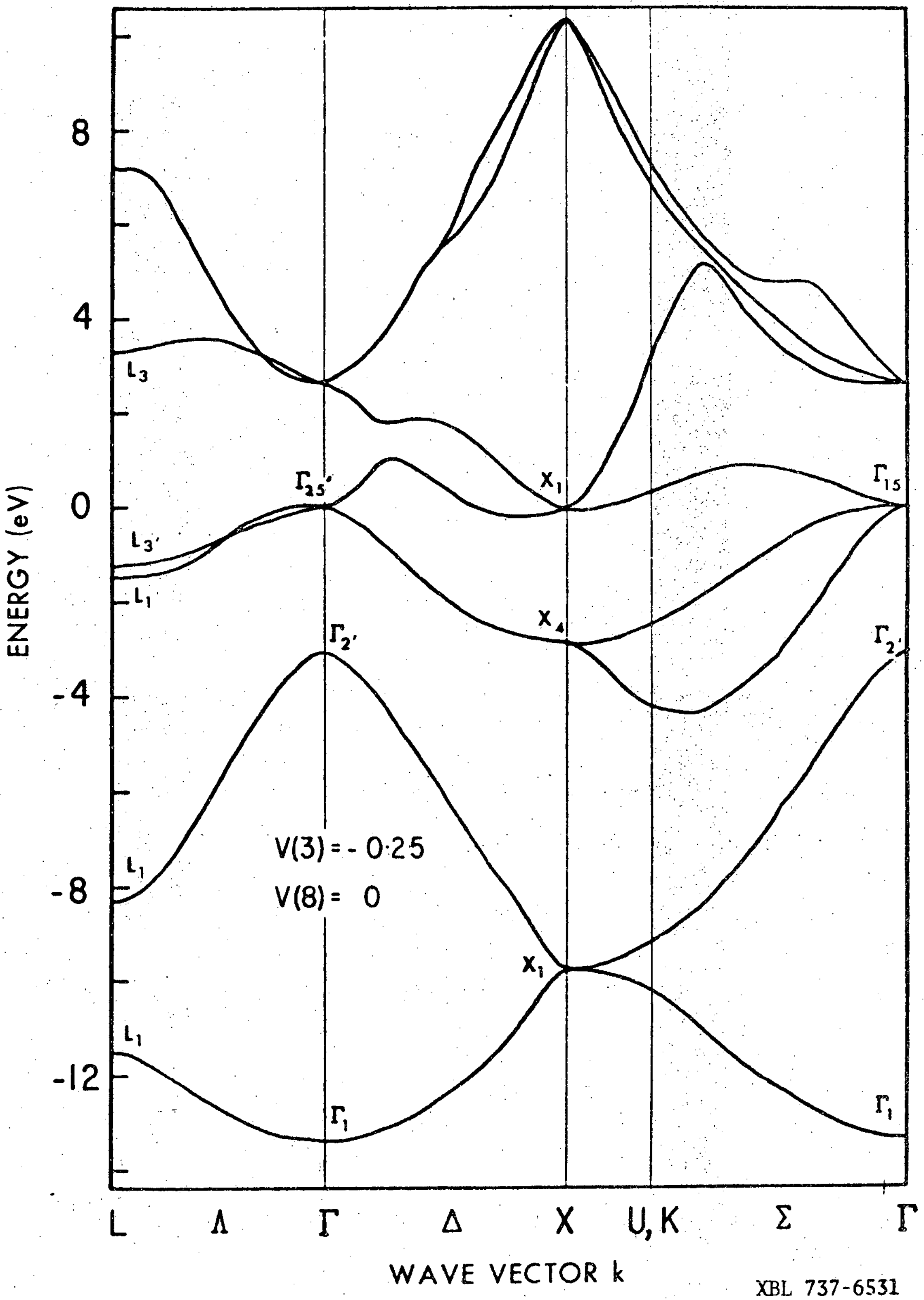

XBL 737-6531

Fig. 8

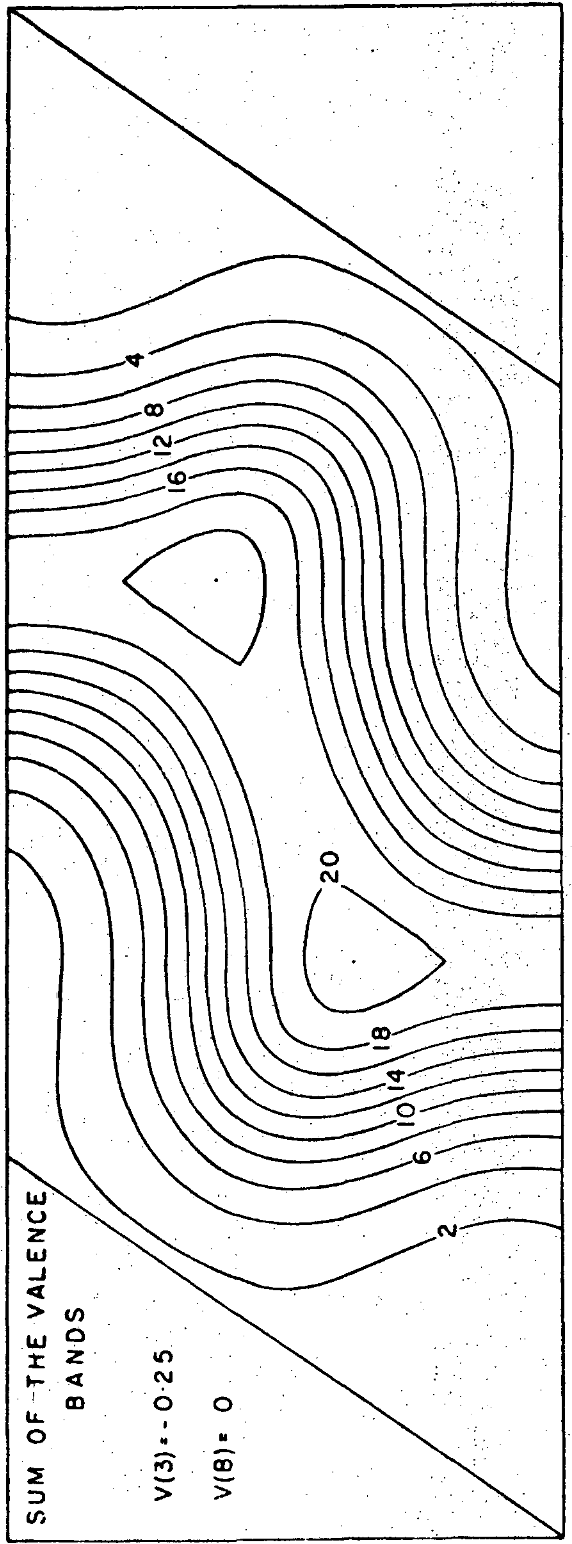

XBL 737-6532

Fig. 9

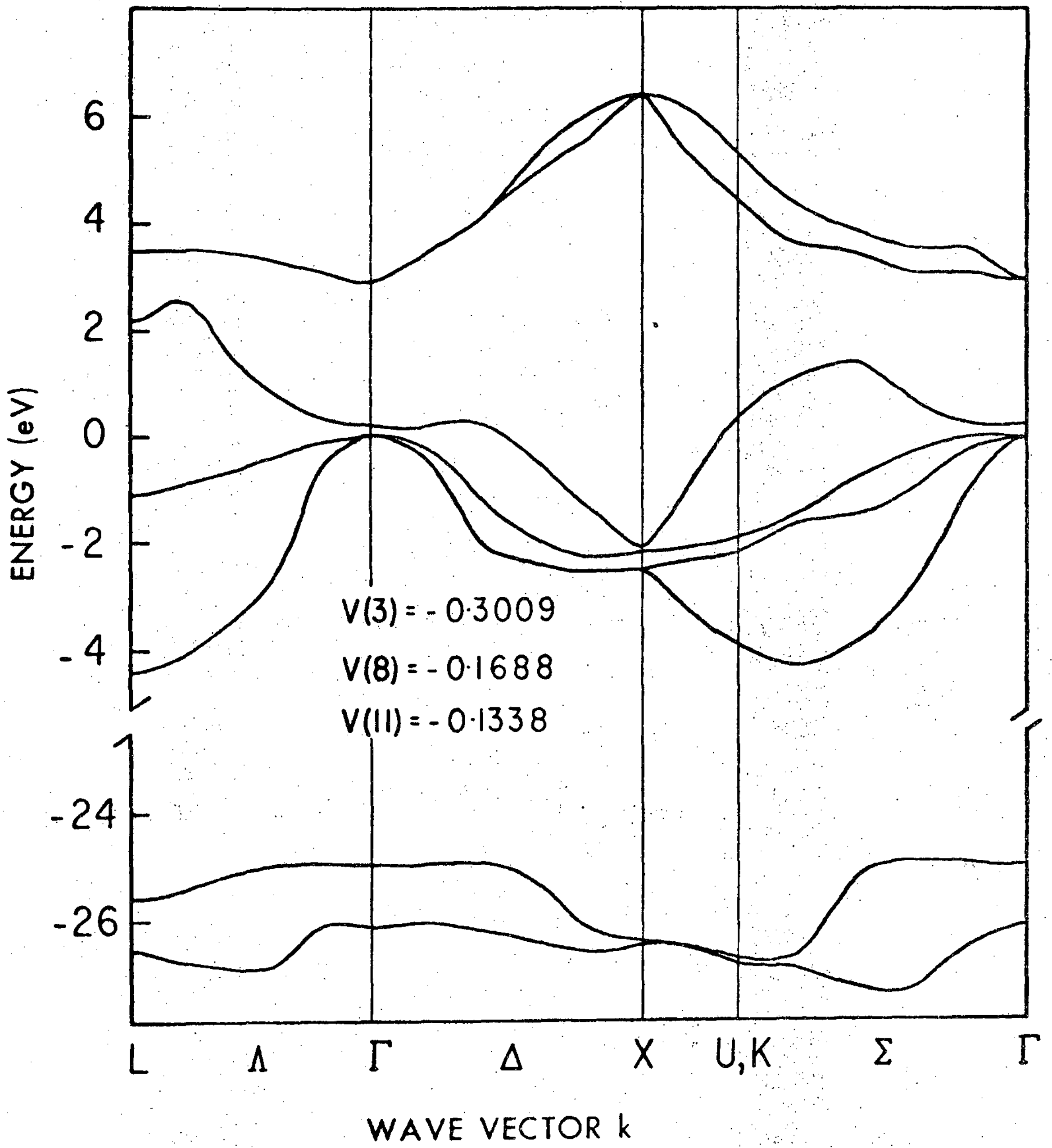

XBL 737-6533

Fig. 10

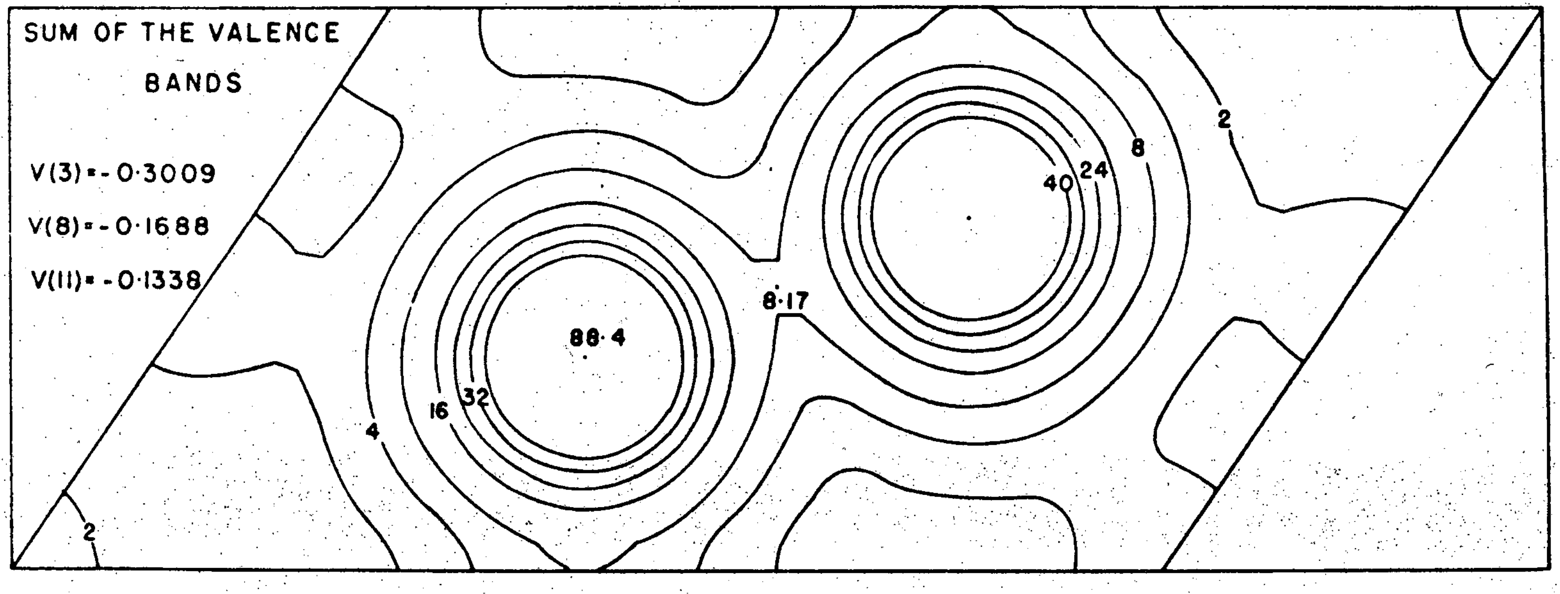

XBL 737-6534

Fig. 11

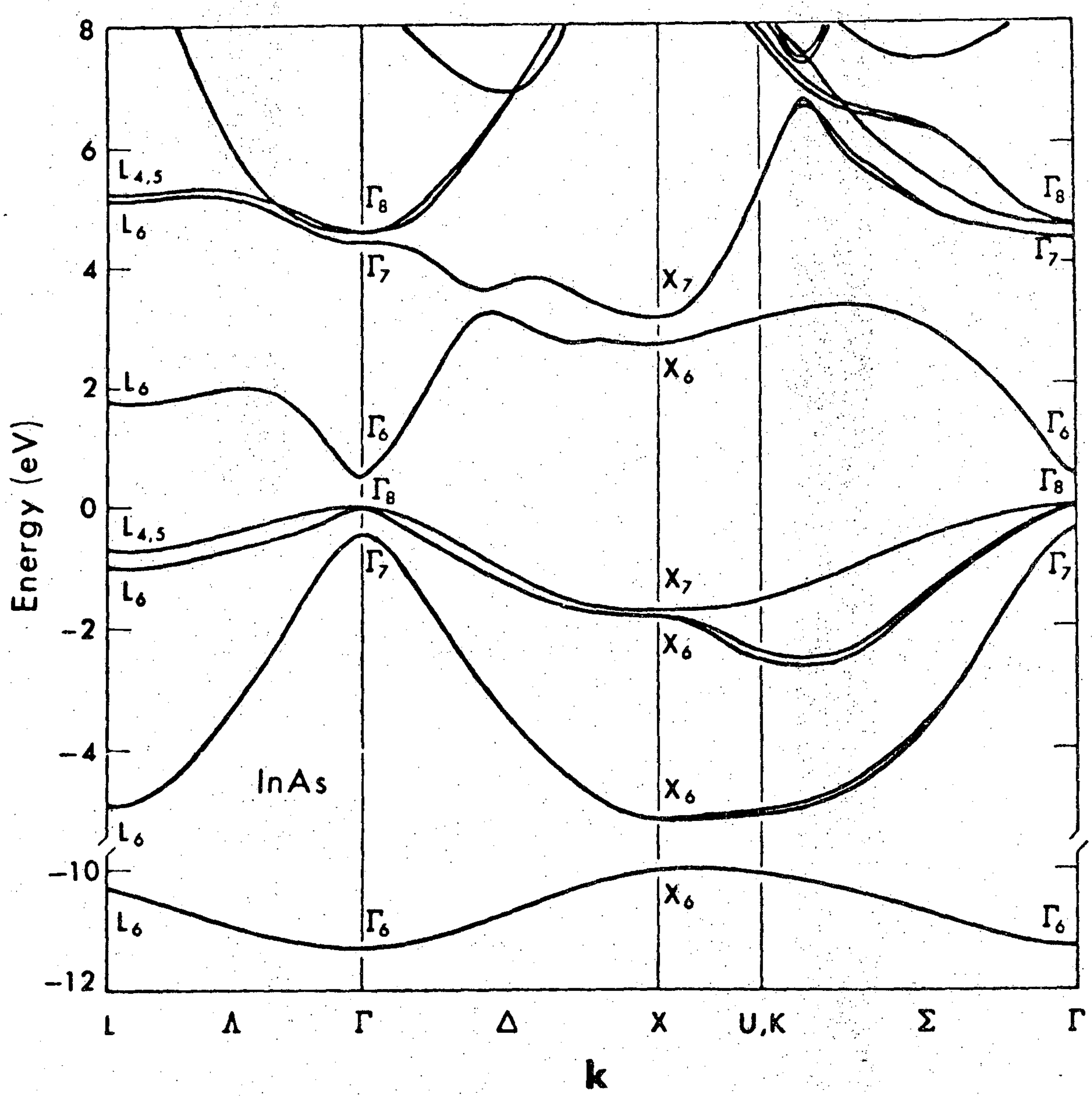

XBL 737-6535

Fig. 12

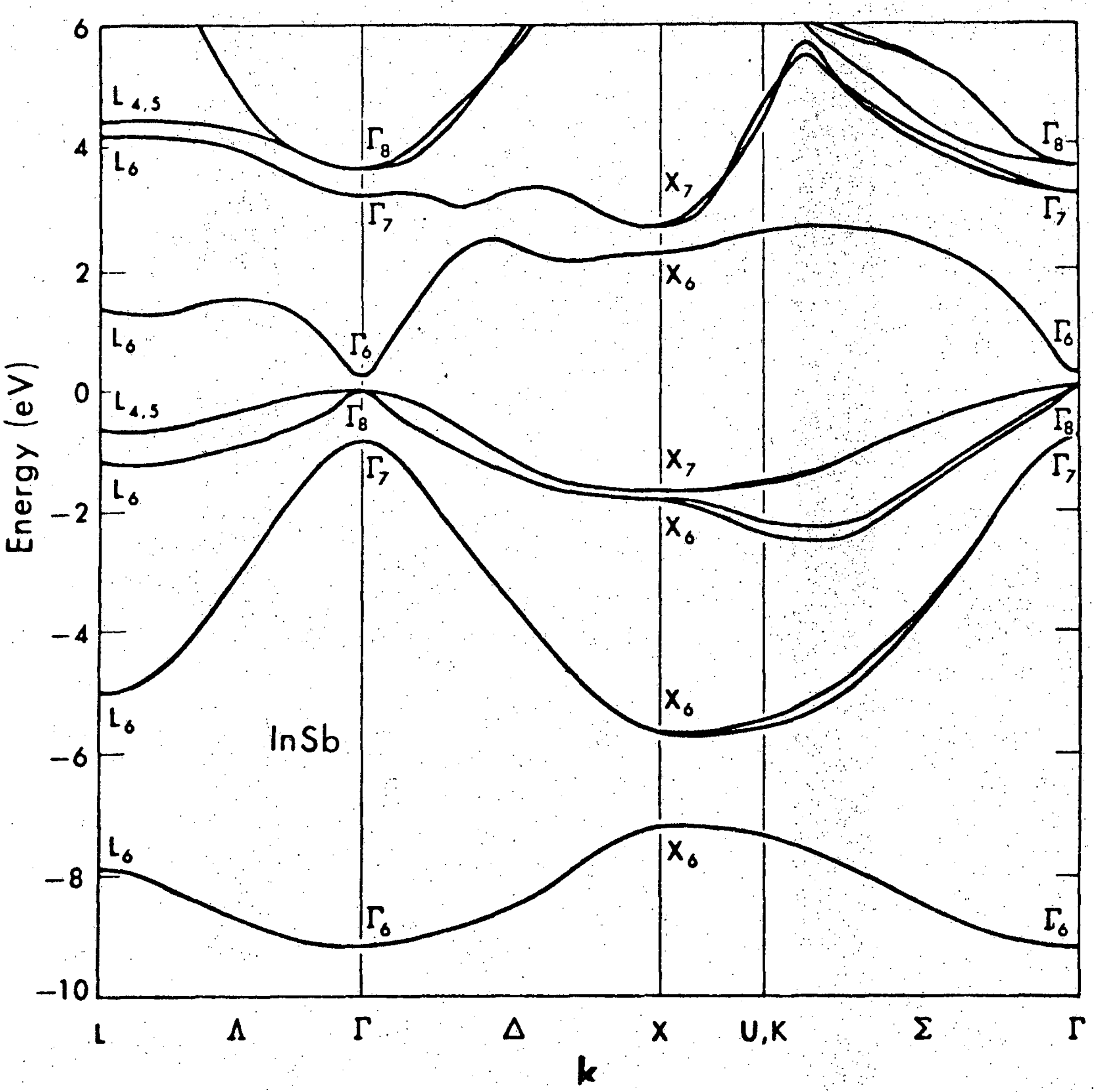

XBL 737-6536

Fig. 13

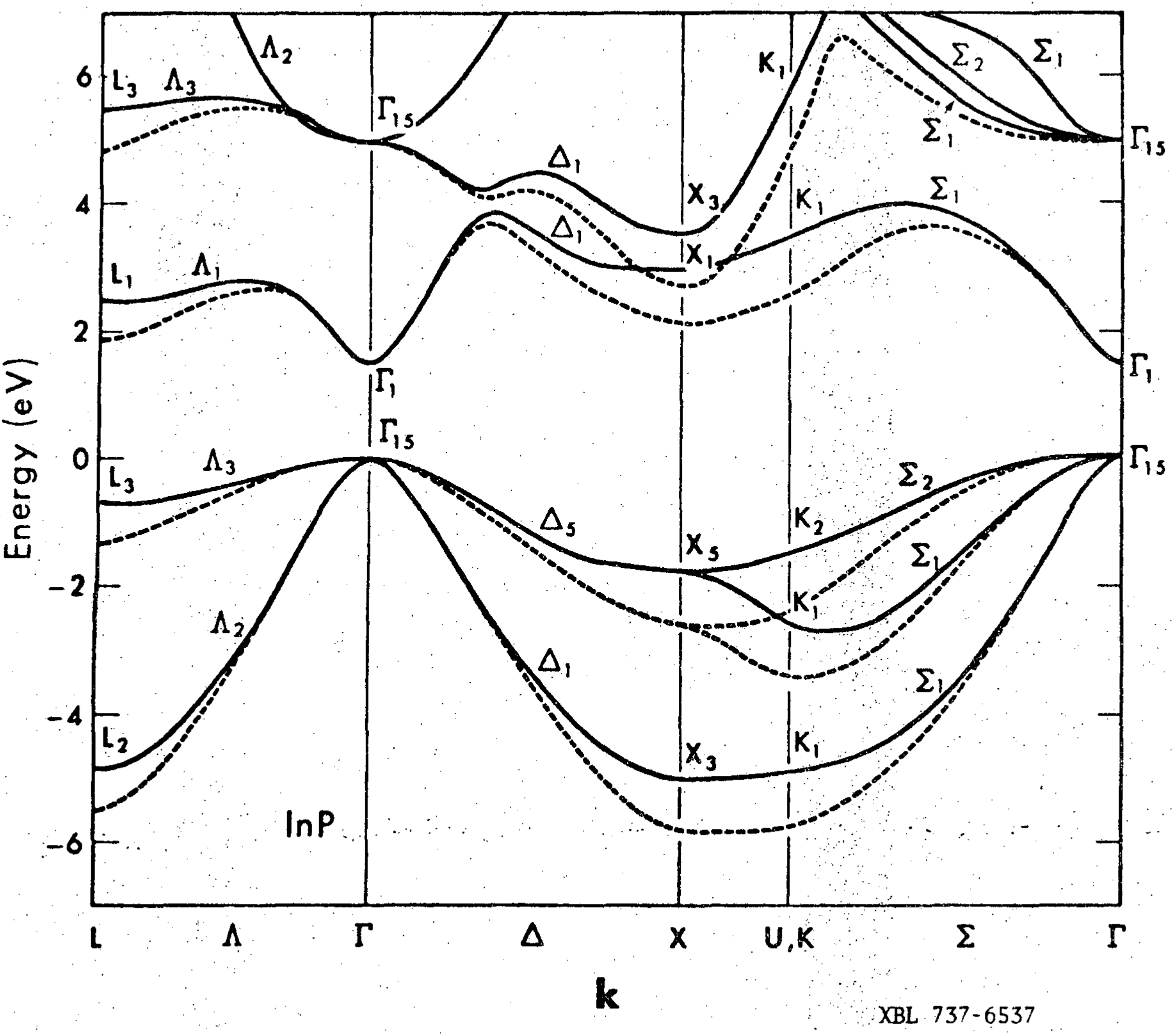

XBL 737-6537

Fig. 14

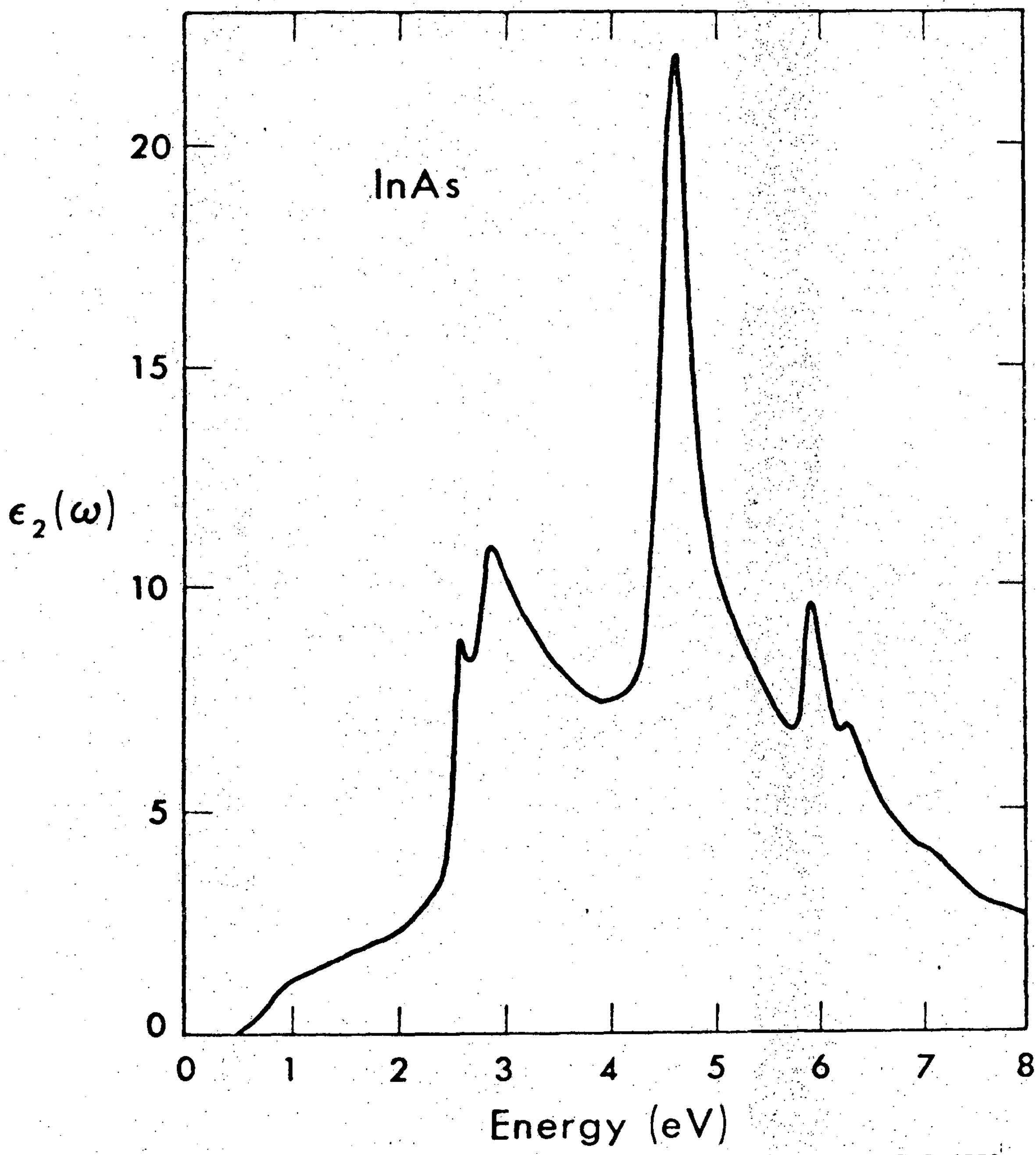

XBL 737-6538

Fig. 15

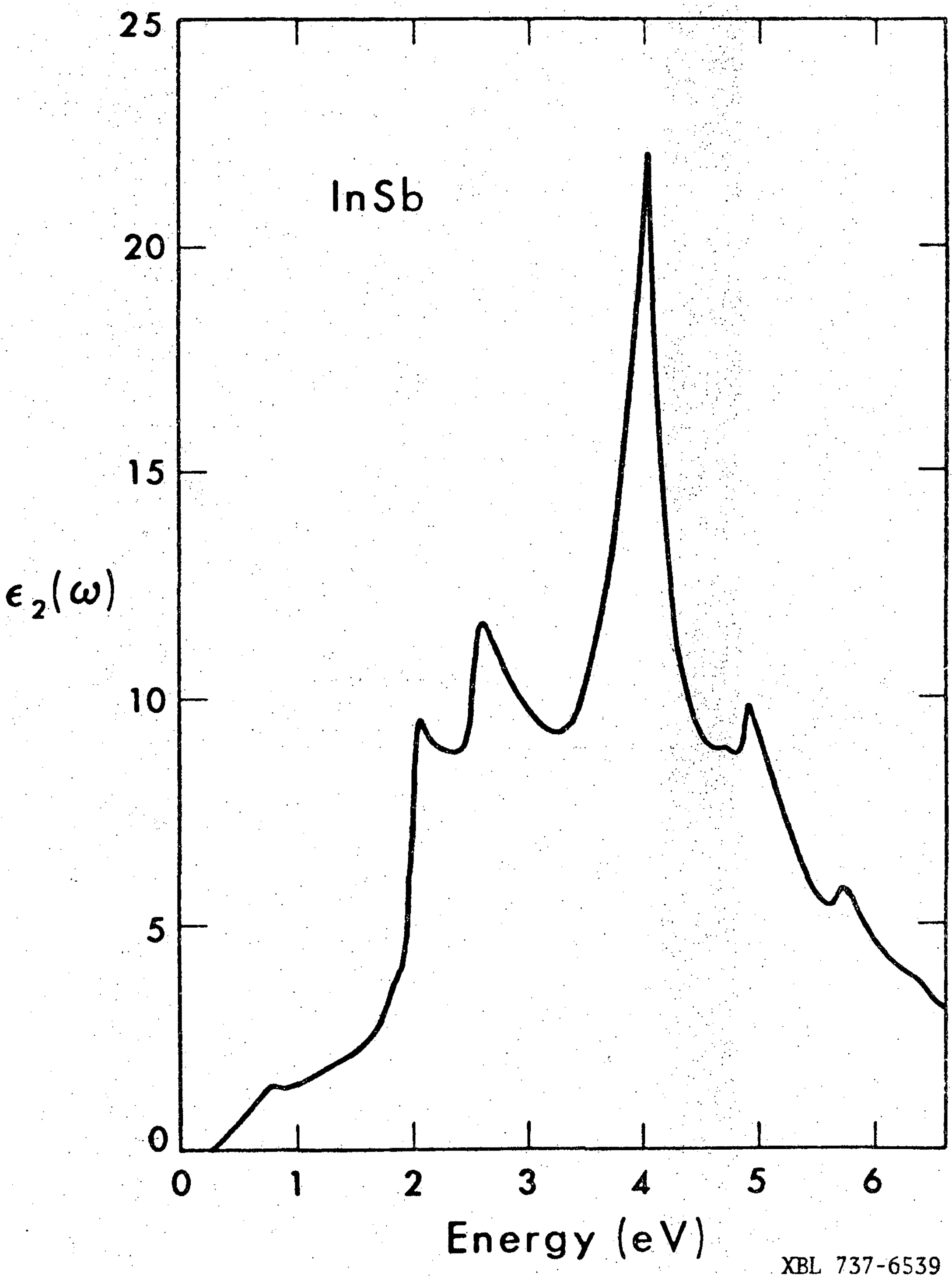

XBL 737-6539

Fig. 16

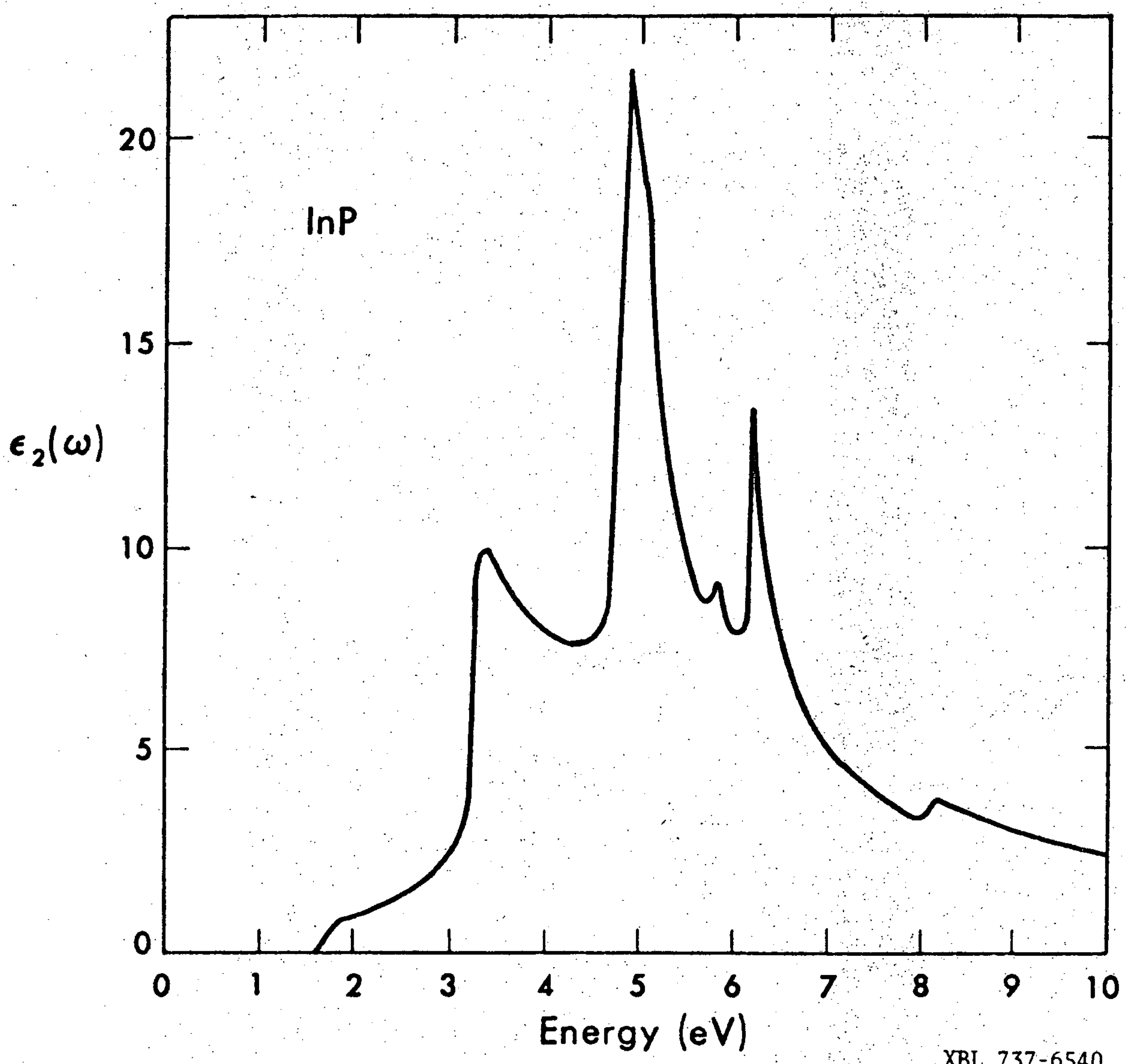
InP
$\epsilon_2(\omega)$
0
5
10
15
20
0
1
2
3
4
5
6
7
8
9
10
Energy (eV)
XBL 737-6540

Fig. 17

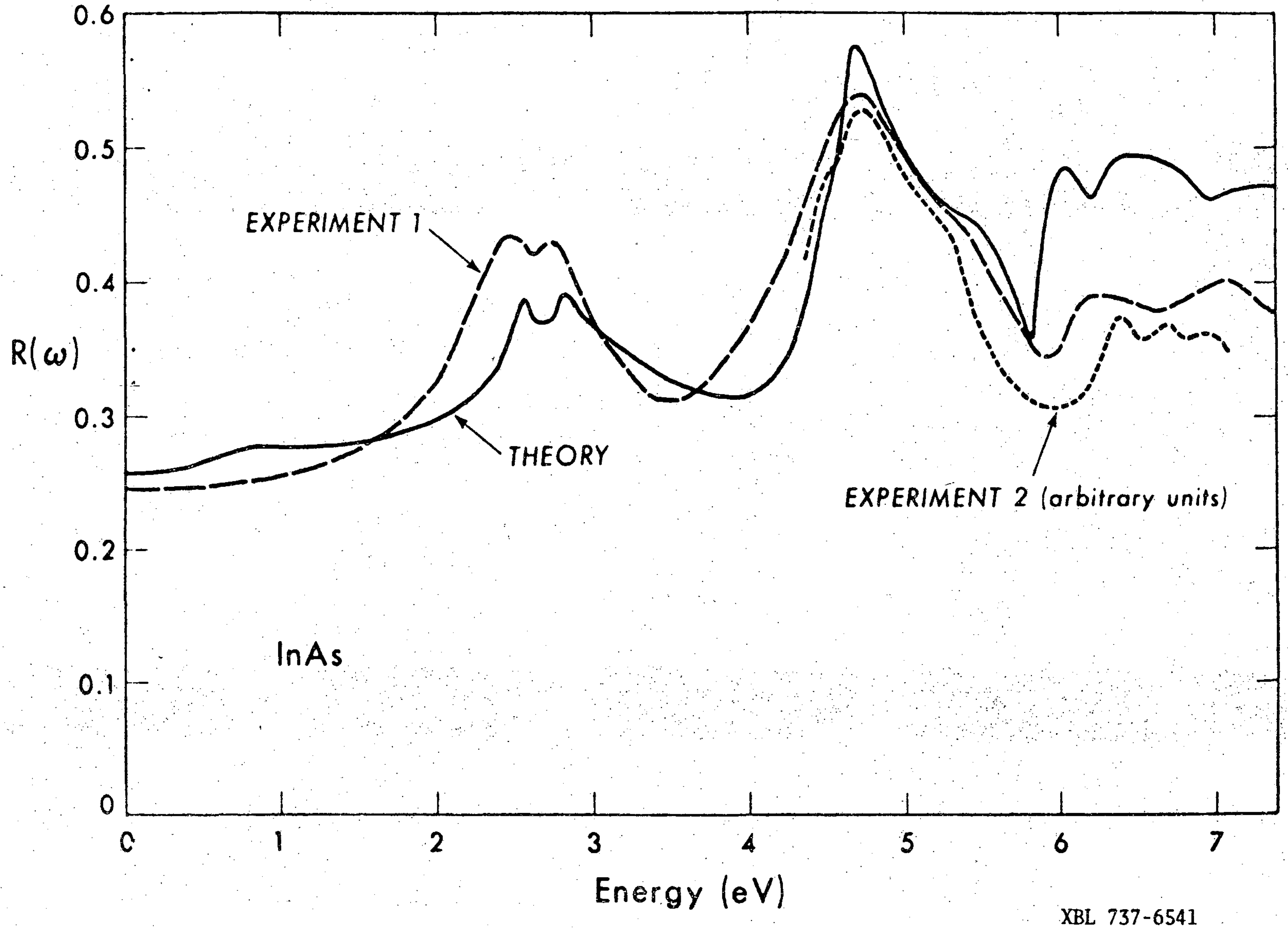

XBL 737-6541

Fig. 18

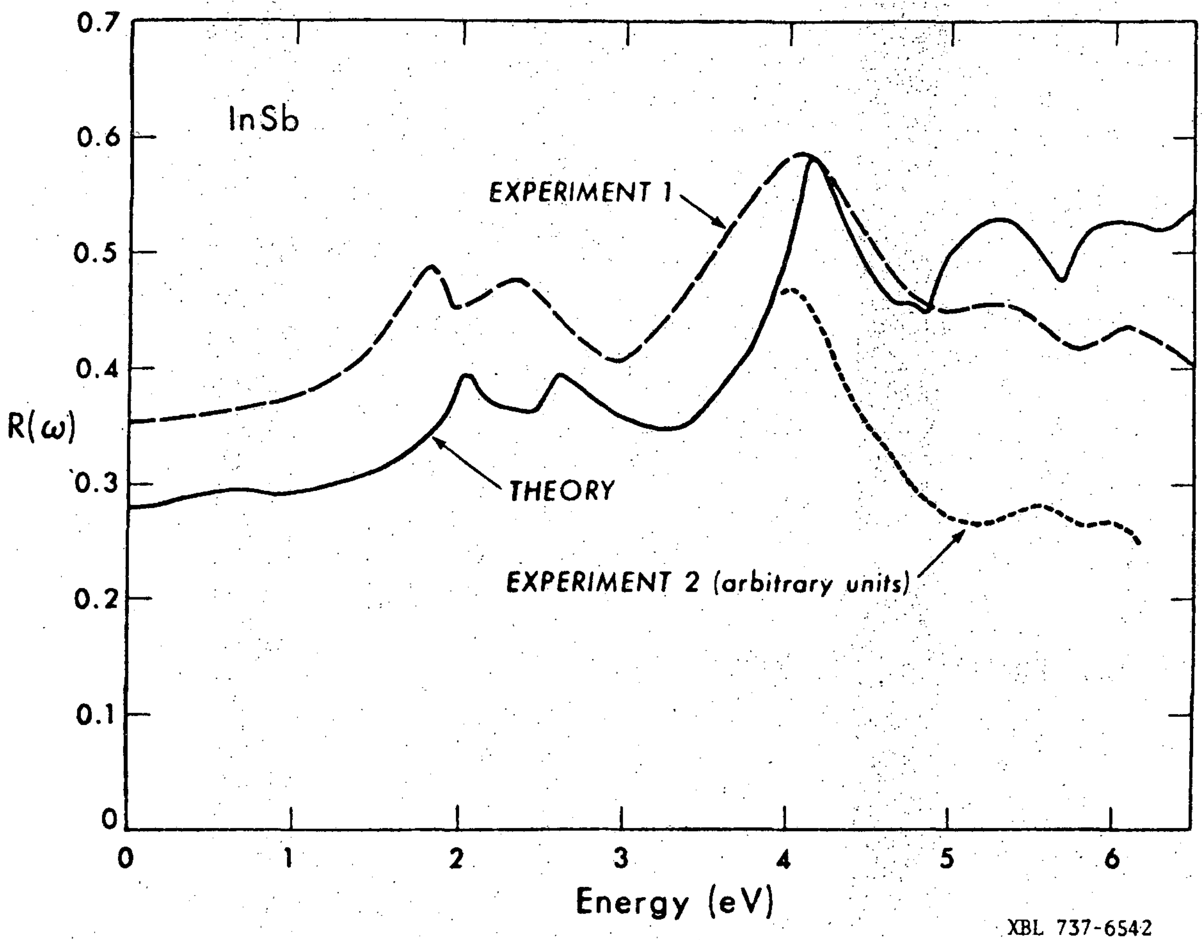

XBL 737-6542

Fig. 19

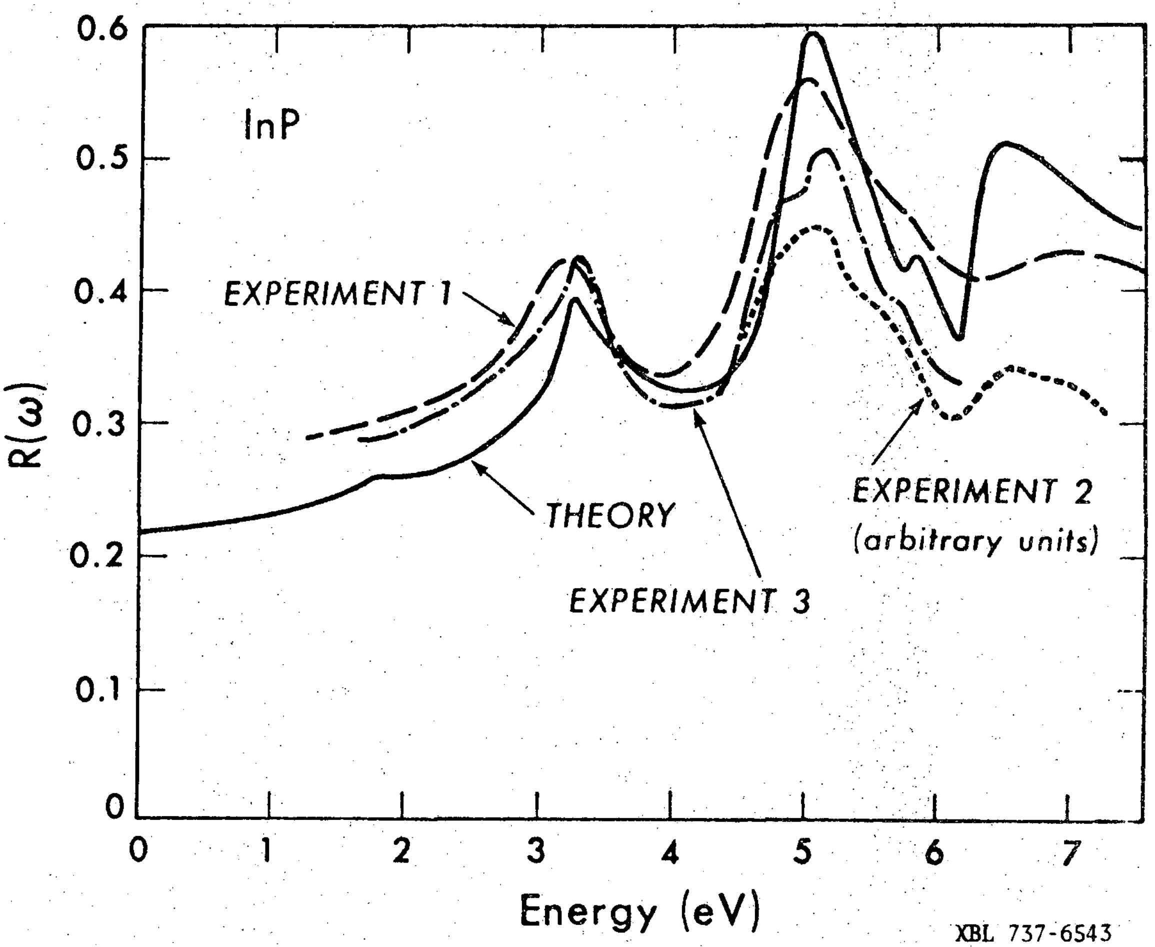

XBL 737-6543

Fig. 20

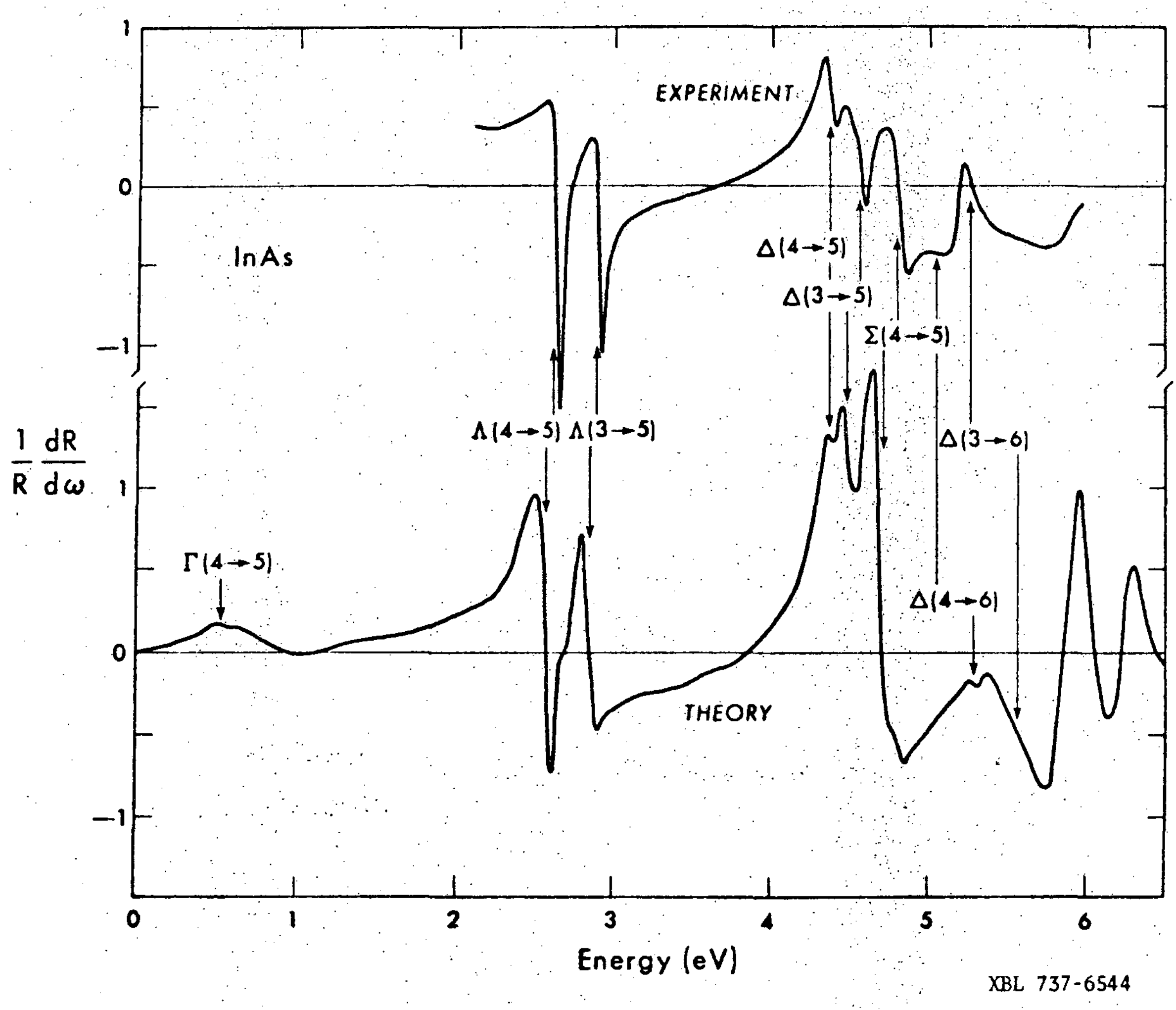

EXPERIMENT
THEORY
InAs
$\frac{1}{R}\frac{dR}{d\omega}$
1
0
−1
1
0
−1
Γ(4→5)
Λ(4→5)
Λ(3→5)
Δ(4→5)
Δ(3→5)
Σ(4→5)
Δ(3→6)
Δ(4→6)
0
1
2
3
4
5
6
Energy (eV)
XBL 737-6544

Fig. 21

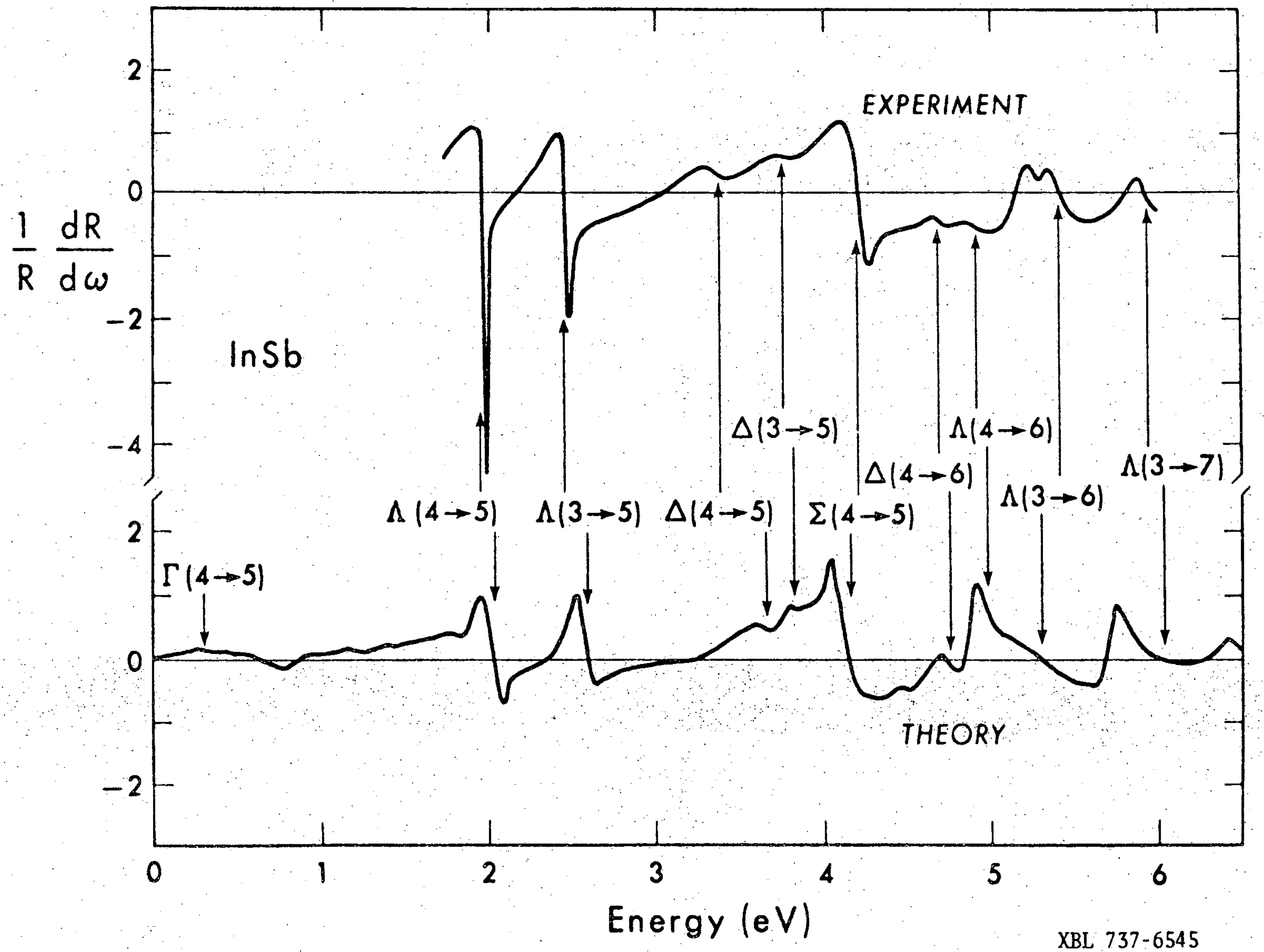

XBL 737-6545

Fig. 22

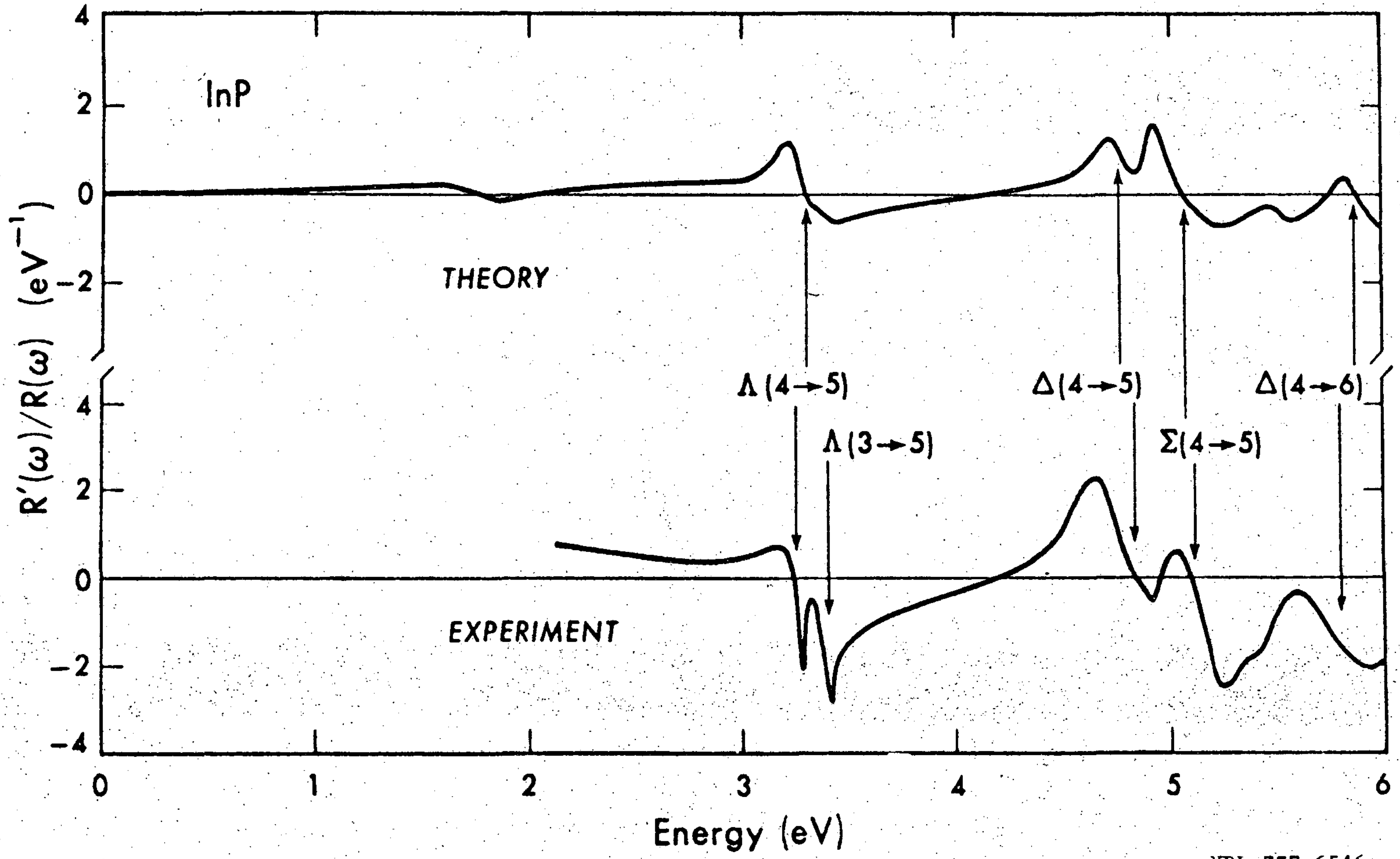

XBL 737-6546

Fig. 23

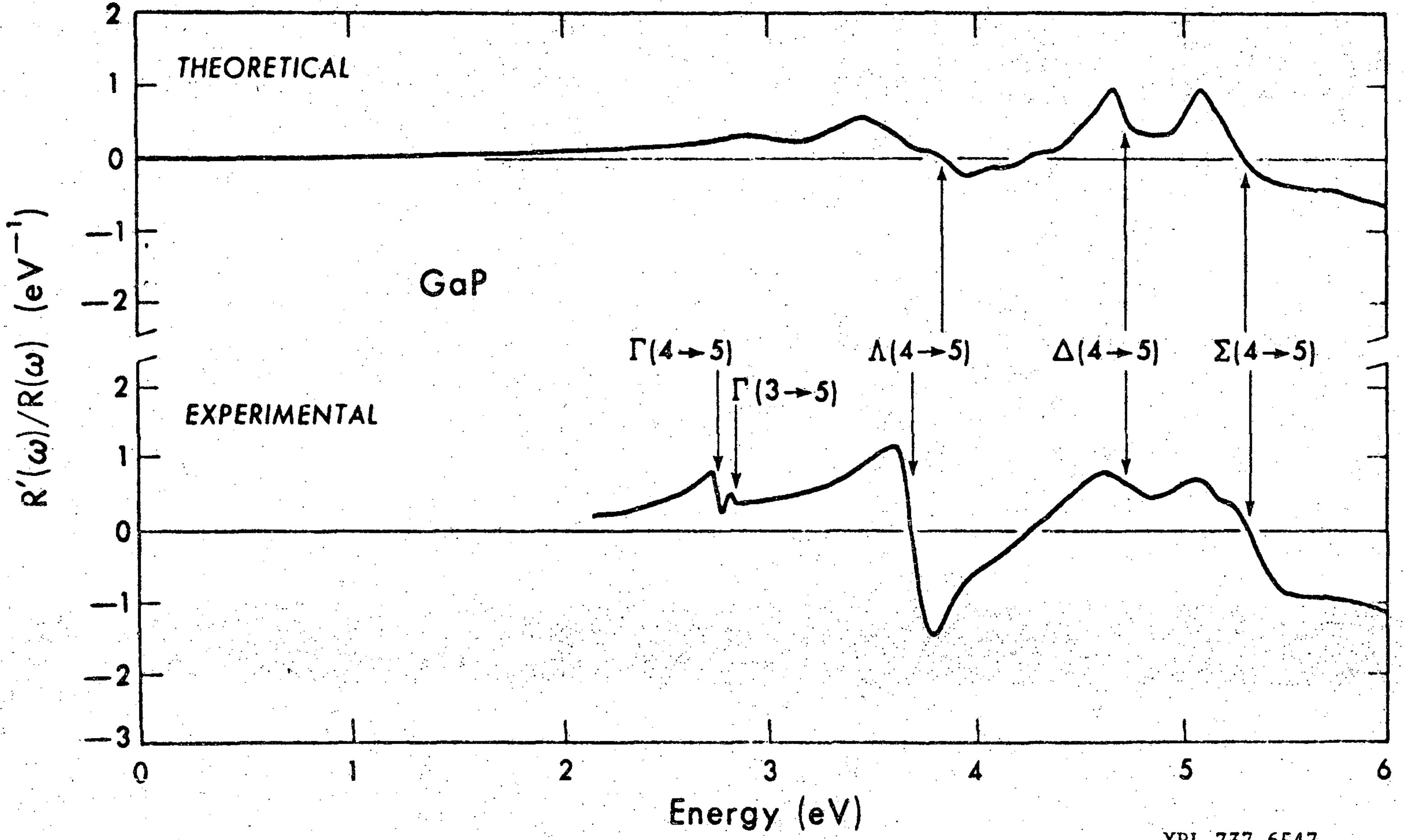

XBL 737-6547

Fig. 24

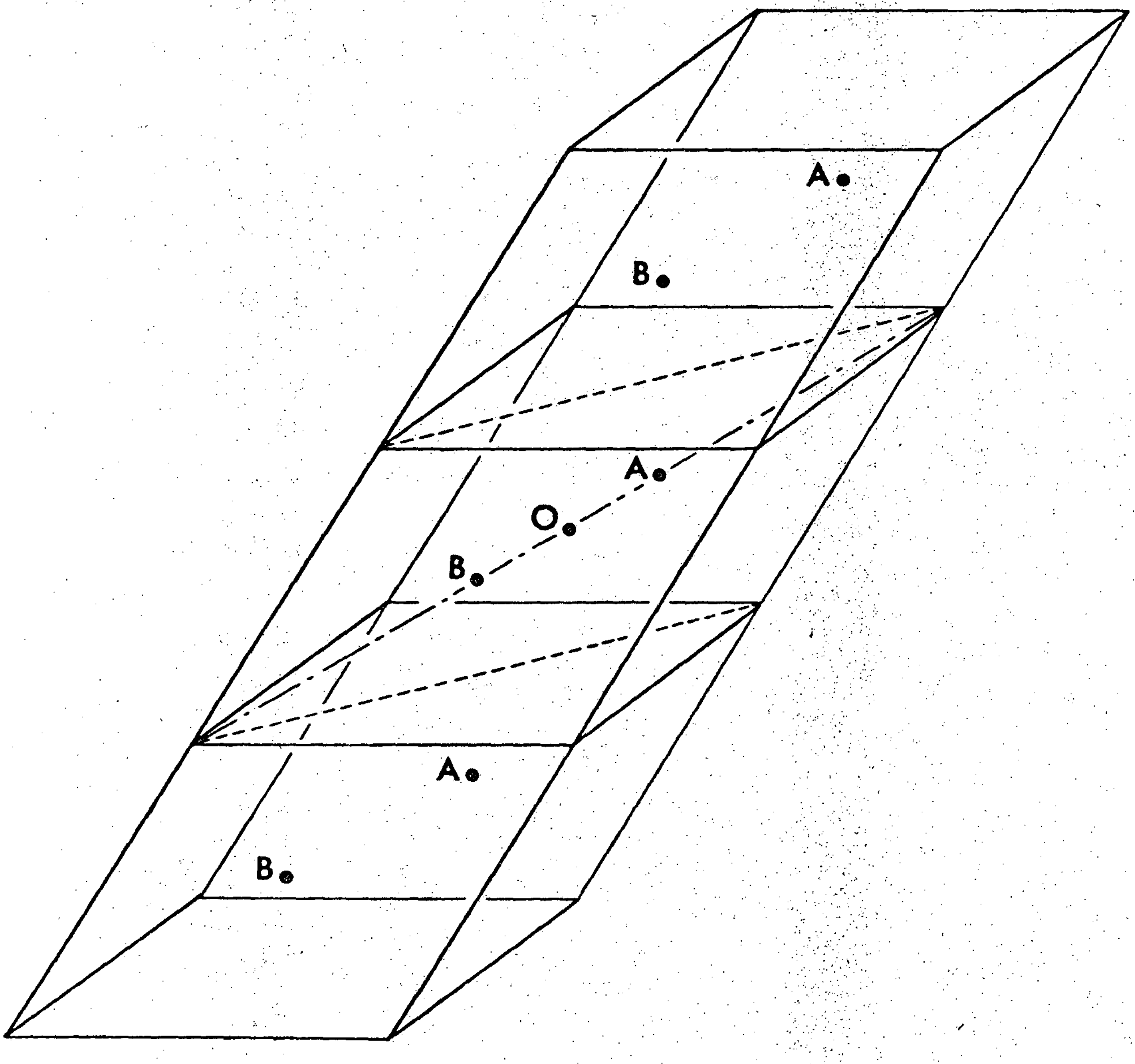

XBL 737-6548

Fig. 25

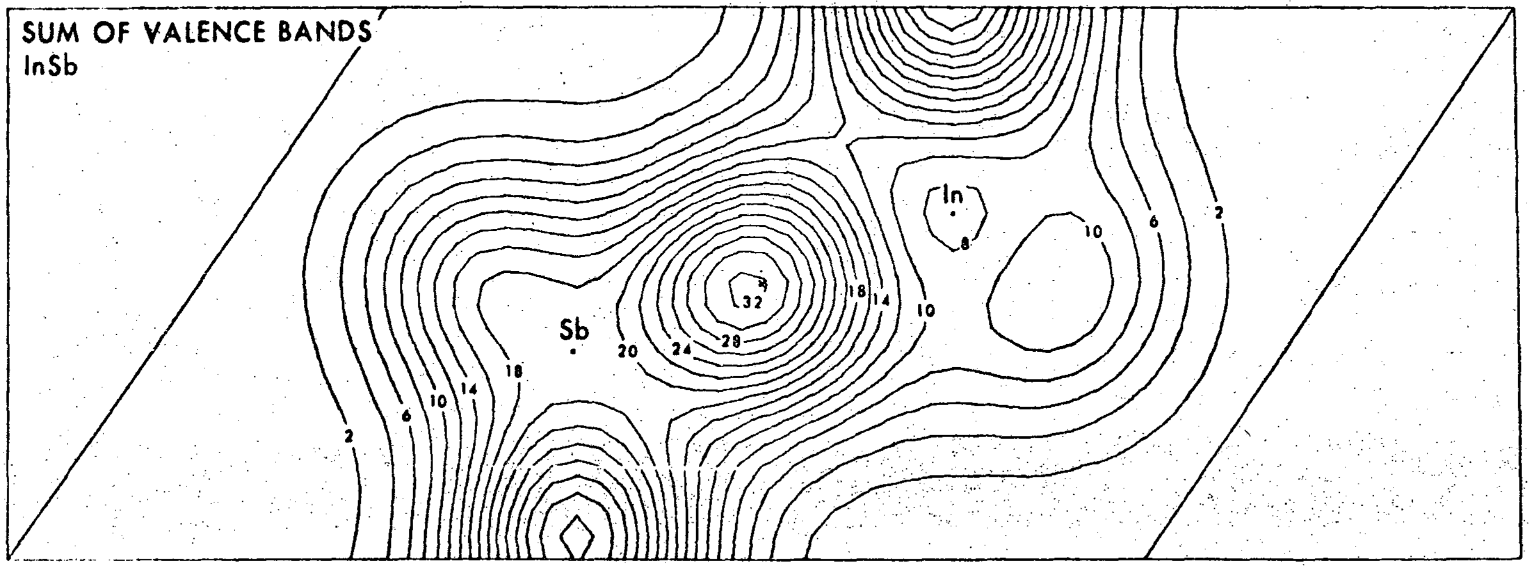

XBL 737-6550

Fig. 26

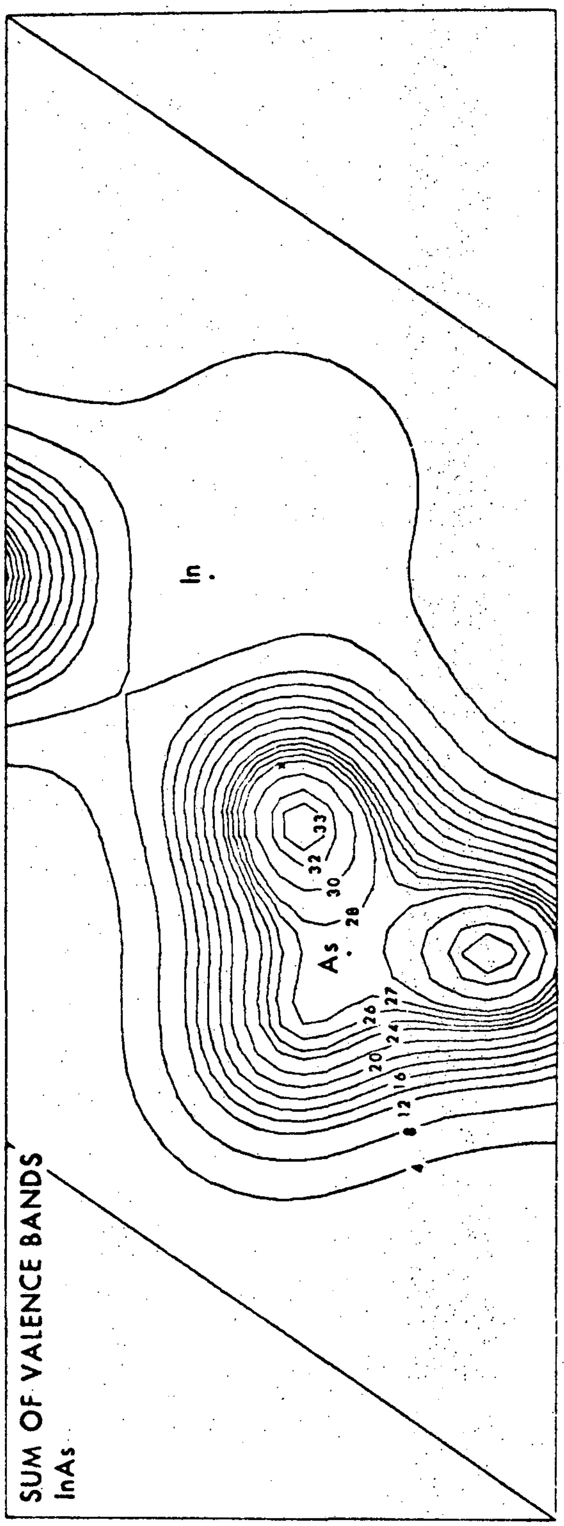

XBL 737-6549

Fig. 27

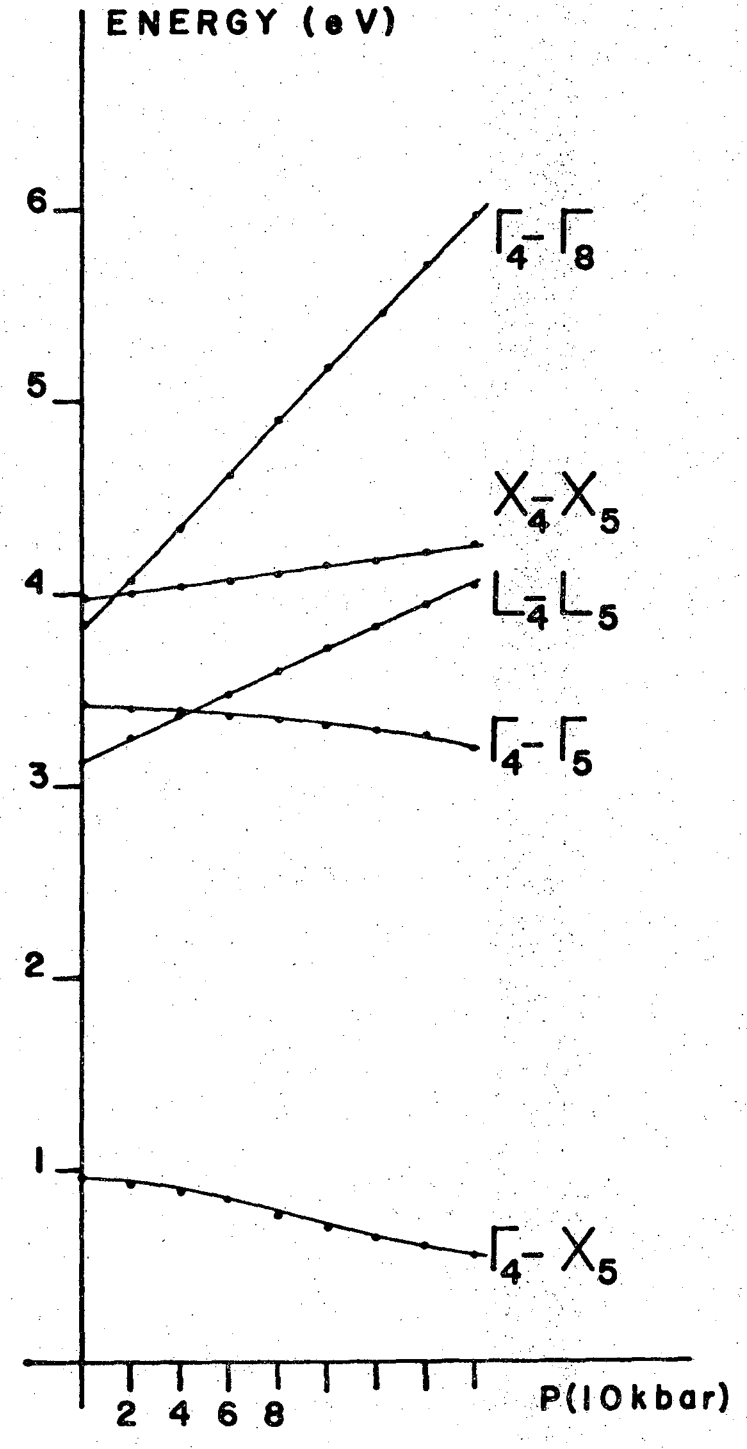

XBL 737-1502

Fig. 28

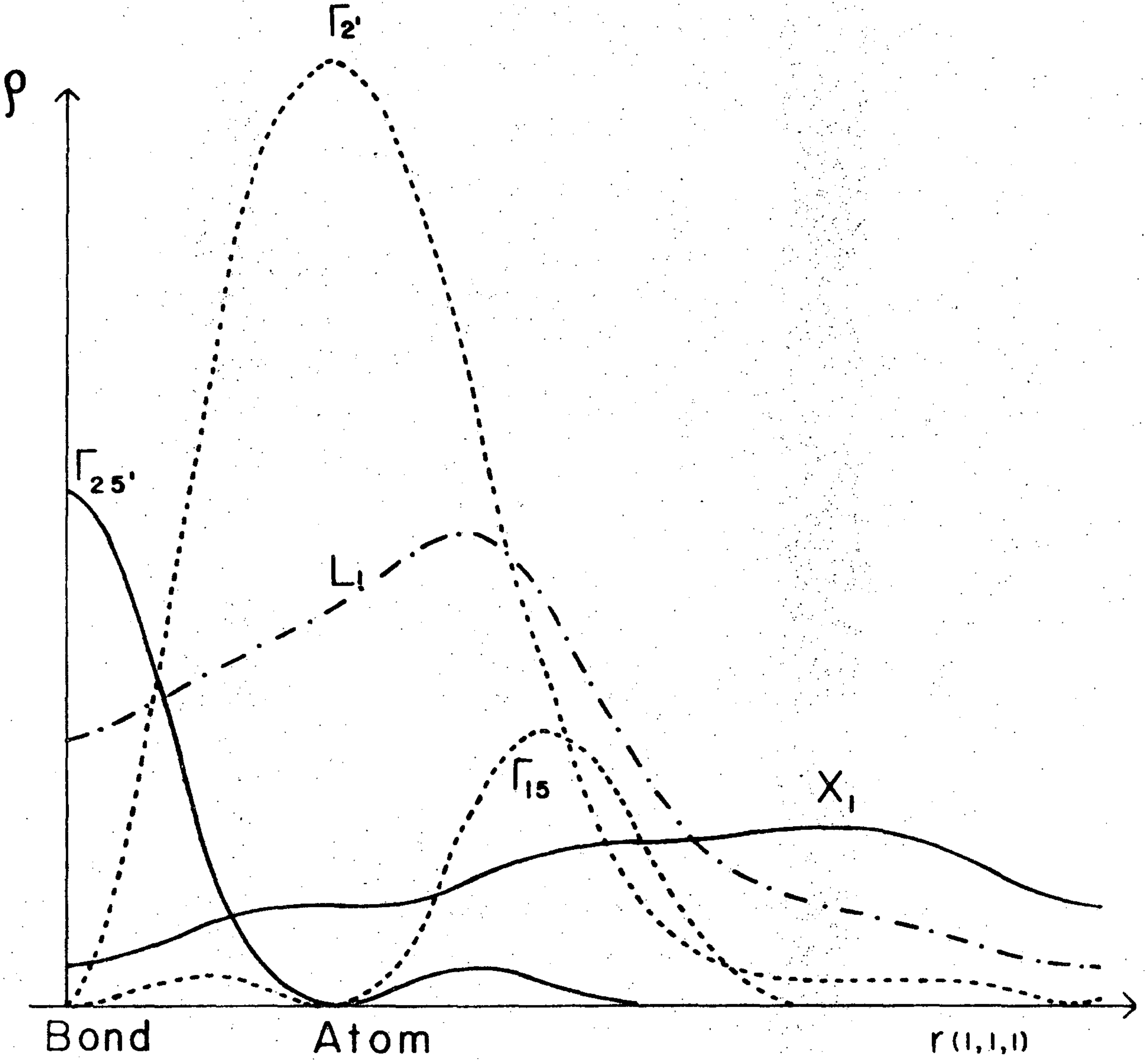

XBL 737-1501

Fig. 29

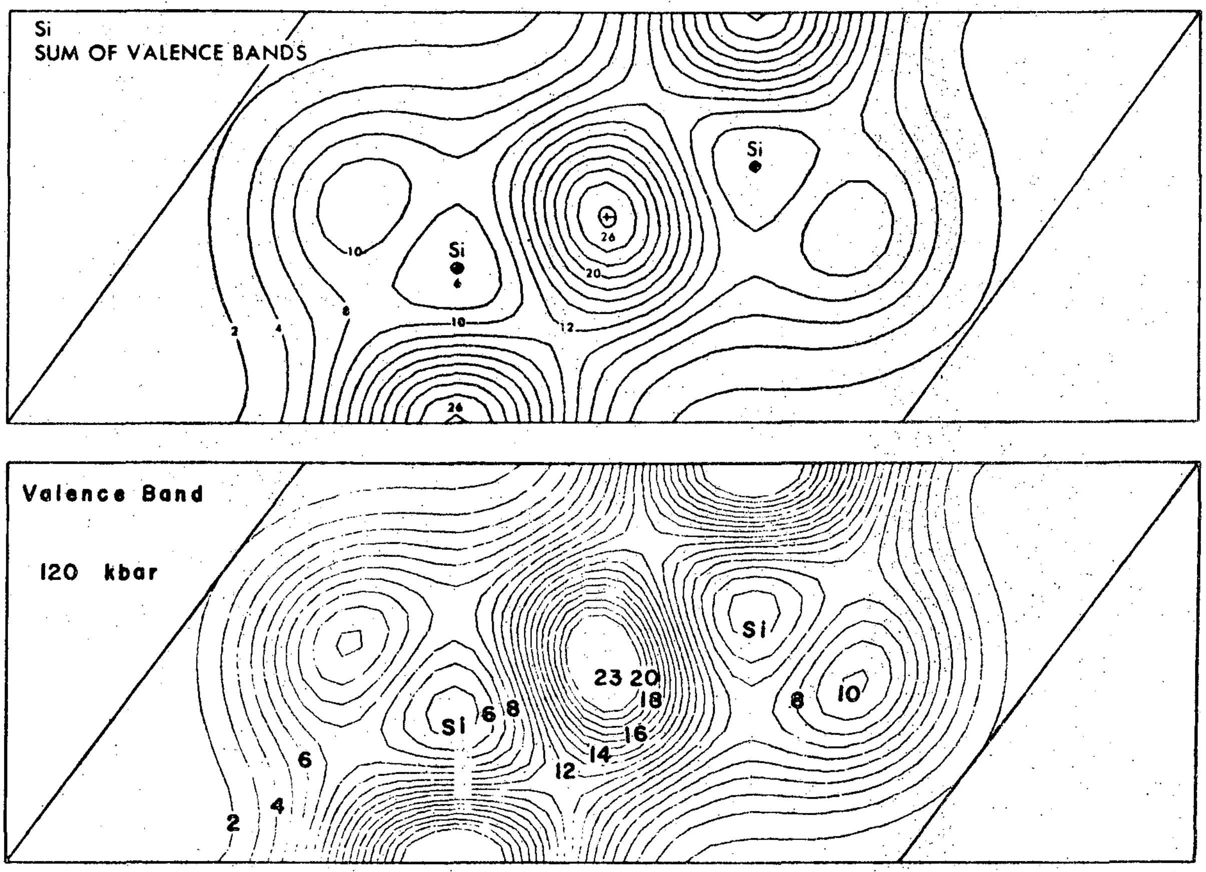

XBL 738-1761

Fig. 30

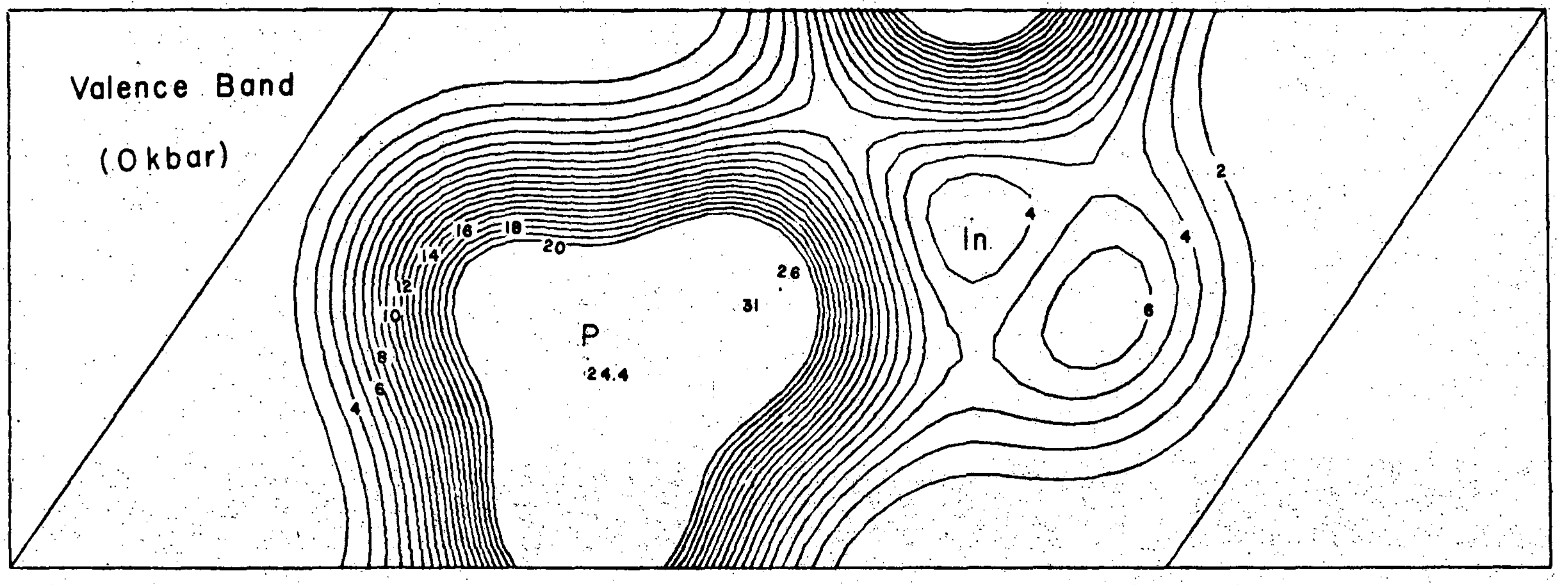

XBL 738-1759

Fig. 31

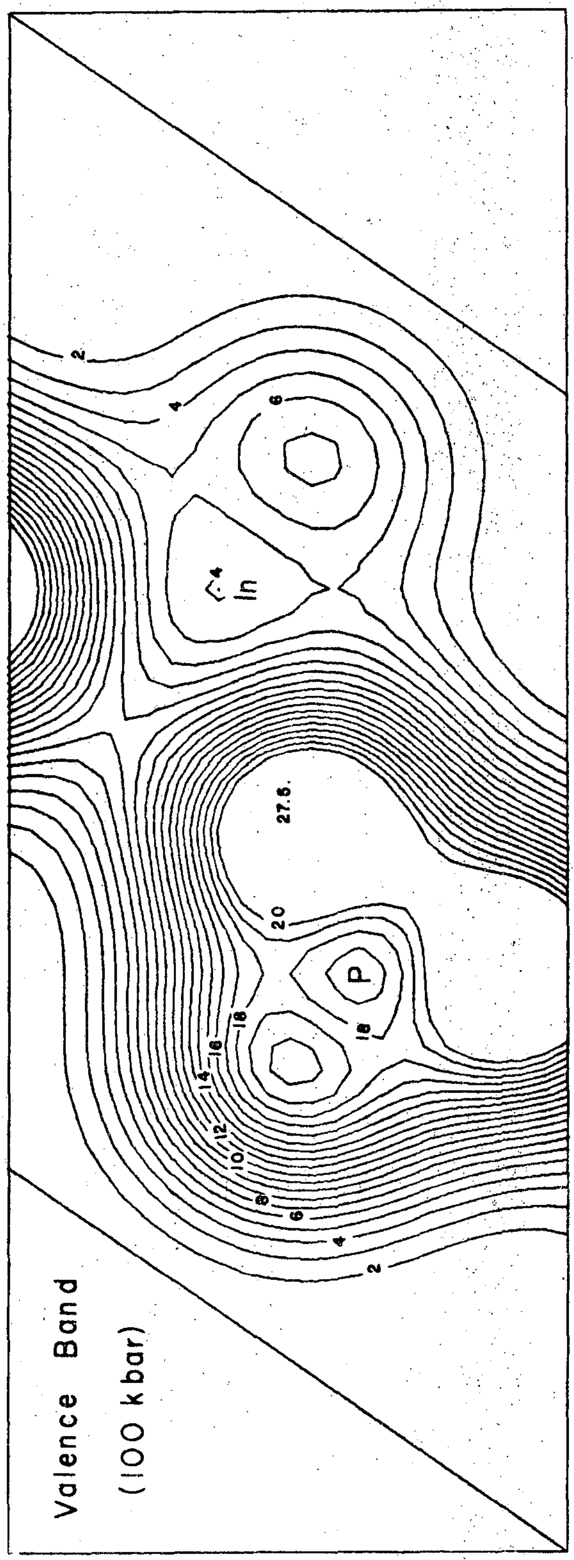

XBL 738-1760

Fig. 32

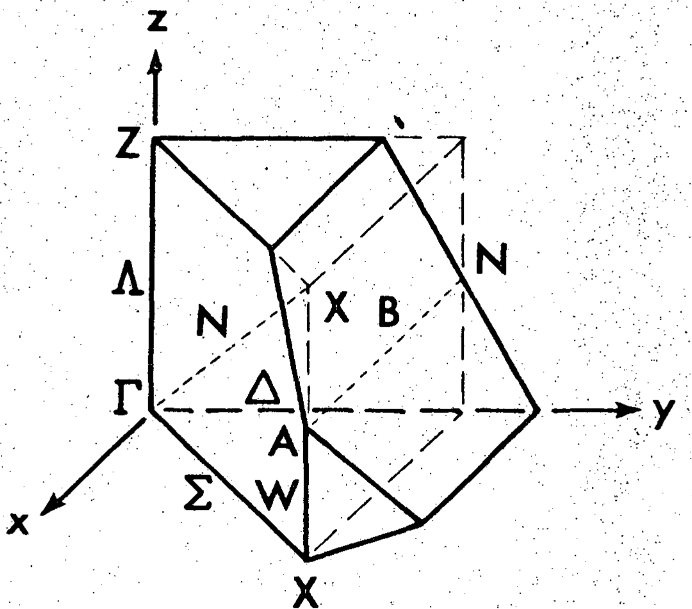

XBL 737-1503

Fig. 33

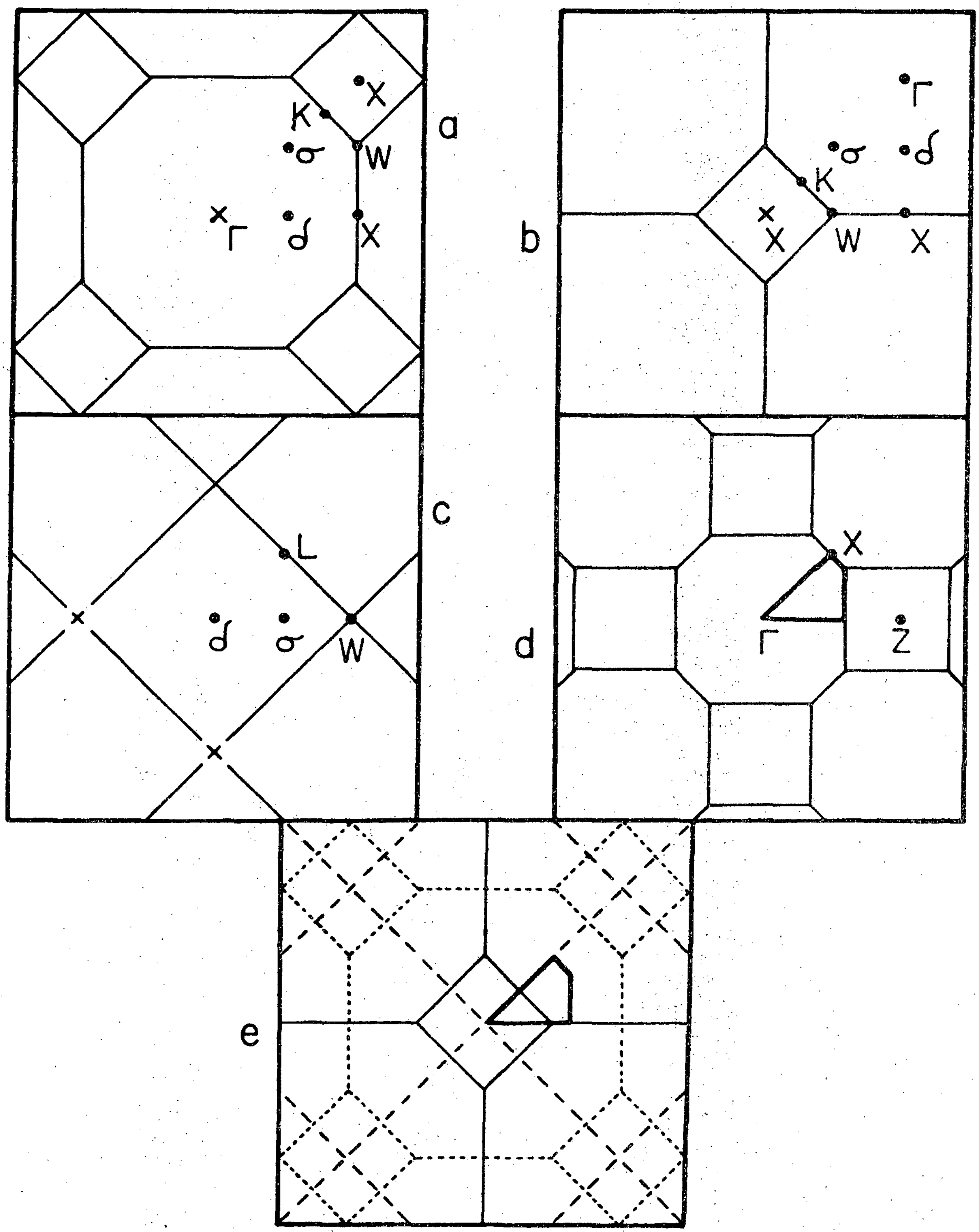

XBL 737-6597

Fig. 34

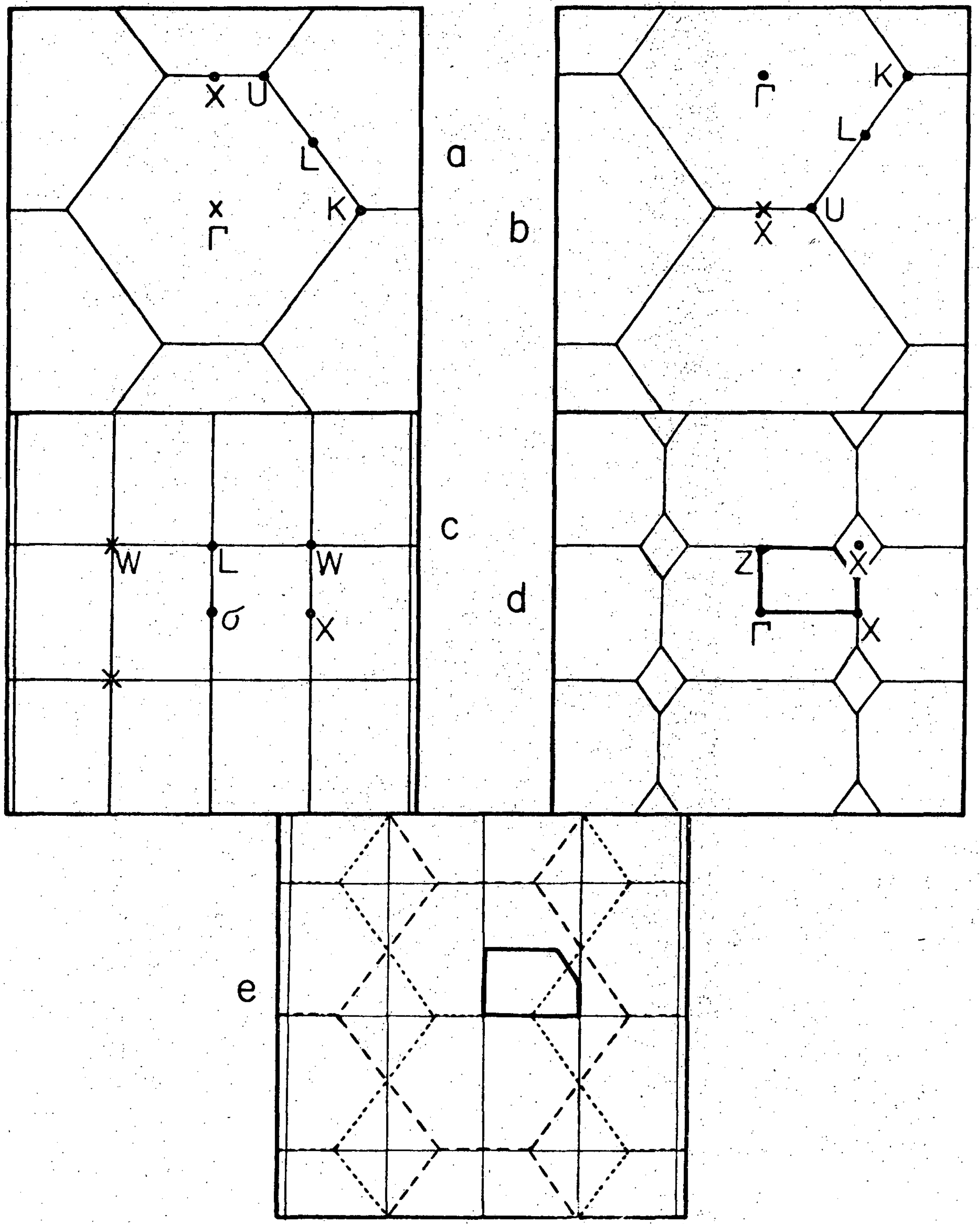

XBL 737-6593

Fig. 35

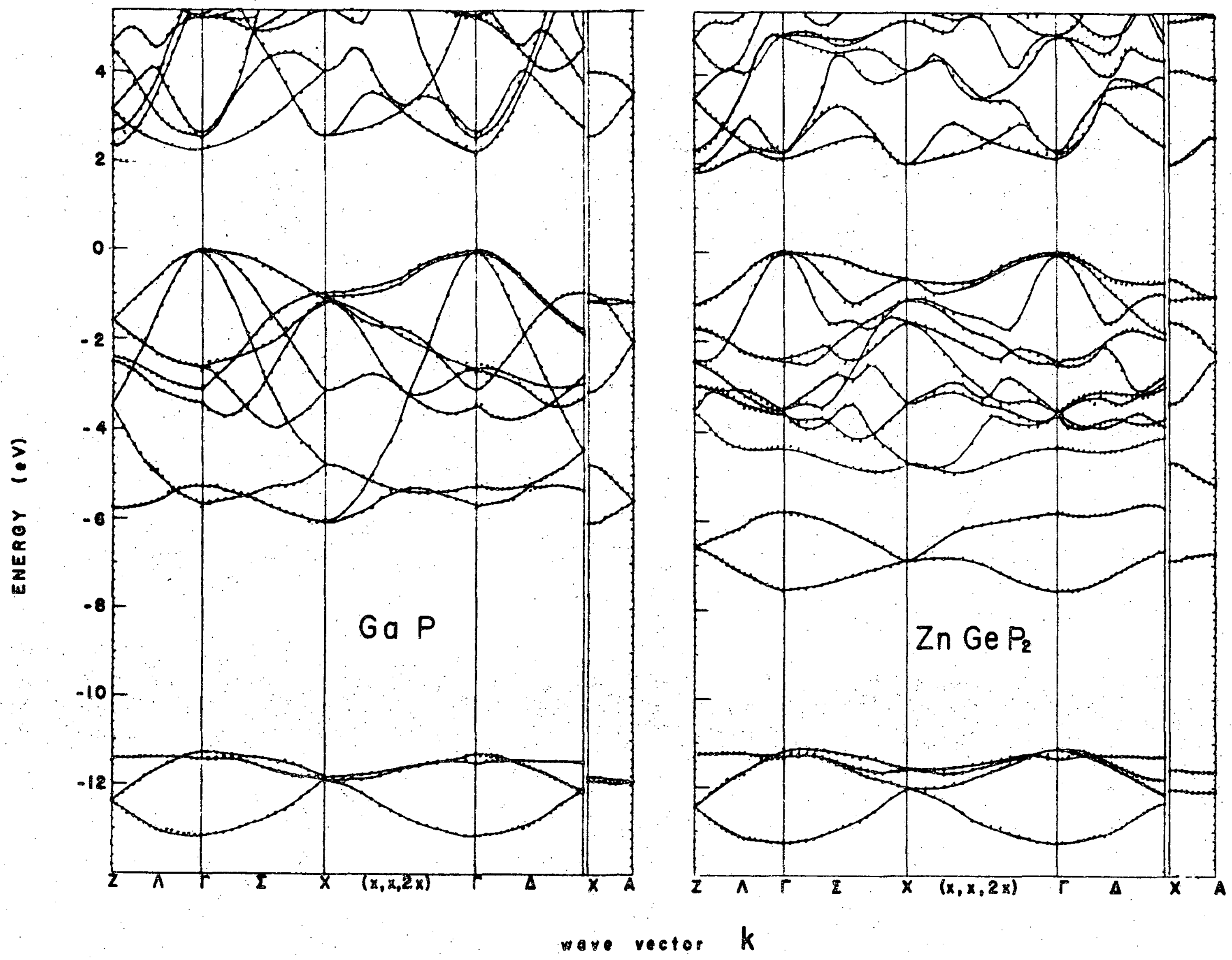

XBL-738-1767

Fig. 36

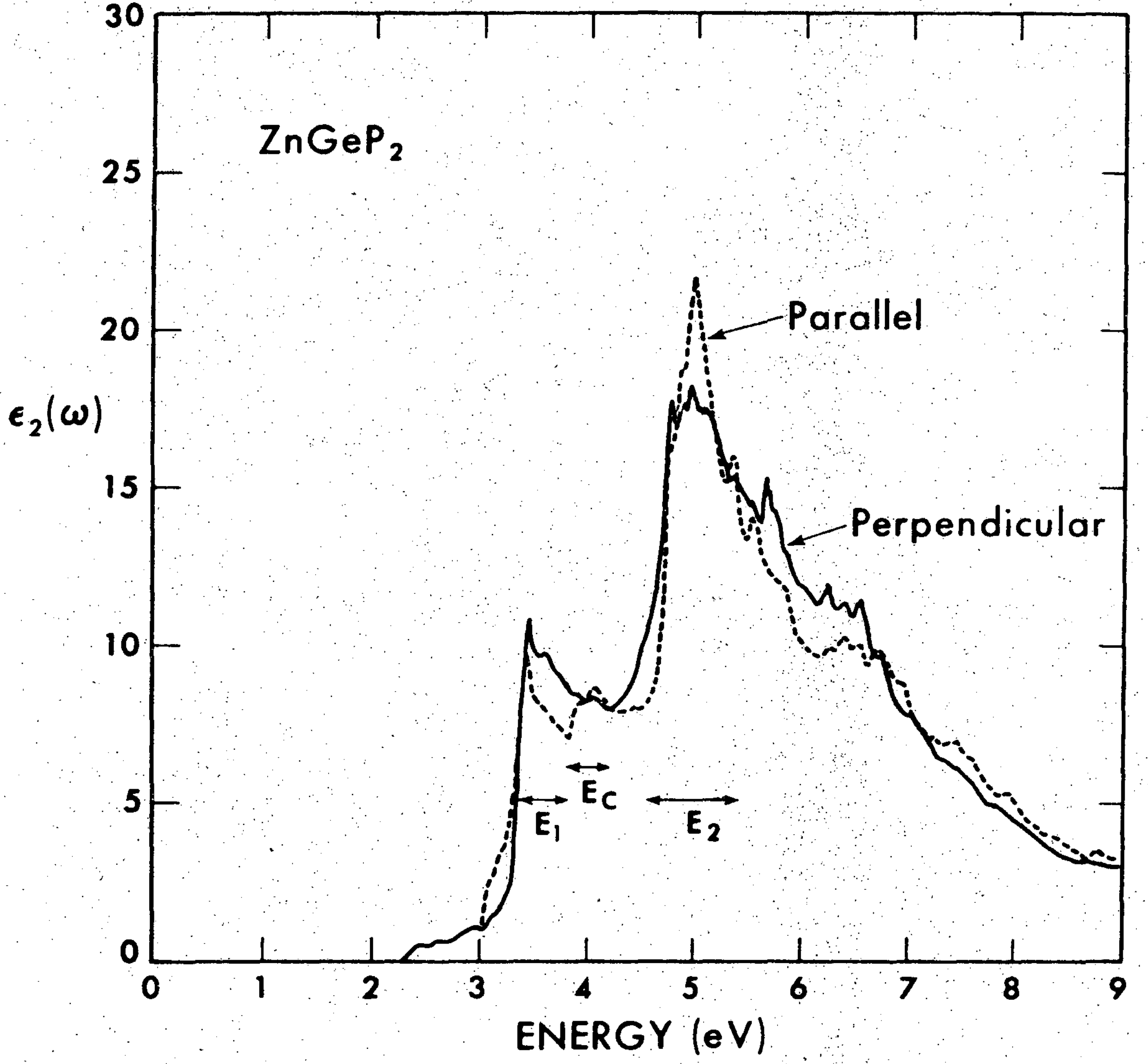

XBL 737-6599

Fig. 37

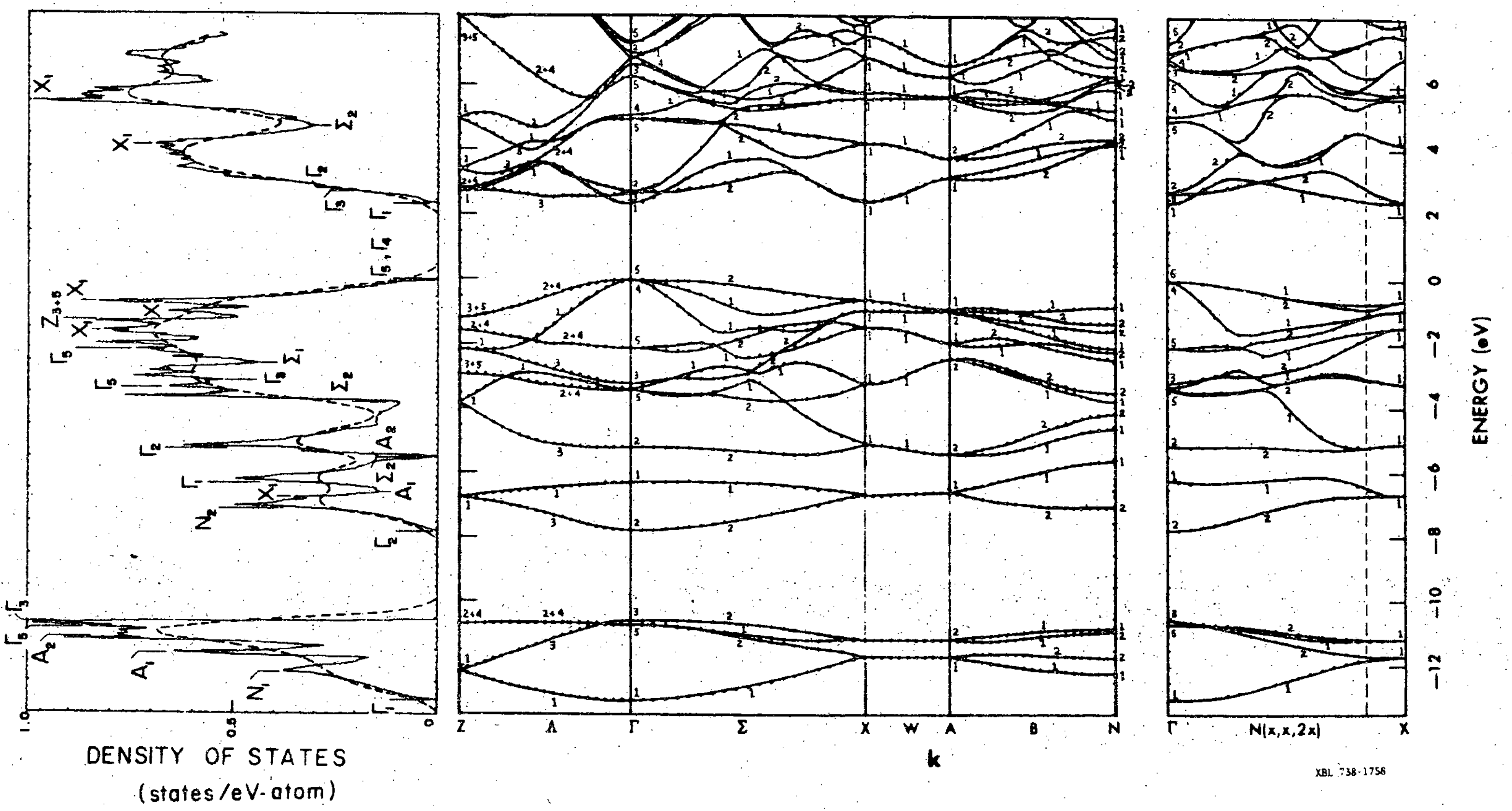
DENSITY OF STATES
(states/eV-atom)
1.0
0.5
0
X_1
Σ_2
X_1
Γ_2
Γ_5
Γ_1
Γ_5, Γ_4
Z_{3+5}
X_1
Γ_5
Σ_1
Σ_2
Γ_2
A_2
Σ_2
A_1
N_2
Γ_2
Γ_3
Γ_5
A_2
A_1
N_1
Z
Λ
Γ
Σ
X
W
A
B
N
k
Γ
N(x,x,2x)
X
ENERGY (eV)
6
4
2
0
−2
−4
−6
−8
−10
−12
XBL 738-1756

Fig. 38

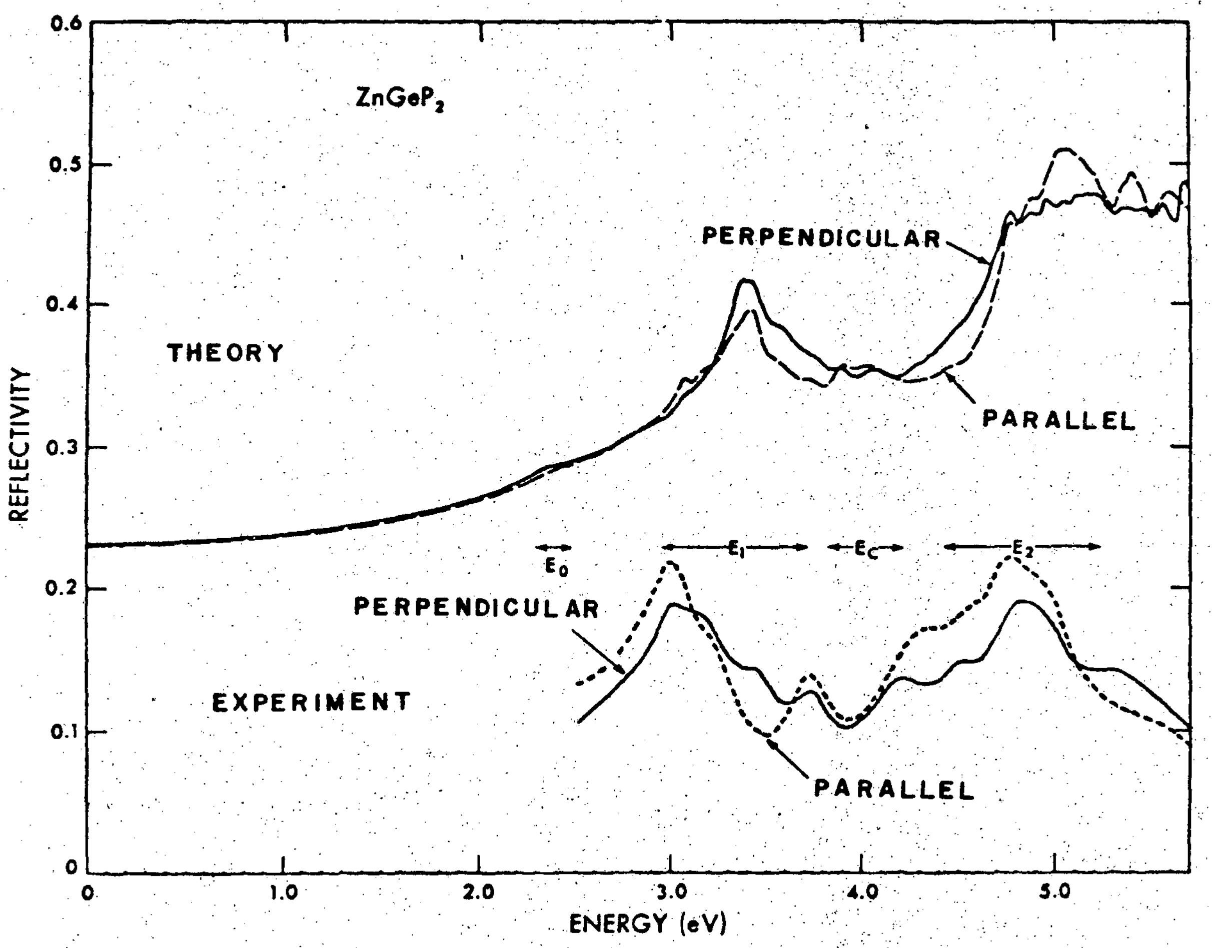

XBL 738-1762

Fig. 39

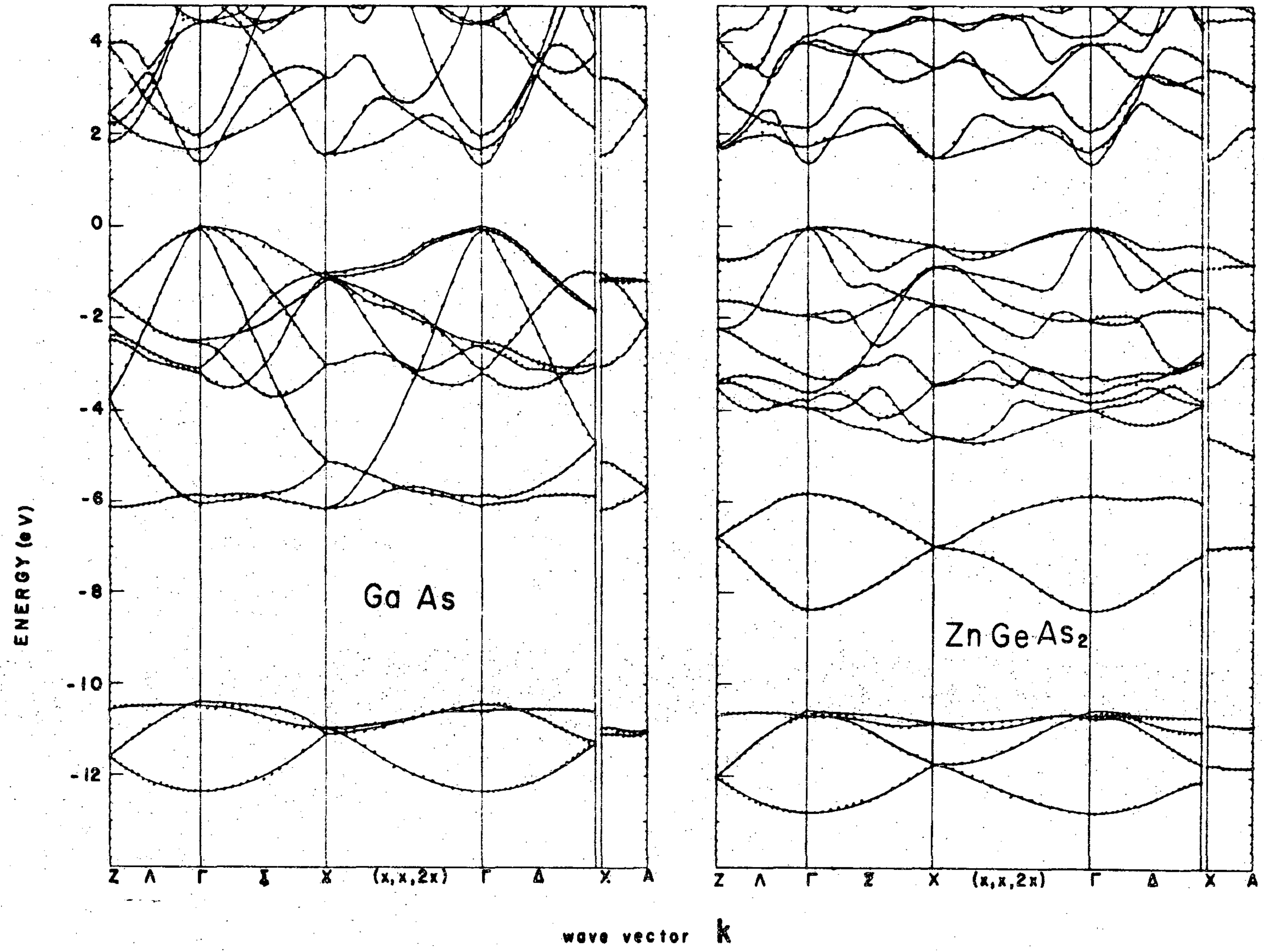

XBL 738-1768

Fig. 40

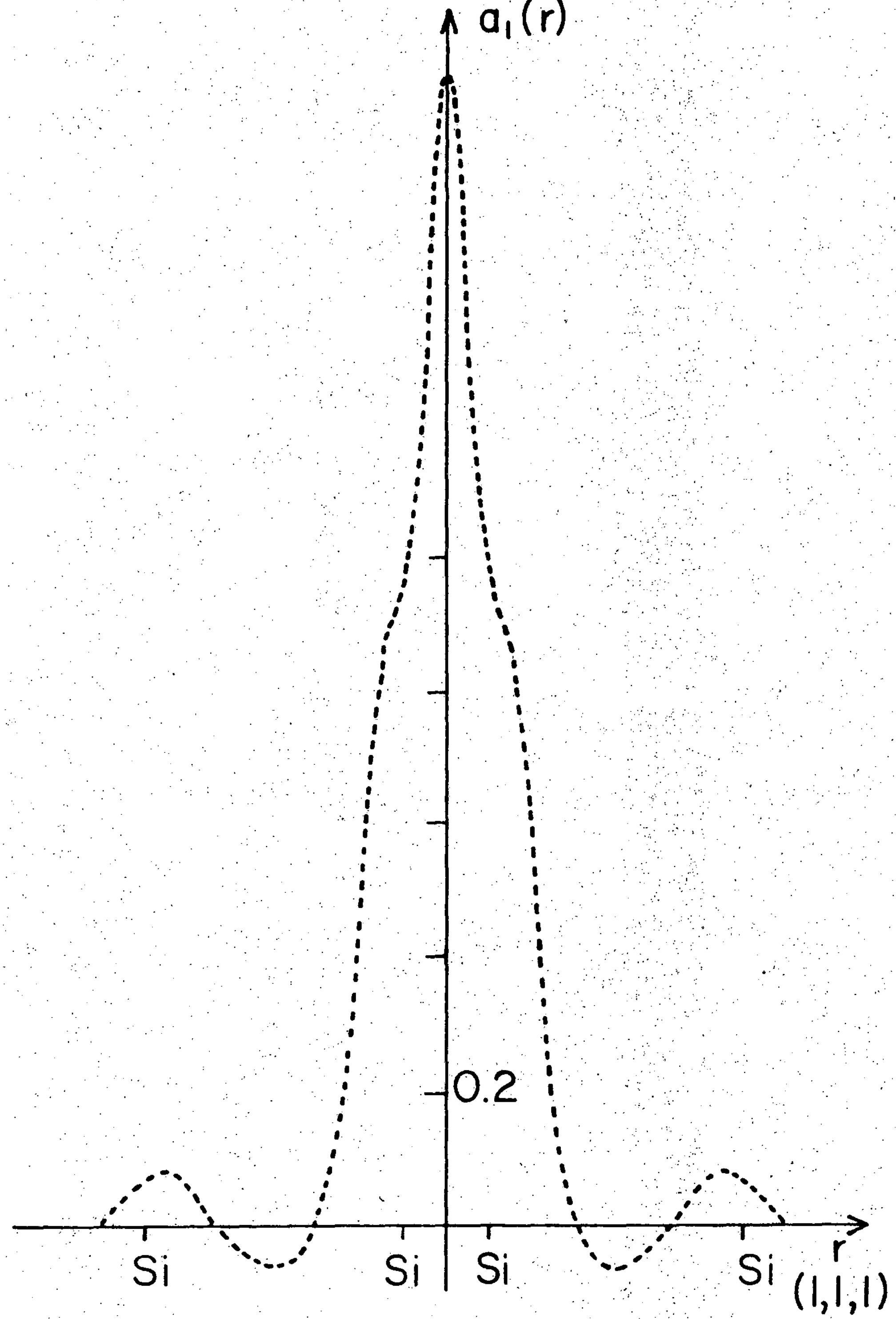

XBL 737-1500

Fig. 41

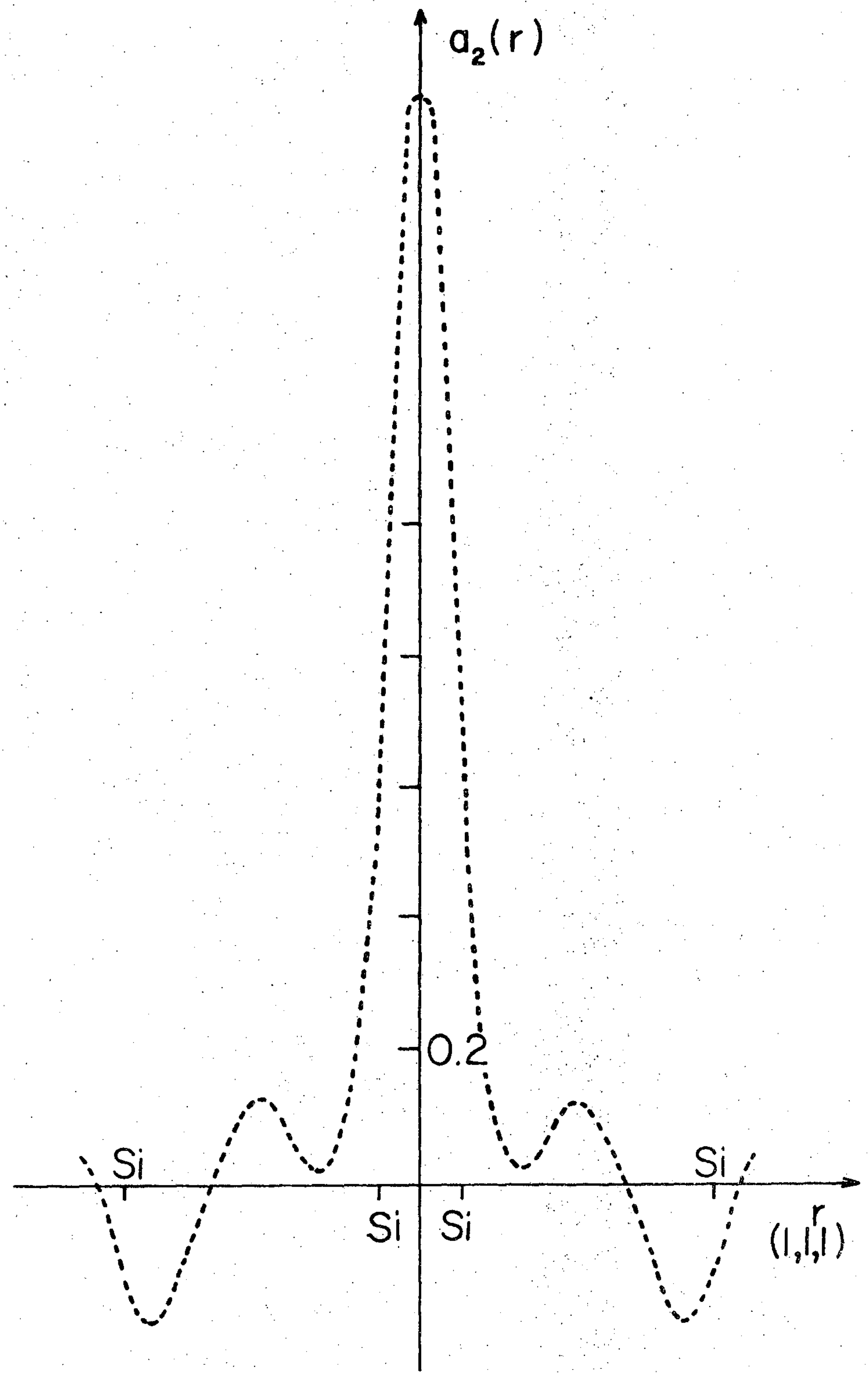

XBL 737-6598

Fig. 42

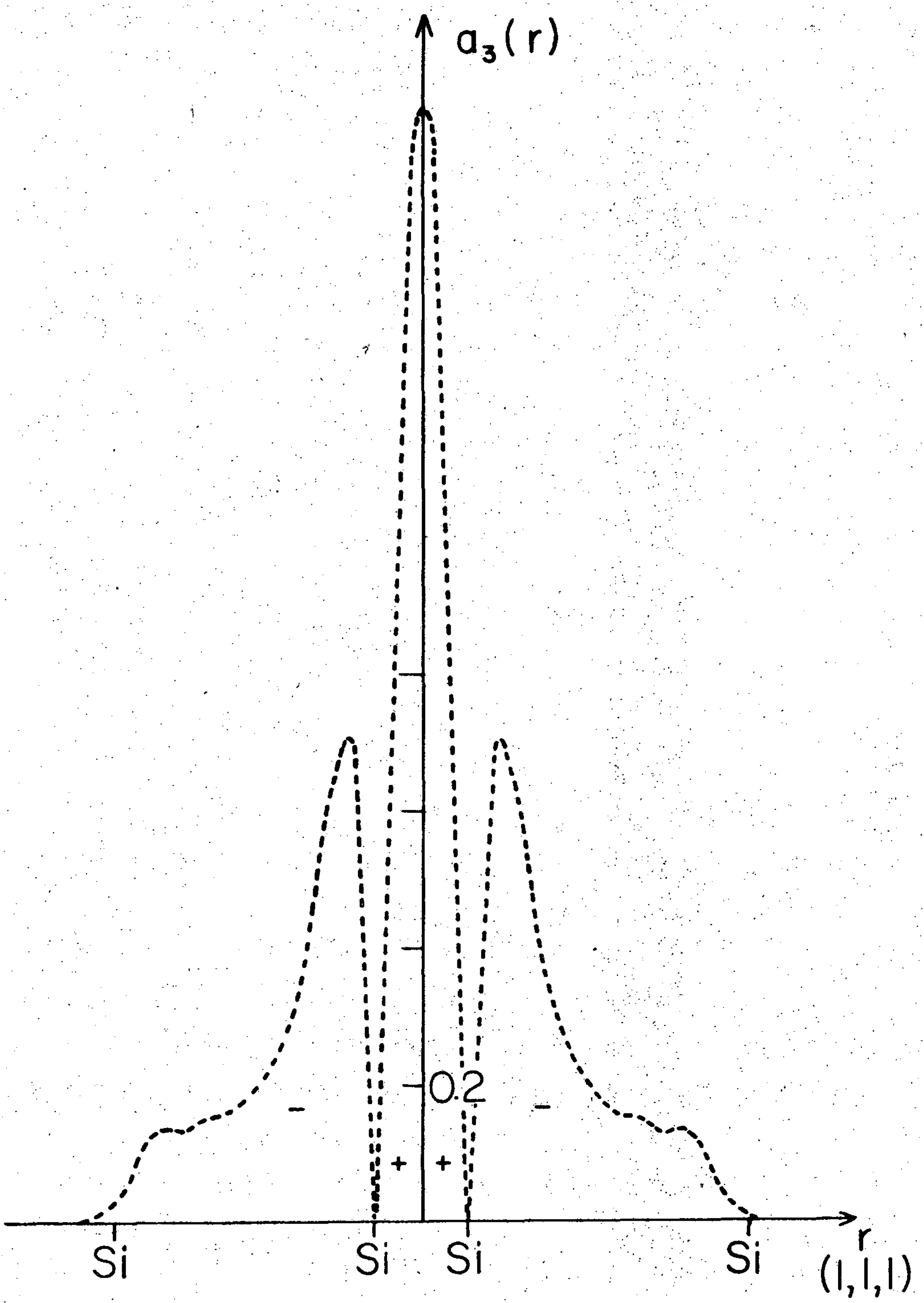

XBL 737-6595

Fig. 43

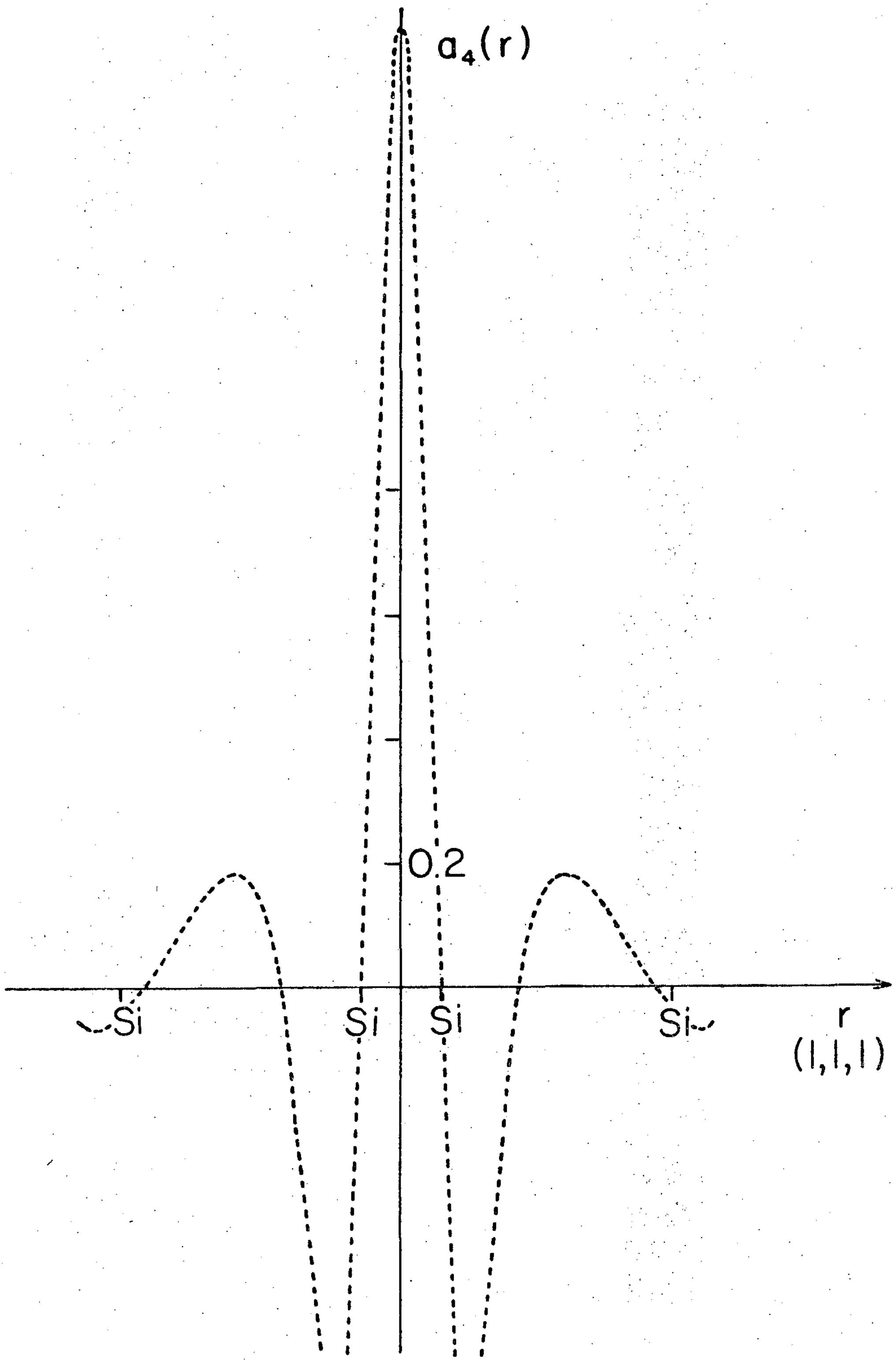

XBL 737-6596

Fig. 44

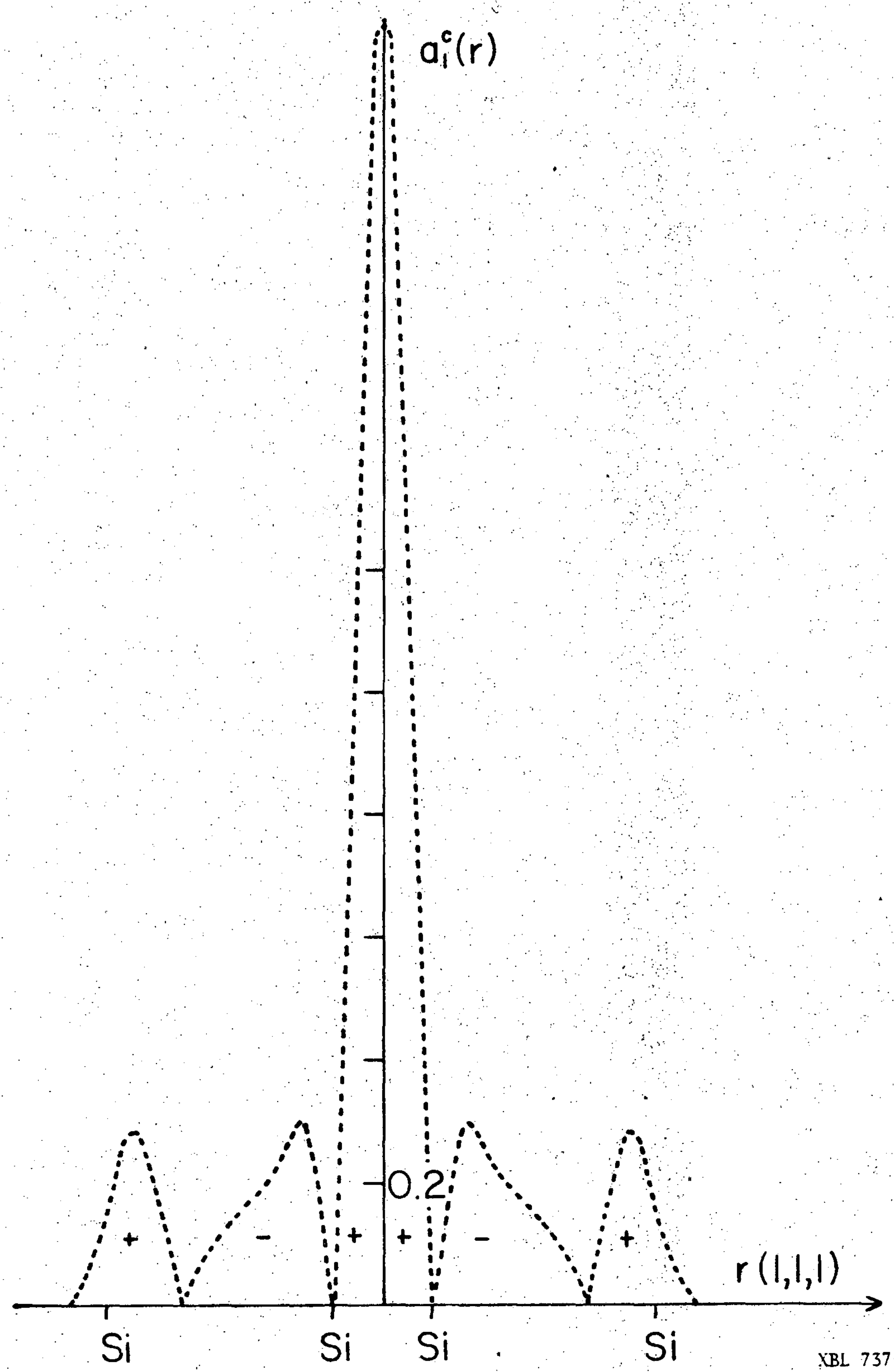

XBL 737-6594

Fig. 45

TECHNICAL INFORMATION DIVISION
LAWRENCE BERKELEY LABORATORY
UNIVERSITY OF CALIFORNIA
BERKELEY, CALIFORNIA 94720